Università degli Studi di Padova

Dipartimento di Fisica e Astronomia

CNR-Istituto di Fotonica e Nanotecnologie di Padova

Corso di Laurea Magistrale in Fisica

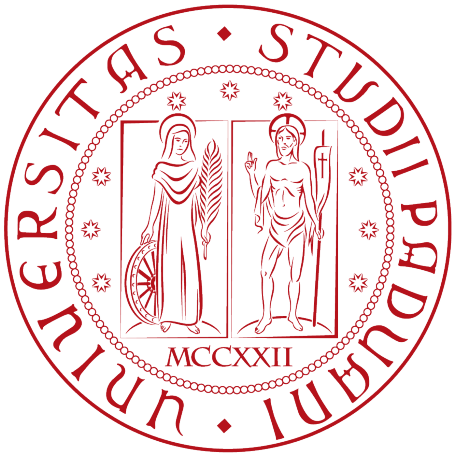

Shape Memory Alloys for Adaptive Optics

Relatore: Stefano Bonora
Correlatore: Martino Quintavalla

Laureando: Antonio Vanzo

Ottobre 2017

Contents

Introduction

Shape memory alloys (SMAs) are smart materials that, upon deformation, return to their original shape when heated above a temperature threshold. This special behaviour makes SMAs very attractive as efficient strain/force actuators with very large strains (up to 8%). For this reason, SMAs have been widely used in several applications, from surgery to space. In thesis work, we considered the use of SMAs to build a deformable lens, i.e. a lens with tunable focal length.
Usually, optical systems are realized by using optical components such as lenses and mirrors that have fixed optical power (focal length) and that sometimes can be moved, as it occurs in zoom systems. In such cases the movements are achieved manually or by using motors that are slow and subjected to mechanical wear. More recently, optical elements with variable focal length, hence called "adaptive" have been developed, allowing for a great simplification in optical design. Among all the available materials used for actuation, SMAs possess a higher strain with respect to the common actuation materials used to build deformable lenses (such as the piezoelectric). Moreover, they don't need high actuation voltages and, by using SMA wires, allow to realize very small actuators, and consequently very compact devices. SMA wires present however a strong hysteresis in their transformations and the models that describe their behaviour are complex. Luckily, the resistivity of the wires presents a linear dependence from the strain of the wire under certain conditions. This allows the use of the resistivity as feedback parameter to control the strain of the wire and consequently the behaviour of the device.
The idea behind this thesis project is to build a lens with variable focal length by employing SMA wires. The lens consists in two thin glass sheets with a gel layer among them. Each glass sheet is symmetrically bent by two SMA wires which hook it at its extremities. The two glass sheets are bent along perpendicular axes in such a way that each glass determines the focusing of light rays on planes parallel to the axis along which it is bent. Controlling the strain of the wires by heating them with current allows to control the glass surface curvature and consequently the focal length. Herein, we demonstrate that SMA wires with 50 μm diameter can efficiently bend thin glass sheets and be employed for developing lenses with variable focal length.
We can sum up the thesis work as follows:
In chapter 1, shape memory alloys and their properties are introduced in order to understand their behaviour and why they are frequently employed as actuation materials. We then make a dissertation on the principal applications of SMAs in several fields.
In chapter 2, we introduce adaptive optics and its scopes, dwelling on the principal types of aberrations that afflict optical systems. Subsequently, we describe the current techniques with which deformable lenses are developed, and in particular those lenses with a variable focal length. Then, we describe the deformable lenses which already employs SMA elements.
In chapter 3, we briefly introduce the several models which have been used until now to describe SMAs behaviours. Then, the model chosen by us is described in detail and how we implemented a simulation of SMA wires in different conditions by employing this model is explained.
In chapter 4, SMA wires are tested at different stress levels to get the parameters needed for the simulation and to make a first check of their time response. During these tests, the resistivity of the wire is measured in order to understand its behaviour at different stresses, since it would be possible to control the wires using the resistivity as feedback parameter.

In chapter 5, we describe the procedure adopted to build some glass cantilevers. Their response to the bending with SMA wires is evaluated in order to have an experimental confirmation of the simulation results. Furthermore, we test the possibility to bend a glass with two pivot along its long sides and leaning on a gel layer, by using two wires that hook it at its ends. Two of these devices are finally employed to focus a collimated laser beam and to focus objects at different distances by using a camera in order to demonstrate the feasibility of this approach.

Chapter 1

Introduction to Shape Memory Alloys

1.1 Smart Materials for actuators: why Shape Memory Alloys?

An actuator is a component of a machine that is responsible for a movement of the machine or one of its parts. Usually, an actuator needs a control system and a source of energy. Systems of actuation are, for example, hydraulic, pneumatic and electrical motors, the rack and pinion system etc. Basically, every machine or automatic system that we use needs an actuation system. Developing new system of actuation easier to control, less invasive or more efficient is one of the main issues of technology research. We define smart materials as those that convert energy between multiple physical domains. A domain is any physical quantity that we can describe by a set of two state variables. Examples of physical domains are: the mechanical domain, whose state variables are the stress and the strain of the material or the thermal domain, whose state variables are the temperature and entropy. Other examples are the electrical and magnetic domains (see tab. 1.1). Smart materials have been recently widely used for developing small actuation systems or systems in which a precise control of motion is needed. The *coupling* between two domains occurs when a change in the state variable in one physical domain causes a change in the state variable of a separate physical domain. For example, changing the temperature of a material, which is a state variable in the thermal domain, can cause a change in strain, which is a mechanical state variable. This type of coupling is called thermomechanical coupling because it occurs between the thermal and mechanical physical domains. Some examples of smart materials include piezoelectrics and electrostrictives (coupling of mechanical with electric fields), piezomagnetics and magnetostrictives (coupling of mechanical with magnetic fields), and shape memory materials (coupling of thermal with mechanical fields).

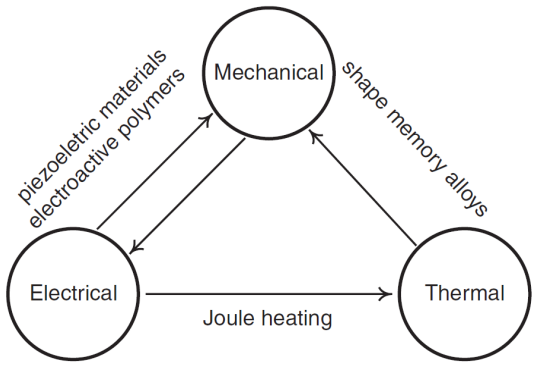

Figure 1.1: Example of physical domains and their coupling by some smart materials

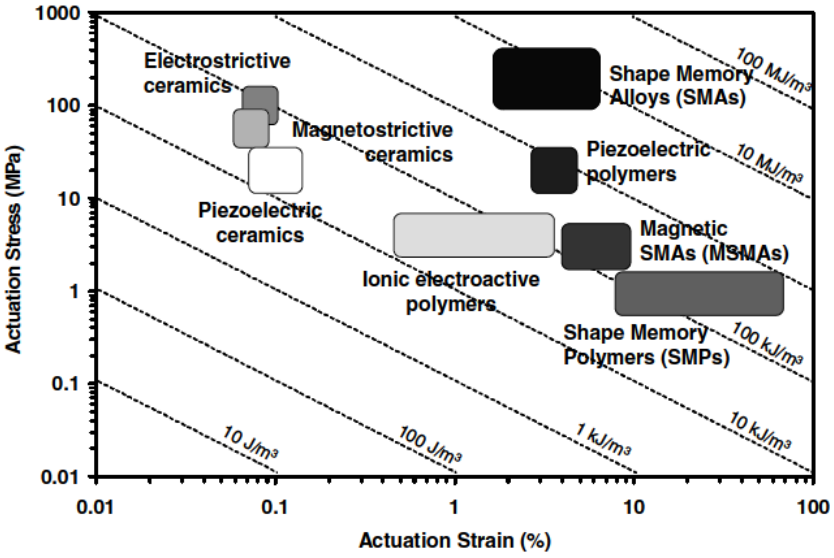

Figure 1.2: Comparison of stress and strain limits for different smart materials. Dotted lines represent *loci* with constant actuation energy density. [1]

Piezoceramics and piezoelectric polymers produce an electrical displacement when a mechanical stress is applied and can produce mechanical strain under the application of an electric field, *i.e.* they can convert an electric signal in a mechanical response and *vice versa*; this is called *two-way coupling*. Shape Memory Alloys have the ability to return to their original shape when heated above a temperature threshold with very large strains. They produce a mechanical deformation when heated, but do not show an appreciable change in temperature due to mechanical stress; in such case we talk about *one-way coupling*.
Piezoelectrics materials, SMAs and other smart materials have been widely used in engineering applications as sensing or actuating materials. Engineering design often requires materials that have a high elastic modulus(Pa) and are lightweight. For the same applied force, materials with a higher elastic modulus will undergo less deformation than materials with a lower one. The SMA behaviour is characterized by a the coupling between temperature, force and displacement. However, the last two are examples of *extrinsic properties*, i.e. that are a function of the geometry of the material or device. As we shall see, it is often useful to compare materials by certain *intrinsic properties* that do not depend on geometry. Intrinsic material properties that are important for actuator comparisons are the stress and strain that are produced by the applied stimulus. *Stress* is defined as the force applied per unit area ($N/m^2 = Pa$), and *strain* is defined as the change in a dimension over the original size of the dimension ($\frac{m}{m}$ or %).
A general comparison of piezoelectric materials, shape memory alloys and other smart materials is shown in fig.1.2 as the plot of the maximum stress of the material on the vertical axis versus the maximum strain produced on the horizontal axis [1]. Shape memory alloys are the materials

Physical domain	Mechanical	Electric	Thermal	Magnetic
State variables	Stress Strain	Electric field Electric displacement	Temperature Entropy	Magnetic field Magnetic flux

Table 1.1: Main physical domains and associated state variables

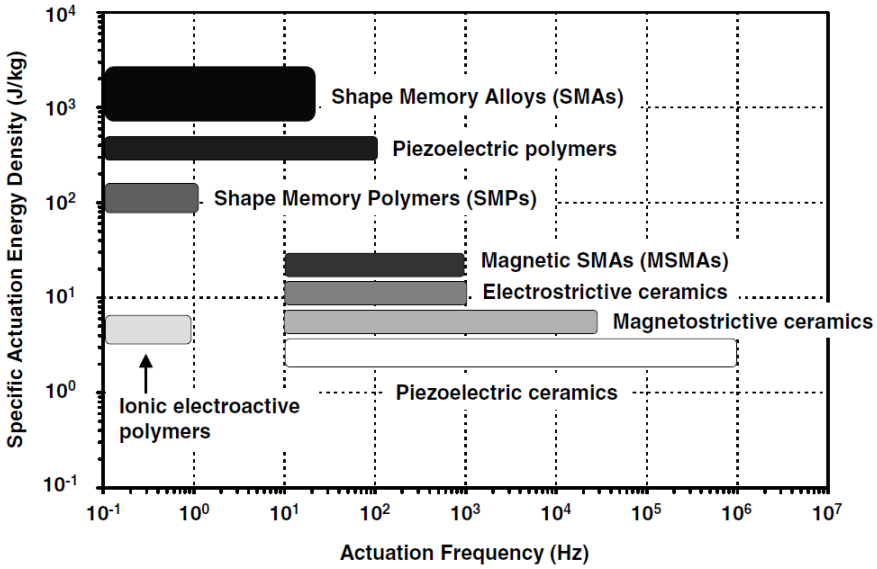

Figure 1.3: Comparison of frequency limits for different smart materials. [1]

that push farthest into the upper right part of the diagram, due to the fact they can produce large strain with large stress. A parameter used to compare different actuation materials is the *actuation energy density* defined as the work for volume unit, in other words, it is the product of strain and stress. The energy density of a material can be visualized in fig.1.2: a straight line drawn from the upper left to the lower right of the plot. Each line represents a line of constant energy density. Materials in the upper right portion of the plot are materials that have higher energy density and thus have a larger work capacity per unit volume.
An other important parameter in actuation applications is the speed of response of the used actuation material. The rate of change of the strain (displacement or stress) as response of a step change in the applied stimulus is commonly considered as measurement of the speed (obviously it depends on the step). The time response of shape memory alloys is limited by the speed at which the stimulus can cause changes in the molecular structure of the alloy. The response speed is generally limited to a time scale of 10 to 100 milliseconds [2], three to four orders of magnitude smaller than that of piezoelectric material. A general comparison between the actuation frequencies allowed by different actuation materials is shown in fig.1.3 ([1]).
SMAs are the smart materials that show the largest strain (from 4% to 8% [2]) at high values of stress, and can be shaped in several geometries among which wires, ribbons, bars, springs, etc.

1.2 A brief history introduction

The discovery of the first shape memory alloy, NiTi, occurred in 1963 by Buehler and coworkers while investigating materials useful for heat shielding [3]. It was noticed that, in addition to its good mechanical properties, comparable to some common engineering metals, the material also possessed a shape recovery capability. Following this observation, the term "*NiTiNOL*" was coined for this NiTi material in honour of its discovery at the Naval Ordnance Laboratory (NOL). The term Shape Memory Effect (SME) was given to the associated shape recovery behaviour [4].
In 1965, studies of F.E. Wang, W.J. Buehler and S.J. Pickart [5] showed that the addition of a third alloying element such as Co or Fe to the existing NiTi system caused a dramatic decrease in the SMA transformation temperatures. The new alloys inspired the first commercial SMA

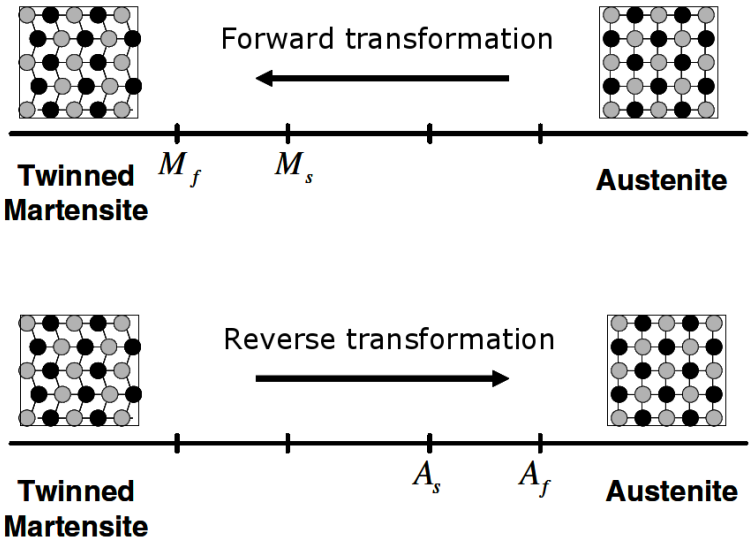

Figure 1.4: Forward transformation and reverse tranformation induced respectively by cooling and heating the SMA with no applied load. The x-axis represents temperature. M_F, M_S, A_S and A_F are martensitic finish, martensitic start, austenitic start and the austenitic finish temperatures, respectevely. (Adapted from [1])

application, known as Cryofit, where SMA material was used for pipe couplings in F-14 fighter aircraft [6]. The transformation temperatures for Cryofit were so low that, to prevent actuation from occurring before the assembly, the pipe couplings were transported in liquid nitrogen.
Since the initial discovery of Nitinol in 1963, many commercial applications have been developed. During the 1970s, several uses of NiTi in biomedical applications appeared, but it wasn't until the 1990s that NiTi stents made their commercial breakthrough. By this time, SMAs had found additional applications in air conditioning vents, electronic cable connectors, valves and a variety of other products. In addition, over the last decade, the demand for actuation under high temperature operating conditions driven by the aerospace and oil industries, has revived a great deal of interest in the research of SMA. At present, NiTi remains the most used shape memory alloy.

1.3 Phase Transformations in Shape Memory Alloys

In shape memory alloys, the shape change occurs concurrently with a phase change. This is why the transformations of SMAs are usually represented by a phase diagram. A metallurgical phase diagram for a metallic alloy is a schematic representation of the equilibrium conditions between distinct phases. Phase diagrams consist of equilibrium lines or phase boundaries that separate different phases from each other. SMAs have two phases, each one with a different crystal structure and therefore different properties:

- *Austenite* is the high temperature phase (generally characterized by a cubic crystal structure).
- *Martensite* is the low temperature phase (generally characterized by a monoclinic, orthorhombic or tetragonal crystal structure).

Each martensitic crystal formed can have a different orientation direction, called a *variant*. The assembly of martensitic variants can exist in two forms: *twinned martensite* or *temperature induced martensite*, which is formed by a combination of "self-accommodated" martensitic variants, and *detwinned martensite* or *stressed induced martensite* in which a specific variant is dominant.
The transformation from one structure occurs by shear lattice distortion as usually happens in metals. Such a transformation is called *martensitic transformation*. Upon cooling in the absence of an applied load a rearrangement of the variants occurs with no macroscopic shape change, resulting in a transformation from austenite to twinned martensite. This transformation is called *forward transformation*. A further explanation of the transformations form the crystallographic point of view can be found in section 1.5
When the material is heated from the martensitic phase, the crystal structure transforms back to austenite, again with no associated shape change. This transition is called *reverse transformation*.
As said before, the transformation is temperature-dependent, four characteristic temperatures associated with these transformations can be defined: during the forward transformation with no load, austenite begins to transform at the *martensitic start temperature (M_S)* and completes its transformation at the *martensitic finish temperature (M_F)*. Similarly, during heating, the transformation begins at the *austenitic start temperature (A_S)* and is completed at the *austenitic finish temperature (A_F)*. A scheme of these transformations is shown in fig. 1.4.

1.3.1 Shape Memory Effect

If a mechanical load is applied to the material in the twinned martensitic phase (at a temperature below M_F), it is possible to detwin the martensite by reorienting a certain number of variants (see fig.1.5). The minimum stress required for detwinning start is called the *detwinning start stress (σ_S)* while the stress that is necessary to complete detwinning is termed the *detwinning finish stress (σ_F)*. The detwinning process results in a macroscopic shape change. When the load is released, the strain of the material (along the direction of the applied stress) reduces to that called *residual strain*. Heating the material over the austenitic final temperature leads to a complete shape recovery that is maintained upon the cooling. This behaviour is called *Shape Memory Effect* (SME).
If the material is cooled down with an applied load, the transformation leads to a detwinned martensitic phase with a consequent shape change. Reheating the material implies a shape recovery. Under these conditions the recovery is not complete but the material in the austenitic phase has a residual deformation which depends on the Young's Modulus of the material. The Young's Modulus is different in the austenitic and martensitic phase and has intermediate values when both phases are present.
Irrespective of the nature of the applied load, i.e. tension or compression, the transformation temperatures increase with an increase in the magnitude of the load. Under an applied uniaxial load with a corresponding stress, σ, the new transformation temperatures are represented as M_F^σ, M_S^σ, A_S^σ and A_F^σ for martensitic finish, martensitic start, austenitic start and the austenitic finish temperatures, respectively. The dependence of the transition temperatures from the applied stress is linear as can be seen in the diagram in fig.1.6.
The nature of the SME can be better understood by following the thermomechanical loading path in a combined stress-strain-temperature space as shown in fig.1.7. In this scheme is represented a typical shape memorty effect path for a NiTi specimen under uniaxial loading [1]. The uniaxial stress on the specimen due to an applied load is represented by σ. While the corresponding strain ϵ is the change in the length of the specimen along the direction of applied load, normalized by the original length.
Starting from the austenitic phase (point A in fig.1.7), the stress-free cooling of austenite below

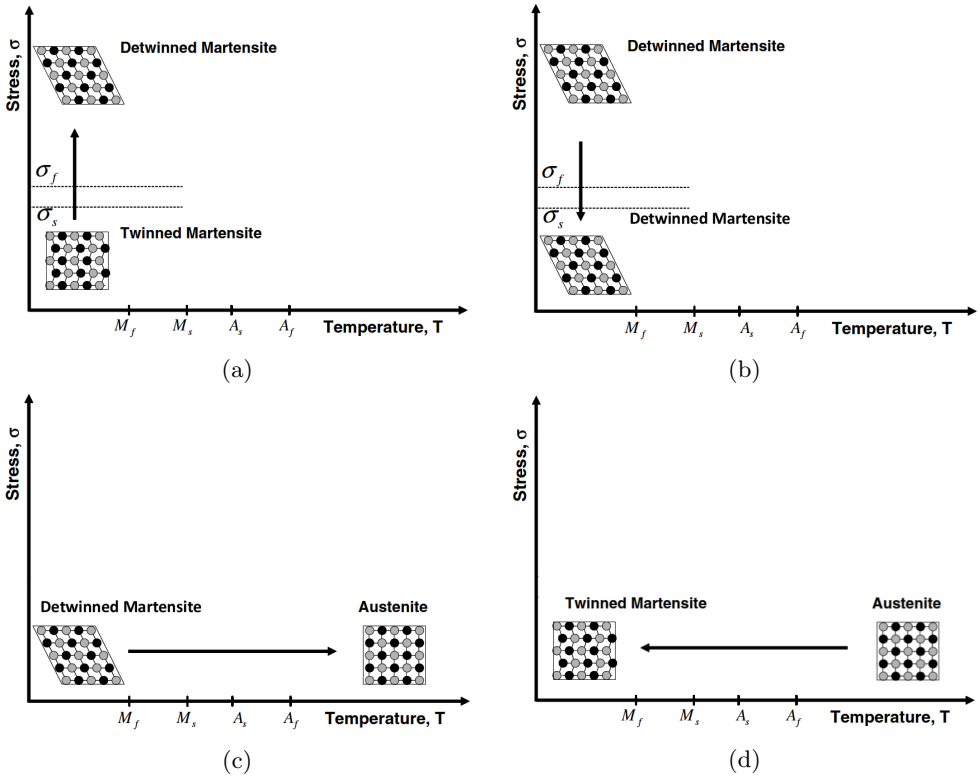

Figure 1.5: Transfomations of the Shape Memory Effect (SME). (a) Detwinning of the material with an applied stress. (b) Unloading of the material. (c) Reverse transformation leads to a shape change. (d) Forward transformation leads to the initial condition of twinned martensite with no shape change occurred.

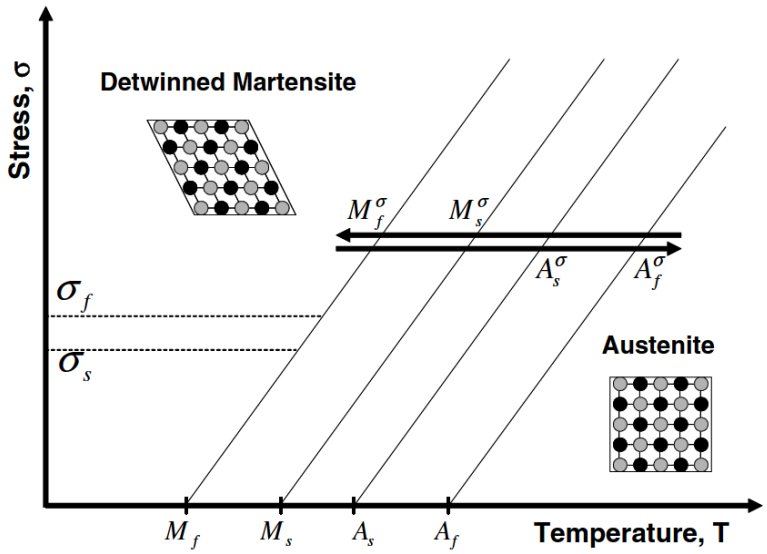

Figure 1.6: Forward and reverse transitions with applied stress.

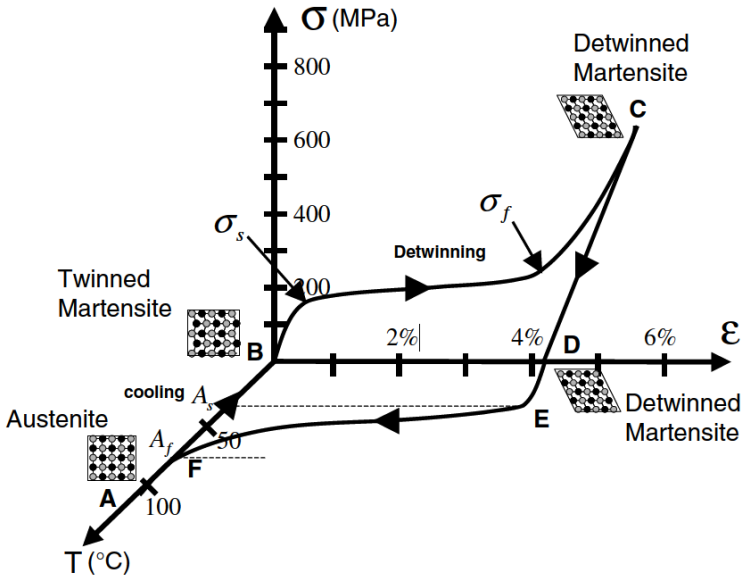

Figure 1.7: Stress-strain-temperature diagram with a shape memory path for a typical NiTi SMA. [1]

the forward transformation temperatures (M_S and M_F) results in the composition of twinned martensite (point B). When the twinned martensite is subjected to an applied stress that exceeds the start stress level (σ_S), the reorientation process starts, with the growth of a certain favourably oriented variant. The detwinning process is completed at a stress level σ_F, that is characterized by the end of the plateau in the $\sigma - \epsilon$ diagram (see fig.1.7). If the material is further stressed it strains proportionally to the applied stress with proportional constant $1/Y_m$ (where Y_m is the martensitic Young's modulus). The material is then elastically unloaded from C to D and the detwinned martensitic state is maintained with a certain residual strain. Upon heating in the absence of stress, the reverse transformation initiates as the temperature reaches A_S (point E) and is completed at the temperature A_F (point F). In the absence of permanent plastic strain generated during detwinning, the original shape of the SMA is recovered (point A).
Subsequent cooling to martensite will again result in the formation of self-accommodated twinned martensitic variants with no associated shape change, and the whole cycle of the SME can be repeated. The above described phenomenon is called *one-way shape memory effect* because the shape recovery is achieved only during heating after the material has been detwinned by an applied mechanical load.

1.3.2 Pseudoelastic Effect

In addition to thermally induced phase transformation, a transformation between the two phases can also be induced by applying a sufficiently high mechanical load to the material when it is in the austenitic phase. If the temperature of the material is above A_F, a complete shape recovery is observed upon unloading. This behaviour is called the pseudoelastic effect. A loading path demonstrating the pseudoelastic effect is shown in fig.1.8a while the associated macroscopic shape change due to the applied load is reported in a schematic strain-stress diagram in fig.1.8. The stress levels at which the martensite transformation initiates and completes are denoted by σ_{M_S} and σ_{M_F}, respectively. Similarly, when the SMA is unloaded, the stress levels at which the material starts and completes its reverse transformation to austenite are denoted by σ_{A_S} and σ_{A_F} , respectively. If the material in the austenitic phase is tested above the M_S temperature, but below the A_F temperature there is only a partial shape recovery.

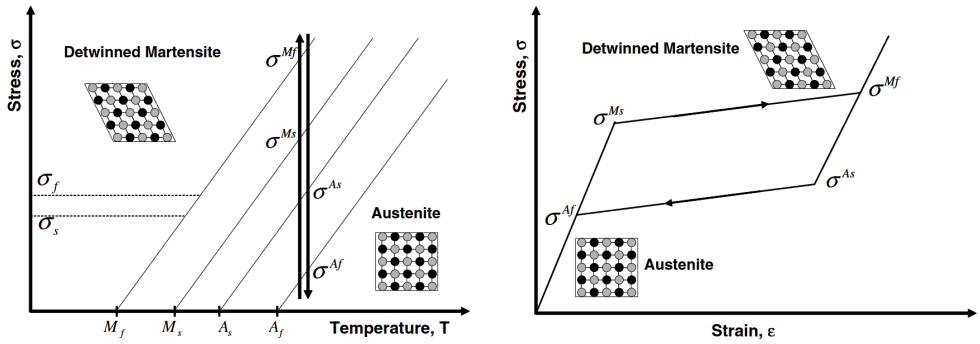

Figure 1.8: The Pseudoelastic Effect (PE). (a) A pseudoelastic loading path. (b) A schematic representation of stress-strain diagram for a pseudoelastic transformation.

Twinned and detwinned martensite can be also classified as *temperature induced* and *stressed induced martensite*. That's because former is obtained cooling down austenite with no (or small) stress applied, while the latter is obtained cooling down austenite when a stress greater than σ_F is applied to the material.

1.3.3 Two-way shape memory effect

The discussion presented so far regards the one-way SME behaviour in SMAs. In particular cases, however, an SMA can exhibit repeatable shape changes under no applied mechanical load when subjected to a thermal or stress cycling. This behaviour is named *two-way shape memory effect* (TWSME). The TWSME can be observed in a SMAs which has undergone repeated thermomechanical cycling along a specific loading path (in a process called *training*). Repetition along a loading path for a large number of cycles can induce changes in the microstructure, which causes macroscopically observable permanent changes in the material behaviour. Training a SMA refers to a process of repeatedly loading the material following a cyclic thermomechanical path until the hysteretic response of the material stabilizes and the inelastic strain saturates. The training can be done with a thermal cycle under a certain load (fig. 1.9a) or a load cycle in the pseudoelastic regime (fig. 1.9b); in either cases, during the first cycle there is only a partial recovery while a permanent strain accumulates after each consecutive cycle until it begins to gradually decrease and the hysteresis path remains the same.

1.4 Cyclic Behaviour and fatigue in SMAs

Since SMAs are widely used in actuation application it is very important to understand how these materials behave after multiple cycles. The fatigue behaviour of SMAs depends on the material processing (fabrication process, heat treatment, etc.), the type of loading conditions (applied stress, strain, temperature variations, environment, etc.), and transformation induced microstructural modifications (e.g., defects on grain boundaries due to strain incompatibilities). As said in the previous section, cycling SMAs produces microstructural changes. Those have the effect to reduce the fatigue of the material as opposed to high fatigue most commonly observed in loading paths operating in a purely elastic regime of a material. Mechanically induced fatigue behavior of SMAs is typically examined by performing rotating bending tests or by mechanically cycling the material on the load frame between two stress or strain levels along a given loading

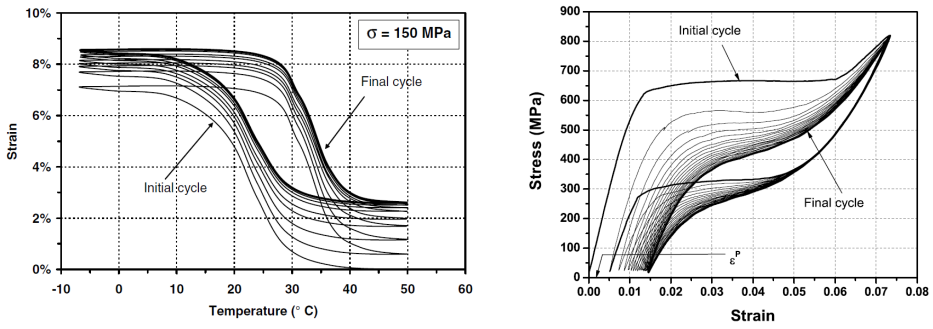

(a) (b)

Figure 1.9: 1.9a Thermal cyclic loading (50 cycles) of a NiTi shape memory alloy wire under constant load of 150MPa [7]. 1.9b Pseudoelastic response of an *as-received* NiTi wire with $A_F = 65°C$, tested at a temperature of $70°C$. Also shown is the stabilized pseudoelastic hysteresis loop after 20 cycles [1].

path [7]. The transformations can be complete or partial, i.e., the two states between which the material is cycled correspond to mixed phase states (partially martensitic and partially austenitic). In the second case the fatigue is much more evident. In fig. 1.11 a scheme of how the strain and the stress influence the fatigue of NiTi wires with a diameter of the order of $10^2 \mu m$ can be seen.

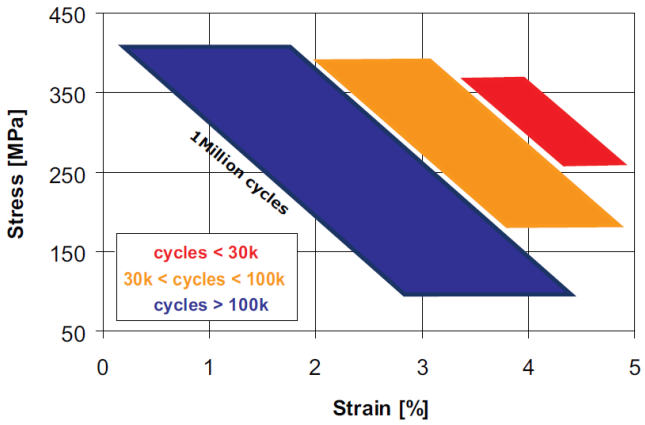

Figure 1.10: Life cycles depend on a stress-strain trade-off. A strain increase needs a stress decrease to achieve a good fatigue performance [8]

1.5 Cristallography of SMAs phases

Since the transformations of SMAs occur by a crystallographic phase change, it is interesting to better understand the crystallography of such materials. The *habit plane* is defined as the plane that physically divides the two phases and it is the plane along which the shear distortion occurs; for this reason it is also called the *lattice invariant plane*. In general the transformation form austenite to martensite can take place in two ways called *lattice invariant shear* mechanisms:

1. Through slip (atoms move of one or more atomic space)

2. Through *twinning* (atoms move of a fraction of an atomic space).

Both mechanisms do not involve a volumetric change of the material while the strain associated with this transformation is called *lattice invariant strain*. In SMAs twinning is the more common method.
The austenitic crystallographic structure is commonly cubic while that of the martensite depends on the alloying of the material; for NiTi the structure is monoclinic, when Cu or Pd are added the structure is orthorhombic. In SMAs, during the transformation from austenite to martensite, every martensitic unit cell that is formed can have different crystallographic orientations with respect to the cubic parent phase, and each unit cell having a different orientation is called a *variant*. The number of variants that can form depends on the crystal structure of the martensite and its lattice correspondence with the parent phase unit cell.
An example of this can been seen in the NiTi alloy where there are "twin" planes along which twinning can occur. In the cubic lattice of the parent austenitic phase, the twinning shear can occur along the [011] planes to obtain the crystallographic equivalent martensite twins. Since there are six such of [011] planes and two directions for the twinning to occur along each plane, there exist 12 equivalent martensitic twins. Each twin is composed of two martensitic variants, which, due to the shear distortion during transformation, assume a mirror symmetry. As a consequence of this, there are 24 total martensitic variants in most NiTi systems.
Let's see from a crystallographic point of view the two processes at the basis of the shape memory and pseudoelastic effects of shape memory alloys:

- **Austenite to Twinned Martensite**
  When austenite, under zero or very little stress, transforms to twinned martensite, there is no associated shape change. The martensite that forms along the habit plane, under zero or little stress, occurs by twinning and the twins that form arrange themselves in a unique patterns to minimize the overall strain energy due to transformation. This behaviour is known as the *self-accommodation* of twinned martensite.

- **Twinned Martensite or Austenite to Detwinned Martensite**
  When the self-accommodated martensitic structure (monoclinic, orthorhombic or tetragonal) is subjected to an applied load, a shear stress acts on the twin plane. When the shear stress reaches a critical value, the most preferred variant (based on orientation to the applied stress) will evolve at the expense of other variants. This process of the evolution of the favourable variant and the associated generation of the inelastic strain, at the basis of the shape memory and pseudoelastic effect, is known as the *detwinning process*. In the case of pseudoelasticity, a resolved shear stress reaches a critical value along the habit plane that leads to the formation of stress induced martensite.

As previously said, alloying determines the crystallographic structure of the material but different alloying also leads to different transition temperatures and different maximum strain. Since the discovery of NiTiNOL in 1963, the research on new possible compositions for shape memory alloys have spread and a wide variety of new alloys have been found. Shape memory alloys can be classified in different ways: the primary alloying elements, mode of actuation (thermal or magnetic), operating temperature. Transition temperatures depend on the percentages of the alloy, for example for NiTi, more Nickel means lower transition temperatures. In tab. 1.2 some examples of how different percentages of the elements that constitute the alloy influence the transition temperatures are reported. Since NiTi was the first shape memory alloy discovered, the possibility to vary the transition temperatures in a large range of values simply changing the percentages of the elements and the fact that it is the shape memory alloy with the highest strain (up to 8%) and its bicompatibility have made NiTi the most common SMA.

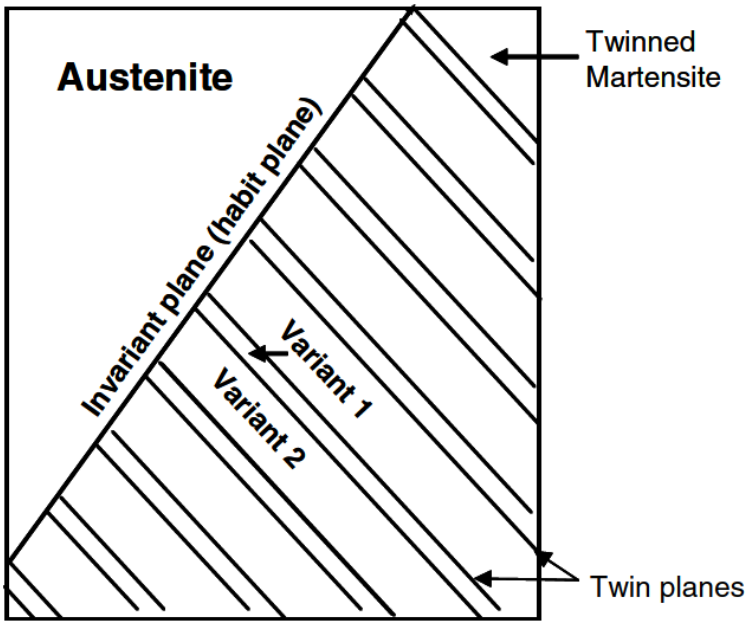

Figure 1.11: Schematic of the austenite-martensite interface in the alloy crystal [1].

Alloy	M_F	M_S	A_S	A_F
$Ti_{50}Ni_{50}$	15	55	80	89
$Ti_{49.5}Ni_{50.5}$	-78	-19	9	53
$Ti_{49}Ni_{51}$	-153	-114	-89	-40

Table 1.2: The transition temperatures of NiTi alloys depend on the percentages of the alloy element [1].

1.6 State of the Art: Applications

SMAs properties have made them very suitable for actuation applications. The shape memory effect or pseudoelasticity can be induced by an external stimulus or be controlled from the user in order to achieve the desired effect. These unique behaviours have made SMAs a material chosen in aerospace, automotive, medical and other types of actuation applications. Also commercial applications that we can meet every day exploit SMAs properties; for example pseudoelasticity is exploited to make folding the frame of eyeglasses and antennas of mobile phones or to absorb the strike in golf clubs. In some fire protection devices, the ability of SMAs to reversibly respond to changes in temperature have enabled them to find applications like safety valves. SMA actuated louvres have also been incorporated in air conditioning vents that can adjust depending on the temperature of the air exiting form the vents. The SME is also exploited in shower faucet designs where an SMA spring automatically adjusts the flow of hot and cold water to maintain a pre-set water temperature. As you can see SMAs are everywhere in our life.
In this section we will provide a sistematic overview on the main applications of SMAs in various fields (for a more systematic review on SMA applications you can see [9]).

1.6.1 Aerospace applications

- *Coupling* - One of the first applications of SMAs (1960s) was about pipe coupling in F-14 aircraft [6]. As shown in fig. 1.12, at temperatures below M_F , the couplings are expanded to a larger diameter such that it can easily slide through the pipes to be fastened . Once the SMA coupling transforms back to austenite (i.e., above Af which is generally programmed to be lower than the ambient temperature), it shrinks to its original dimension and thus securely holds the pipe ends. This method is still employed today in several applications in which pipe coupling is needed, (for example for underwater pipe or electric connectors [10] due to its vantages over other ways of couplings [11].

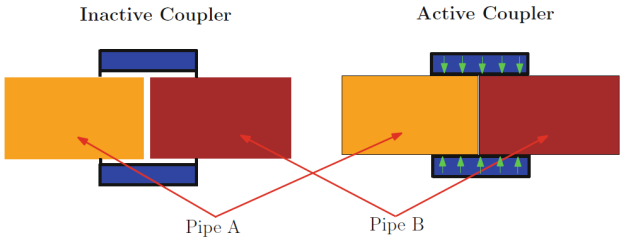

Figure 1.12: SMAs can be used as couplers that can substitute socket welds or compression fittings in aerospace, civil, oil exploration industries. The idea is to deform the couplers in its martensitic state to larger diameters for easy sliding along the pipes and then heated to temperatures above A_F to hold the ends of pipes firmly with appropriate compressive forces. [12]

- *Chevrons* - To reduce engine noise levels during take off and landing of airplanes, some designers have installed chevrons into engines to mix the flow of exhaust gases and reduce engine noise. Research is being performed into methods by which SMA beam components can be embedded inside chevrons. The SMA beams bend the chevrons into the flow during low-altitude flight or low speed flight, thereby increasing mixing and reducing noise. During high-altitude, high speed flight, these SMA beam components will cool into martensite, thereby straightening the chevrons and increasing engine performance [13]. The current Boeing design for these variable geometry chevrons can be seen in fig. 1.13.

Figure 1.13: Boeing variable geometry chevron, flight testing [13].

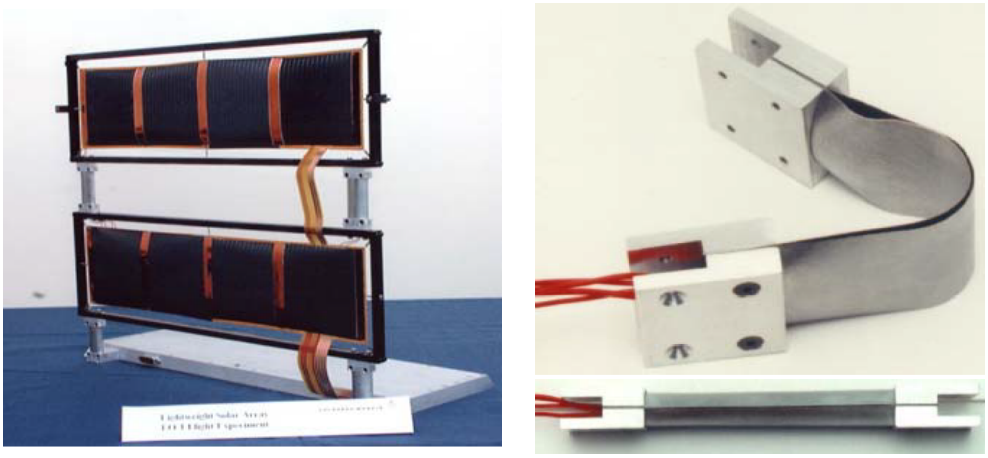

Figure 1.14: The LFSA and the SMA hinges shown in the folded and the deployed configurations

- *Spacecraft Applications* - SMAs have been used in space applications to address problems related the actuation and release in zero atmosphere environment as well as vibration damping during spacecraft launch. Most of the applications and systems are typically designed by careful experimentation. One such application that uses SMAs is for the low-shock release mechanism in satellites [14], indeed it was estimated that until 1984 a great number of spatial failures were due to shocks caused by the explosive method for the release that was used. A new method for the release was employed using SMA wires. In normal conditions, strained SMA wires hold together the components; when the release has to occur, SMA wires are heated, this causes an applied force which break the wires such that the two components split up with no damages.
  The Lightweight Flexible Solar Array (LFSA) [15] used thin SMA strips as hinges, which deploy the folded solar panels upon heating in approximately 30 seconds. The proof of concept design is shown in Fig. 1.14.
  As stated in [16], SMA wires could be used to adjust the "trailing edge tab" of a helicopter as reported in fig. 1.15. An other study proposed the use of SMA torque tubes to vary the twist of rotor blades, as found on tiltrotor aircraft [17]. SMAs are ideally suited for such applications because of their high actuation energy density and forces required in the small available volume within a rotor blade.
  In addition to actuation, another attractive application for SMAs is vibration isolators and dampeners [18]. The hysteresis in the pseudoelastic behaviour is representative of the mechanical energy that a SMA can dissipate during a cycle. Further, the change in the stiffness from the initial elastic region to that in the transformation region makes it an effective tool to isolate vibrations.

1.6.2 Automotive applications

The employement of sensors and instruments for safety and comfort in modern vehicles has recently spread. The pseudoelastic behaviour hysteresis provides an effective system to dissipate vibrations and impact. SMA panels have been used for impact absorption instead of kevlar ones on armor vehicles in military [19] and commercial applications [20]. The SME has also been implemented for actuating blinds that cover the fog lamp to prevent damage. A series circuit

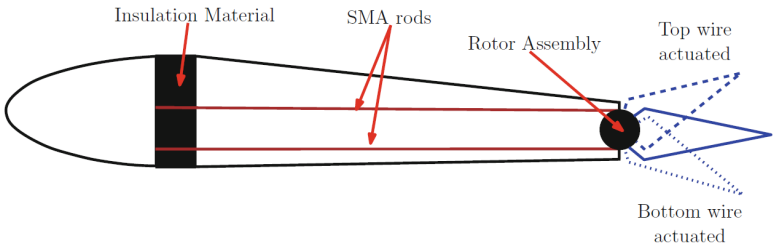

Figure 1.15: The use of pretwisted SMA rods to torsionally actuate blade tabs between two angular positions is possibility by differentially heating of top and lower SMA rods. This way the angular positioning of "trailing edge tab of a helicopter rotor" can be adjusted and thus allowing for user inflight tracking of its position.

ensures the actuation of the SMA louvres every time the fog lamps are turned on.
SMA wires has been considered a valid alternative to electromagnetic actuators as sensors or for actuation systems triggered by temperature changes. An application that exploits this behaviour is the SMA spring for the continuous variable transmission in the Mercedes A class. The spring acts as a sensor that monitors the temperature and actuates a valve at a specific temperature, which changes the direction of oil flow. A similar actuation system is incorporated in the Shinkansen bullet train gearbox where the temperature in the gear box is monitored and an SMA spring actuates a valve to adjust the oil level in the gearbox [21]. An other sensing applications is a cost effective side mirror actuator [22].

1.6.3 Robotics applications

Shape memory alloys have been employed in robotics as actuating system instead of electric servomotors due to their low invasiveness, lightness, absence of vibrations and noise, low power need, high energy densities. For example they have been used to develop several prototypes of mechanical hands. In [23] has been showed how SMA wires can be used to control the movements of an artificial arm with significant improvements respect to electrical motors. The actuation system constists of SMA wires bounded to the artificial tendons of an arm, with bias springs, and controlled with a current input. A small prototype of a prostetich hand controlled with SMA wires has been developed in [24] for dexterous manipulation of small tissues and parts in medical and industrial fields. The dimensions of the device are about a third of a human hands. The step response of the hand is about 200ms, a time comparable with that of human reaction, and the frequency of movements can reach 4 Hz. In this case the actuation systems consists of two antagonistic SMA wires instead of a wire and a spring. The developed prototype has shown the ability of power and precision grasping those are typically requested to a mechanical hand (see fig. 1.16b).
SMA wires have also been employed to move an insectlike robot with six legs [25]. The actuation system has been exploited in two ways: using two antagonist SMA wires or using gravity as bias force for the actuation system. Simple on-off control of actuators (fully stretched-fully contracted wires) was used to control the miniature six-legged robot which is shown in fig. 1.16a. Also different models of flying robots have been proposed or developed using SMAs, like the bat inspired "Bat-robot" in [26, 27] and the dragonfly inspired "BionicOpter" in[28].

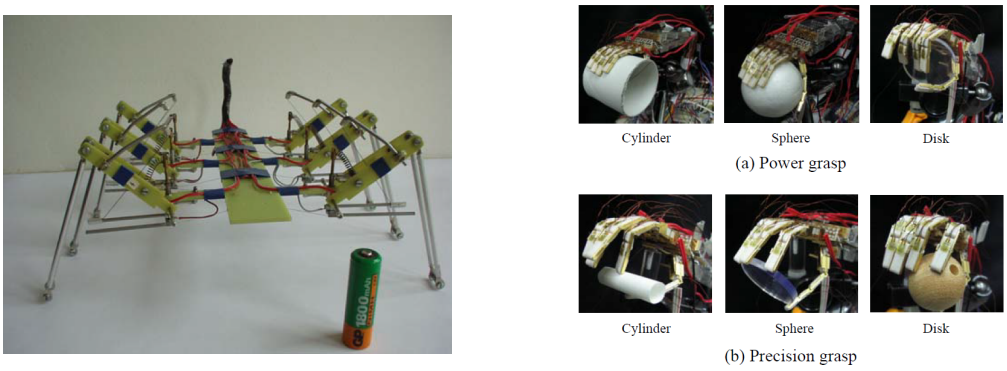

(a) (b)

Figure 1.16: (a) Six-legged robot controlled with SMA wires. (b) Grasping test on a mechanical hand controlled by SMA wires.

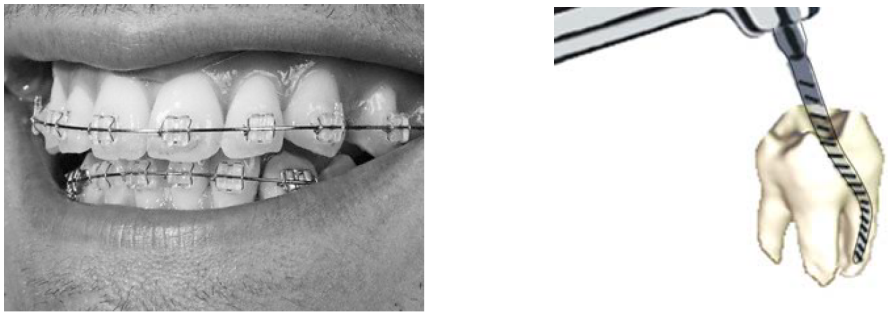

(a) (b)

Figure 1.17: Orthodontic applications of SMAs. (a) Orthodontic NiTi archwires. (b) Schematic representation of a SMA drill for dental root surgery.

1.6.4 Medical applications

Some first applications of SMAs were in the medical field. An important requirement for a SMA, or any other material to be used in the human body, is that to be biocompatible. Biocompatibility is a property of the material to remain nontoxic through its functional period inside the human body. Several analysis have focused on each individual element that constitutes the alloy: nickel and titanium and tested NiTi biocombatibility with positive results [29]. We report some of the principal and more important medical applications of SMAs.

- *Orthodontic applications* - Nitinol orthodontic archwires have been used since the 1970s [30], and are more effective than other alternative materials. The advantage of SMA archwires is that, working in the pseudoelasticity regime, a small change of stress leads to a big change of strain while in a linear elastic material such stainless steel, a small strain change will imply a strong force on theeth but with a small amount of corrective strain. So, using SMA archwires is possible to apply a constant force to theeth and for a longer time respect to archwires made of other materials.
  Another dental application for SMAs involves the use of NitiNOL drills used in root canal surgery, which needs careful drilling within the tooth. The advantage of these Nitinol drills is that they can bend to rather large angles, which induce large strains, maintaining the high velocity of rotation 1.17b.

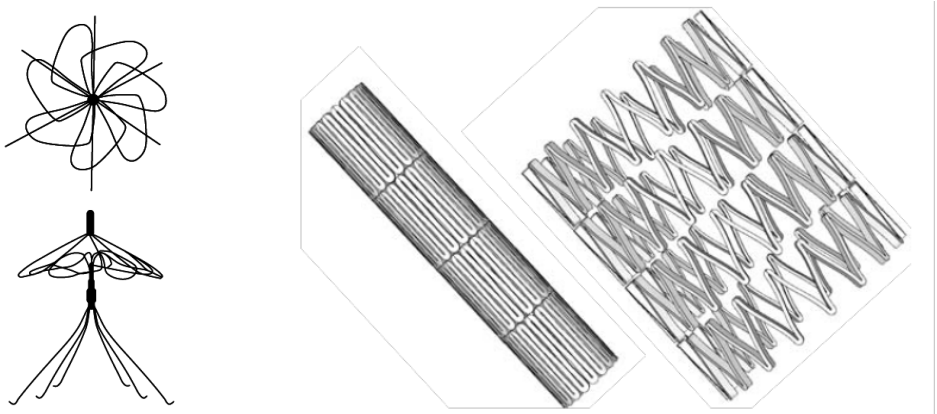

(a) (b)

Figure 1.18: Medical applications of SMAs. (a) Simon filter. (b) NiTi stent for cardiovascular surgery

- *Cardiovascular applications* - Shape memory effect is exploited in cardiovascular application. The idea that undergoes all cardiovascular application is to deform the material in the martensitic phase. Then, when it will be inserted in the human body, temperature will rise over A_F and the material will deform.
  One of such applications is the *Simon Filter* (fig. 1.18a), a device that acts as a filter that traps clots traveling in the blood stream. The trapped clots are then eventually dissolved. It is inserted in blood vessel within a catheter and the rise of temperature make it expanding to its original shape.
  A more common cardiovascular application is the "self-expanding" NiTi stent (fig. 1.18b). Like other conventional stents, this device is used to support the inner circumference of tubular passages in the body such as blood vessels those would collapse in its absence. As the Simon Filter, it is inserted within catheters in its contracted form and then, and then, when realised into blood vessels it expands preventing the vessel to collapse. The device is generally laser cut from sheets or tubing and is then shape set to the appropriate diameter.

- *Orthopedic applications* - The devices developed for orthopaedic applications are used to support injured, weakened or fractured bones. One such device is the spinal vertebra spacer, used to provide local reinforcement to the vertebrae and prevent motion during the healing process. The device applies a constant force on the joint while providing flexibility (both SME and pseudoelasticity are involved). SMAs represent a different kind of material form and can be used as artificial bone implants. They are used for staples and shape memory plates. Staples are installed in a open configuration at a fractured joint. Then heated by the temperature of the human body they provide a force on the two adjacent bones holding them together. Shape memory plates are used when cast cannot be applied over the fracture surface (facial areas, jaw, nose, etc.). The principle is similar as before.

- *Catheter and endoscope actuation* - SMAs have been successfully used as actuation material to bend and torque catheters and endoscopes. As explained in [31], several actuation systems have been proposed and used.
  One of this consists in a bending mechanism realized by thin NiTiNOL SMA plates: one of the SMA plates fixed along the side of the catheter bends when it is heated by application

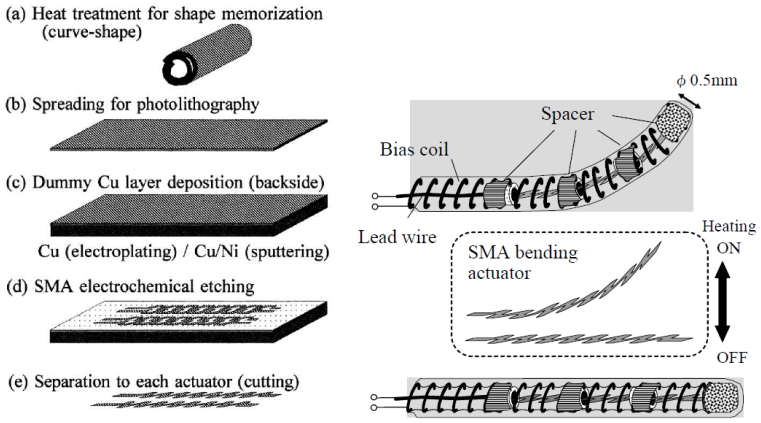

Figure 1.19: Scheme of "meandering-shaped" SMA actuators fabrication for active endoscope.

of a current. To realize precise control of bending motion was employed a feedback control monitoring temperature. Other applications used SMA wires or SMA coils heated directly (through current) or indirectly to reduce the power needed (by additional heater lines with high resistance). An other interesting method is to use flat "meandering-shaped" SMA actuators (see fig. 1.19).

1.6.5 Applications of SMAs in optics

In this section we report some applications that SMAs have found in the optical field. Especially the shape memory effect has been used for application of position control of optical elements and shape morphing.

- *Automatic alignment of an optical system* - One of the first applications exploited SMAs properties to align the elements of an optical system [32]. A SMA foil has been used to control the position of a pinhole through a current input and position feedback. Precision at the level of the optical wavelength was realized retaining a large displacement of 1 mm.

- *NiTi film as optical switcher* - In [33] has been shown how the reflectivity of a NiTi film changes of a large factor (45%) between the austenitic and martensitic phase. These changes are due to the changes in the surface roughness and also in the refractive index of the material when it undergoes a phase transformation. The authors suggested the possibility to use the NiTi films as devices with a nonreflecting surface at room temperature and with a reflecting surface when heated.

- *Surface actuation of lightweight mirrors* - Processing-induced errors and surface errors due to temperature excursions and gravity sag (zero gravity in space) make it impossible to correct the surface of thin mirror face-sheets by conventional point actuators. An experimental study was conducted to explore the possibility to employ SMA wires to correct the shape of lightweigth mirrors for spatial applications [34]. Prestressed SMA wires were attached behind these mirror prototypes and used to actuate a composite beam; the movements were monitored using a Moiré interferometer. It has been shown that the magnitude of actuation is significant (50%) so that such a system could be employed to correct gravity sag and low frequency temperature distortions by an order of magnitude.

Recently SMAs entered in the development of small or even micro systems for lens actuation and several patents have been registered about *Optical Image Stabilization* (OIS) systems or auto-focusing for microcameras, especially to be used in mobile phones.

- *Optical Image Stabilization* - For example the *TDK Hutchinson technology* developed an OIS system employing SMA wires for tilting a microcamera lens [35]. OIS systems are far spreading in the development phone cameras; they permit to correct the hand shacking of the user improving the image quality, particularly in low light conditions. The OIS system of TDK consists of four SMA wires along the sides of the device which can tilt a lens in front of a camera according to data from a gyroscope. Resistance feedback control is provided. The dimensions of the whole device can be reduced to a 8.5 mm footprint, allowing the use as image stabilizer for phones. Respect to other methods of image stabilizations that with SMA wires has several advantages: best performance in smallest footprint (SMA wires with diameter of $25\mu m$, no position sensors or magnets, small footprint, low camera consumption), high capacity (manufactured using automated processes, ability to scale to high volumes quickly by replicating equipment), lowest cost (SMA resistance feedback, highly automated).

- *Auto-focusing device* - In addition to the OIS system also several autofocusing devices has been developed using SMA wires. One of this acuators is composed by a "V-shape" SMA wire actuator whose extremes are attached to a lens carrier provided with a guide pin. When the V-shape wire is heated, it contracts moving the lens carrier along the optical axis. The lens carrier compress a bias spring which ensures that when the wire cools down the lens carrier returns to initial position. It is possible to control the position of the lens through a current input with the feedback of a "Hall sensor" [36]. With a similar method which employs more than one wire it is possible to obtain a device which makes auto-focus and OIS at the same time [37] (see fig. 1.20b).

Shape memory alloys have been also used to develop different prototypes of deformable lenses with a variable focal length. We will discuss about this devices in the next chapter 2.

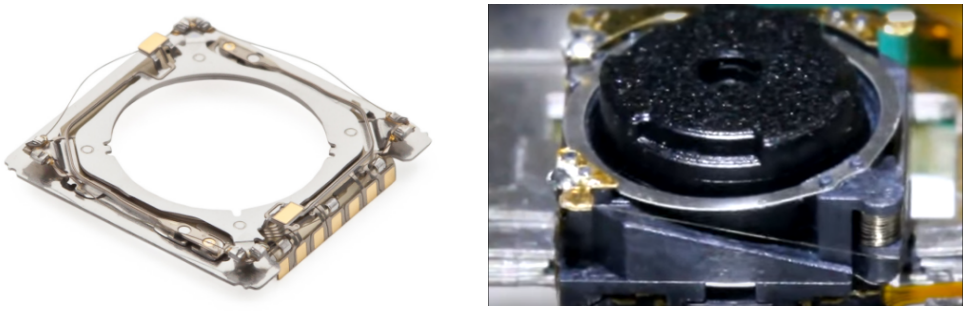

(a) (b)

Figure 1.20: Examples of OIS and auto-focusing systems. (a) OIS system employing SMA wires for the actuation. [35]. (b) Auto-focusing and OIS system employing SMA wires [37].

Chapter 2

Adaptive Lenses

In this chapter we will firstly present simple lenses and the aberrations that characterize them. We will then introduce what are the main issues that adaptive optics deals with and present the principal types of adaptive lenses that have been developed until now.

2.1 Simple lenses

Lenses are among the most used and important devices in optics. They are widely used in vision correction, imaging processing, optical communication, information storage, industrial and scientific applications like cameras, telescopes and microscopes, projectors, laser printers and many more. The most used are solid lenses. Solid lenses are typically made of glass, plastic, polymers or polycarbonate. From a geometrical point of view a *simple lens* is composed by two refractive surfaces with axial symmetry. For simple lenses, the focal length is fixed, once the lens have been produced. Conversely, a *compound lens* is a collection of at least two simple lenses which are arranged one after another with a common axis and it's used when a variable focal length is required. The focal length can be adjusted moving the lenses along the optical axis with a mechanical system.
Optical lenses made of solid materials exhibits very good optical performances. The surface of a solid lens can be fabricated with a $\lambda/40$ precision, thanks to the magneto-rheological finishing technique (MRF), also with aspherical shapes. The selection of materials for fabricating lenses is very wide and permits to optimize the performances of the lens by choosing the appropriate refractive index and dispersion. Solid lenses can also be fabricated with different aperture sizes: from the several hundred of micrometers aperture of the lenses used for CD and CD-ROM readers to the large lenses employed in telescopes (up to 1 m diameter). Solid lenses have several other advantages, such as broadband transmission, high transmittance, especially after the application of anti-reflection coatings, and high thermal and mechanical stability.

2.2 Optical aberrations

However, solid lenses have some inherit issues. For instance, the surface profile of a singlet lens is fixed once the lens is produced. As stated before, two or more lenses are required to change the focal length, thus the system is often bulky and heavy. It is inefficient to adjust the focal length of a compound lens because the driving mechanism of the lens system is mainly mechanical. Moreover, the dynamic response is intrinsically slow, due to the inertial forces generated when moving bulky mechanical parts. Simple and compound lenses present an other important problem, i.e. aberrations. Typically the surfaces of the used lenses are portions of

spherical surfaces and the properties of the lenses are derived on the basis of the Snell's law of refraction:

$$n_i sin\theta_i = n_t sin\theta_t \tag{2.1}$$

With the Taylor's expansion the equation can be written as:

$$n_i(\theta_i - \frac{\theta_i^3}{3!} + \frac{\theta_i^5}{5!} + ...) = n_t(\theta_t - \frac{\theta_t^3}{3!} + \frac{\theta_t^5}{5!} + ...) \tag{2.2}$$

Keeping only the first term of the Taylor's expansion ($sin(\theta) \simeq \theta$) we get:

$$n_i\theta_i = n_t\theta_t \tag{2.3}$$

This is the so called *paraxial approximation*, because corresponds to the condition in which rays are close to the optical axis of the system (paraxial rays). Based on paraxial approximation, one can determine their points of convergence. In principle, these points coincide with the points of convergence of an aberration-free system. The additional terms in the brackets of equation 2.2 represent the deviation from the first-order theory, and quantify the aberrations of the lens. Considering monochromatic light the principal aberrations that an optical system can present are:

- **Spherical aberration** - The spherical aberration is due to the spherical shape of the lens surfaces. For a lens with spherical surfaces, rays which are parallel to the optical axis, but at different distances from it, do not converge to the same point (see fig. 2.1a). Positive spherical aberration means that rays near the edge of the lens have an effective focal point that is closer to the lens than rays that strike the lens near the axis. Negative spherical aberration means that rays near the edge of the lens have an effective focal point that is at a greater distance from the lens than rays that strike the lens near the axis. Since the effective focal length determines the position of the images, several images are formed at different distances. If the light is collected by a camera, the image will be blurred in the presence of spherical aberration because of out of focus rays. Spherical aberration increases with the size of the lens and, in the case of spherical lenses, can be minimized reducing the aperture size; this means using only paraxial rays, so to be closer to the condition of paraxial approximation.
- **Coma** - When parallel rays pass through a lens at an oblique angle θ (see fig. 2.1b) the rays cannot be focused as a point, but as a comet-shaped image. Coma aberration does not depend on the distance of the rays from the optical axis.
- **Astigmatism** - Astigmatism is an aberration of off-axis rays that causes radial and tangential lines in the object plane to focus sharply at different distances in the image space.

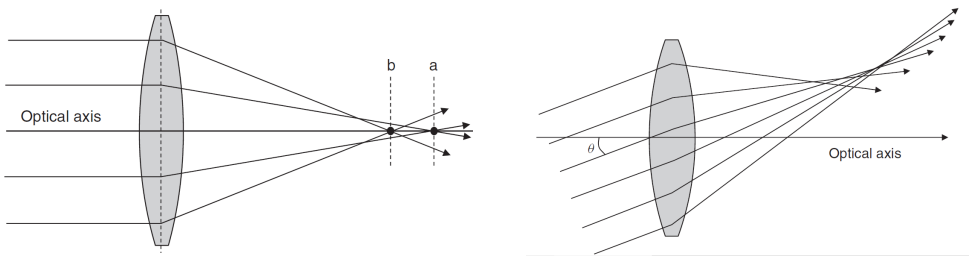

(a) (b)

Figure 2.1: (a) Schematic representation of positive spherical aberration. (b) Schematic representation of coma aberration.

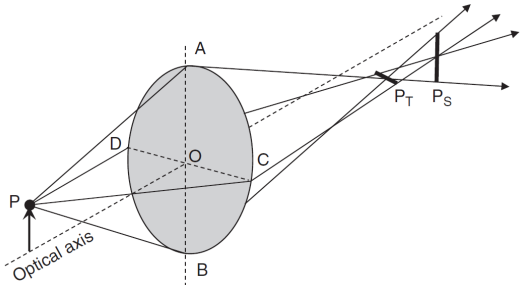

Figure 2.2: Schematic representation of astigmatism. The APB plane is the tangential plane, the CPD plane is the sagittal plane. Rays from these two planes focus on different points, respectively P_T for the tangential plane and P_S for the sagittal plane.

Rays from the tangential plane and from the sagittal plane (see fig. 2.2) focus on different points, creating a blurred image.

- **Field curvature** - Field curvature arises because the image plane is not really a plane but a spherical surface. Figure 2.3a illustrates this effect. When a straight object PQ is placed in front of a lens, the formed image P'Q' is curved. This is because the outer ray has a closer focus than the inner ray, causing the rays through the center of the lens to intersect the rays through the foci as shown. Constructing intermediate points between P and Q and their images subsequently shows curvature. When field curvature is present, close objects seem to have an inward curve, and far away objects seem to have an outward curve. It is possible to correct this effect using a combination of a positive lens and a negative lens that are positioned closely, and this is usually done in camera lenses.
- **Distortion** - This effect is caused by variation in magnification of the image across the field of view. When the magnification of a lens differs at the edge of the lens and at the center, the image of a square object will be abnormally curved. Figure 2.3 illustrates two kinds of distortion. In fig. 2.3b, the lens has too much magnification at its edges, causing a surfeit of magnification of the square at the corners. This is commonly called pincushion distortion, or positive distortion. In fig. 2.3c, the lens has too little power at its edges, causing a barrel, or negative distortion.

However, in most occasions light is not monochromatic.

- **Chromatic aberrations** - The dependence of the refractive index from the wavelength of the light leads to aberrations called "chromatic aberrations". Rays with different wavelengths are refracted differently and consequently converge to different points. Chromatic aberrations are usually corrected using a combination of lenses of different materials.

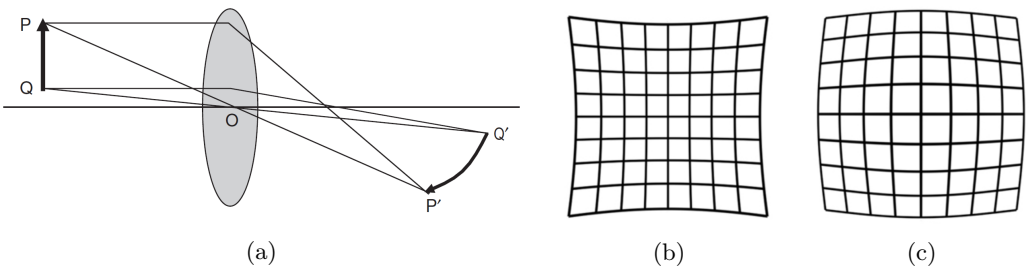

Figure 2.3: (a) Schematic representation of field curvature. (b) Example of pincushion distortion. (c) Example of barrel distortion

2.3 Dynamic aberrations and adaptive optics

If the aberrations are static, they can be corrected with lens combinations once they have been identified, but there are other aberrations that can not be corrected in such a way. For example if the light that we want to collect gets through a medium with a variable (in time and/or space) refractive index, the wavefront that we will receive will be distorted with the consequent formation of a rough image (see fig. 2.4). For instance, this is the case of terrestrial telescopes or microscopes where the light collected by the instrument passes through the Earth's atmosphere or the observed specimen and gets distorted by refractive index variations caused by turbulence in the former or inhomogeneities of the specimen in the latter.

2.3.1 Zernike polynomials

A wavefront can have a generic shape that is not ascribable to neither of the previously described aberrations. In such case, it is useful to describe its shape in rigorous mathematical terms. For this purpose, several mathematical instruments have been developed, including the Zernike polynomials that are the most common instrument used to describe aberrations in optics. The shape of a generic wavefront can be described using a linear combination of these Zernike polynomials. These polynomials are orthogonal on the unit disk and are analytical polar functions. They can be divided in odd and even ones:

$$Z_n^m(\rho,\theta) = R_n^m(\rho)\cos(m\theta), \text{ even polynomials} \tag{2.4}$$

$$Z_n^{-m}(\rho,\theta) = R_n^{-m}(\rho)\sin(m\theta), \text{ odd polynomials} \tag{2.5}$$

where m and n are nonnegative integers with $n \geq m$, θ is the azimuthal angle, ρ is the radial distance $0 \leq \rho \leq 1$, and R_n^m are the radial polynomials defined below. The n index defines the order of the polynomials.

$$R_n^m(\rho) = \sum_{k=0}^{\frac{n-m}{2}} \frac{(-1)^k(n-k)!}{k!(\frac{n+m}{2}-k)!(\frac{n-m}{2}-k)!}\rho^{n-2k} \tag{2.6}$$

Because of their orthogonality and the fact that their derivative are continuous, they efficiently represent common aberrations seen in optics. Moreover, they form a complete set, i.e. that they can represent any arbitrary complex continuous surface given a sufficient number of terms. For these reasons, Zernike polynomials are used in many fields of optics, for example in astronomy for wavefront representation, in optical manufacturing to describe higher-order errors observed in interferometric analyses, in optometry and ophthalmology to describe the aberrations in the human eye. In tab. 2.1 the first order Zernike polynomials are reported. It can be noticed the correspondence between some terms and the aberrations discussed before. In fig. 2.4 the ideal (fig. 2.4b) and real (fig. 2.4d) case of the "point spread function" are shown, i.e. the image of a point source, after the light have double passed the human eye. Also healthy eyes have imperfections which worsen the image on the retina when we observe an object.
To sum up, there are two different problems that adaptive optics (AO) tries to cope with. The first one is the development of a fast and/or compact devices for focusing instead of bulky and slow devices composed by many lenses and the second problem is wavefront correction.
A typical adaptive optics system for wavefront correction has three main components: a deformable element, which consists of a deformable mirror or a deformable lens, a wavefront sensor and a control system. Briefly, the wavefront sensor permits the calculation of the wavefront curvature, this knowledge is used to deform the adaptive element in order to correct the wavefront curvature. If the wavefront sensor is set before the corrective element, the system is in open loop, if it is after the corrective element, the system is in closed loop. The system can also be

n	m	Z_n^m	Classical name	First 21 Zernike polynomials
0	0	1	Piston	
1	1	$2\rho\cos\theta$	Tip (lateral position) (X-Tilt)	
1	-1	$2\rho\sin\theta$	Tilt (lateral position) (Y-Tilt)	
2	0	$\sqrt{3}(2\rho^2-1)$	Defocus (longitudinal position)	
2	-2	$\sqrt{6}\rho^2\sin 2\theta$	Oblique astigmatism	
2	2	$\sqrt{6}\rho^2\cos 2\theta$	Vertical astigmatism	
3	-1	$\sqrt{8}(3\rho^3-2\rho)\sin\theta$	Vertical coma	
3	1	$\sqrt{8}(3\rho^3-2\rho)\cos\theta$	Horizontal coma	
3	-3	$\sqrt{8}\rho^3\sin 3\theta$	Vertical trefoil	
3	3	$\sqrt{8}\rho^3\cos 3\theta$	Oblique trefoil	
4	0	$\sqrt{5}(6\rho^4-6\rho^2+1)$	Primary spherical	
4	2	$\sqrt{10}(4\rho^4-3\rho^2)\cos 2\theta$	Vertical secondary astigmatism	
4	-2	$\sqrt{10}(4\rho^4-3\rho^2)\sin 2\theta$	Oblique secondary astigmatism	
4	4	$\sqrt{10}\rho^4\cos 4\theta$	Vertical quadrafoil	
4	-4	$\sqrt{10}\rho^4\sin 4\theta$	Oblique quadrafoil	

Table 2.1

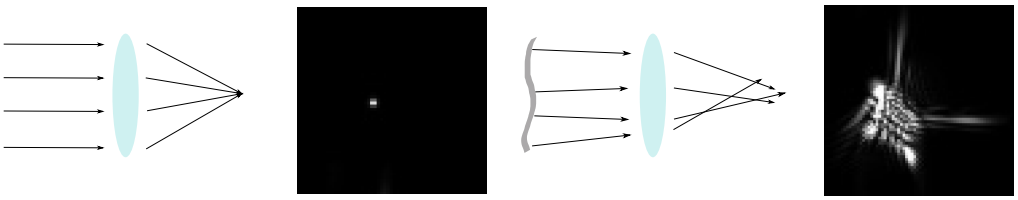

(a) (b) (c) (d)

Figure 2.4: (a) Schematic representation of a flat wavefront focused correctly. (b) Image of a flat wavefront focused correctly. (c) Schematic representation of a distorted wavefront which is not focused in the same point. (d) Image of a distorted focused wavefront.

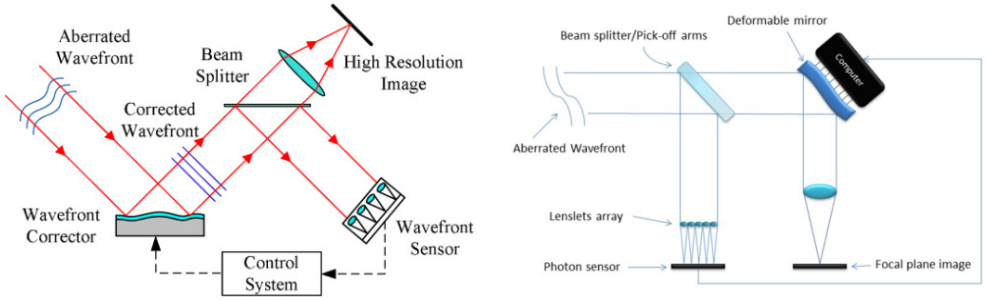

(a) (b)

Figure 2.5: (a) Schematic representation of a closed loop AO system. (b) Schematic representation of an open loop AO system.

sensorless, in such case the correction is made on the basis of a real-time analysis of the acquired images. In fig. 2.5 two schematic examples of a closed and open loop AO systems are shown. The issue of wavefront correction has leaded researchers, in particular astronomers, to the development of a large variety of deformable mirrors and, recently to the development of adaptive lenses capable of correcting (or reproducing) wavefront distortions. The advantage of a lens respect to a deformable mirror is to be less bulky and easier to be inserted in a pre-existing optical system than a mirror, which requires optical setups to relay the pupil plane with folded optical paths.

Recently adaptive lenses have been widely used in fast focusing applications in microscopy or in phone cameras and for wavefront correction in ophthalmology. The demand of deformable lenses is widely increasing. In the next section we will provide a description of different kinds of adaptive lenses, from those make only defocus to those capable of reproducing other aberrations.

2.4 De-focusing adaptive lenses

The human eye has inspired researchers to design several eye-like adaptive lenses capable of varying their focal length. This type of lenses can be divided into two categories: those with a surface profile change and those with a refractive index change.

- **Surface profile change** - In the human eye there is a lens with a bi-convex shape. A muscle encircles the lens in such a way that when it contracts, it can increase the lens curvature, yielding a shortening of the focal length, while when it is relaxed lens curvature decreases. These changes enable the lens to change its focal length. Like the human eye, most adaptive lenses due their variable focal length to a change in the surface profile. There are two different approaches to deform the surface of the lens: the volume of the lens can remain constant or not. In the first case, the volume of the lens is fixed and, varying the aperture of the lens, the curvature is obliged to change in order to maintain the volume. For example, stretchable elastomeric solid lenses, electrowetting lenses, and dielectric liquid lenses are lenses of this kind. Following the second approach, the aperture remains constant, but the volume varies when the surface changes. Conventional elastic membrane lens belongs to this kind of lenses.

- **Refractive index change** - Provided that there is a lens with two flat surfaces and a constant refractive index, a ray which is parallel to the axis would get across the lens without any deviation. But if we find a method to create a gradient distribution to the refractive index, the lens will behave like a converging or diverging lens (depending on the gradient). This is the case of liquid crystals that change their refractive index when an external voltage is applied to them.

In the next paragraphs we will describe these different kinds of adaptive lenses.

2.4.1 Elastomeric membrane lenses

An elastomeric membrane lens is a lens made of a liquid in a chamber with at least one flexible optical surface. When the volume inside the chamber is changed the curvature and so the focal legth of the lens varies without or with little mechanical motions. In several applications, the elastomeric membrane has been made of polydimethylsiloxane (PDMS) [38]. This material is preferred with respect to others for its suitable properties: high optical transparency, large elongation, biocompatibility, highly hydrophobic.
Usually, the lens cell is composed of a lens chamber and a reservoir. PDMS lens cells can be classified into two groups. In the first group, the lens chamber is isolated from the liquid reservoir and the two parts are connected through a tube. In the second group, the lens chamber and the liquid reservoir are integrated together. The center area belongs to the lens chamber, and the reservoir is located in the periphery of the cell. A lens cell with its chamber and reservoir integrated together has a compact structure, and the lens can be easily operated.
As stated before, at least one of the two membranes of the lens is elastomeric. The other boundary surface could be a solid flat substrate, solid convex substrate, solid concave substrate or an other elastomeric membrane.

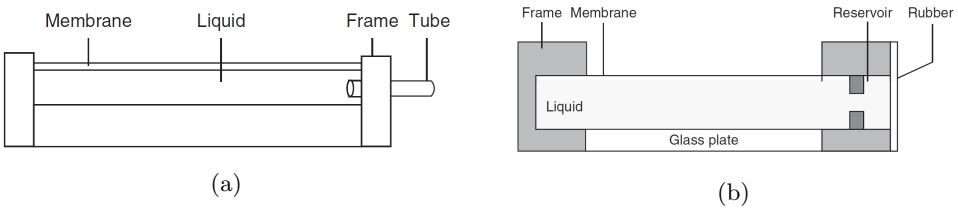

Figure 2.6: Schematic representazion of the two types of elastomeric membrane lenses

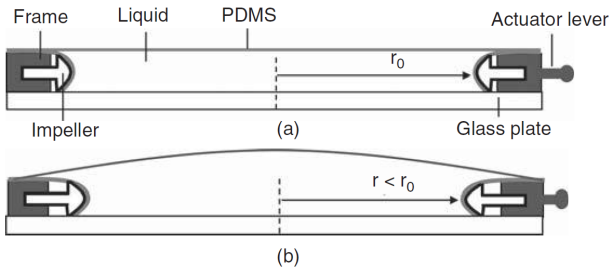

Figure 2.7: Cross-sectional structure of a lens whose surfaces are curved changing the aperture: the circular periphery seal is similar to an iris diaphragm with rotatable impellers so that its radius is tunable.

Several actuation methods have been developed to deform the lens surface(s): a syringe pump [39], motor pumps [40], changing the aperture of the lens [41], piezoelectric linear actuators [42, 43, 44], hydrogels actuators [45], artificial muscles actuators [46]. We report some of the more efficient approaches:

- *Changing aperture* - In [41] it has been proposed an adaptive liquid-filled lens whose actuation is based on varying its aperture. It consists of an elastic membrane, a solid plate and an annular scaling ring; the lens chamber is filled with a fixed volume liquid. The radius of the annular sealing ring is changeable. By tuning the radius of the annular sealing ring, the stored liquid in the lens will be redistributed, thus changing the curvature of the elastic membrane. Both positive and negative foci can be realized by controlling the size of the lens aperture. The negative aspects are that the aperture of the lens is inherently dependent on the lens focal length (it changes from a 14mm to a 25mm diameter) and that the focal length is adjusted using a lever which has to be moved manually or electromechanically.

- *Piezoelectric actuators* - Several adaptive lenses which exploit piezoelectric actuators have been developed.
  In a first prototype [42] two liquids are located in two chambers connected by a circular hole 2.8a. The liquid-liquid interface that is formed at the hole then acts as the aperture of the lens. Because of the different refractive indices of the two liquids, this interface operates as a refractive surface. The lower chamber is equipped with a deformable membrane that is pushed by the piezoelectric actuator to change the liquid volume of the upper chamber. By doing so, the curvature of the interface can be changed dynamically.
  Because the two liquids support each other at the contacting area (aperture), PDMS is not necessary to hold any liquid any more. Without the help of PDMS, the surface profile of two liquids at the aperture area will be much smoother and symmetrical. Moreover, gravity force will not be the main concern to distort the lens surface, so the lens can exhibit high performances.

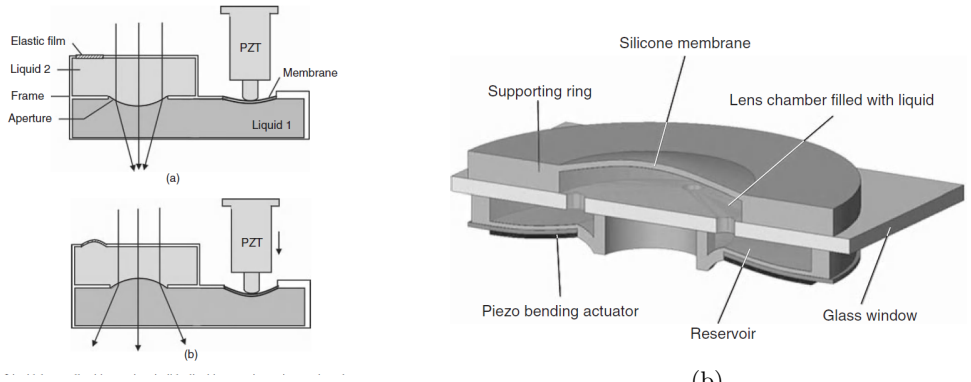

(a) (b)

Figure 2.8: (a) Cross-sectional structure of a liquid lens cell with two immiscible liquids actuated using a piezoelectric actuator [38]. (b) Schematic assembly of a liquid lens with a disk-like piezo-actuator [43].

Since no PDMS is used the lens can be efficiently used in the IR range. Indeed the PDMS transmittance is low for some IR wavelength (due to the resonance of the CH bound). With this prototype the focal length can be varied from -100mm to 150mm. The negative aspect of this device is that it is very bulky and the fabrication procedure is complicated. Another device that exploits piezoelectric actuator is that in figure 2.8b [43]. The chamber of the reservoir and the lens chamber are separated by a glass plate, but they are connected through some small holes in the glass plate. The lens chamber and the reservoir are filled with water or oil. The lens chamber consisting of a silicone membrane and a supporting ring is made of PDMS elastomer. The reservoir chamber is made up of a piezo-bending actuator embedded in silicone. The piezo-actuator is fabricated with a disk-like or zone shape. If a voltage is applied to actuator, the interior edge of the zone-like actuator will bend upwards, so that the liquid in the reservoir is forced to move to the lens chamber. This causes an increasing bulge in the lens membrane; as a result, the focal length of the lens is decreased. This device results to be compact, simple, and low cost. The achieved focal length ranges from 30 to 500 mm at a voltage from -9 to 44V. The lens resolution is crucially dependent on the thickness of the lens membrane. The diameter of the lens is about 5mm while the lens dimensions are higher to permit the realization of the actuation system.

- *Muscle-like actuator* - A fluid-filled elastomeric lens is integrated with an annular elastomeric actuator that works as an artificial muscle [46]. Electrical activation of the artificial muscle deforms the lens, with a relative variation of focal length comparable to that of the human lens. The actuator is composed of a dielectric elastomer (ER). Thin layers of such materials coated with compliant electrodes can be electrostatically deformed upon electrical charging. The lens and the annular actuator form a single body, consisting of two membranes of an optically transparent dielectric elastomer that are bi-axially pre-stretched, coupled together and fixed to a circular plastic frame. To obtain a symmetrical biconvex lens, a transparent fluid is confined in a central region of the membranes, creating a closed chamber. The remaining part of the membranes, corresponding to an annular planar region, is coated with a compliant-electrode material so as to obtain an annular DE actuator. Upon electrical activation or deactivation, the actuator radially relaxes or stretches the lens so as to change its radius of curvature and thus its focal length, miming exactly the same functional operation of the natural system (see fig. 2.9).

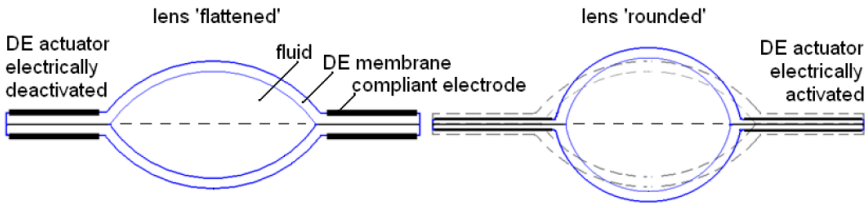

Figure 2.9: Schematic representation of the actuation system of a lens with an dielectric elastomer that acts like a human eye muscle [46].

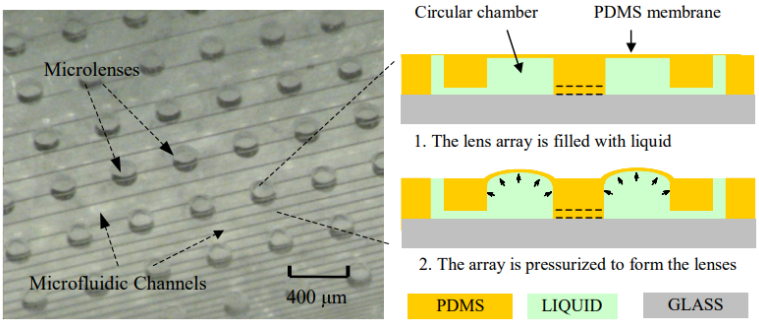

Figure 2.10: Optical micrograph of the microlens array. Upon pressurizing the elastomeric liquid filled chamber, the membrane deforms forming a plano-convex lens array [47].

- *Tunable microlenses arrays* - Besides a singlet liquid lens, PDMS has also been widely used to fabricate variable focal length microlenses arrays. PDMS-based microlens arrays have been studied extensively in recent years. They have potential applications in information processing, photonic imaging, tunable photonic wave guides, biomedical instruments, lab-on-a-chip systems, telecommunication, optical data storage, and variable optical attenuators. The operation mechanism of each microlens in its array is similar to that of a single macro-sized liquid lens, but their fabrication is quite harder.
  An example is the device tests in [47]. They report an integrated tunable liquid-filled microlens array on a microfluidic network to simultaneously control the focal length of multiple microlenses. The focal length of each lens is dynamically adjusted by pneumatically controlling the pressure within a microfluidic network.

2.4.2 Electrowetting lenses

When a small amount of liquid is dripped on a solid substrate surface, various shapes can be obtained. The shape of a liquid is dependent on the relative strengths of the cohesive force and the adhesive force acting on the liquid; that is, they determine the droplet whether or not it will wet the surface. If the adhesive forces between a liquid and a surface are stronger, they will pull the liquid down, causing it to wet the surface. However, if the cohesive forces among the liquid itself are stronger, they will resist such adhesion and keep the liquid to retain a spherical shape. The angle formed by the solid surface and the tangent line to the upper surface at the end point is called the contact angle and depends on the solid-liquid, solid-vapour, and liquid-vapour interfacial tensions. If the interfacial tension of the liquid/solid is variable, the contact angle and hence the surface profile of the droplet could be changed accordingly. In the early 1990s, Berge proposed to use a thin dielectric film to separate the electrolyte liquid from the metal electrode

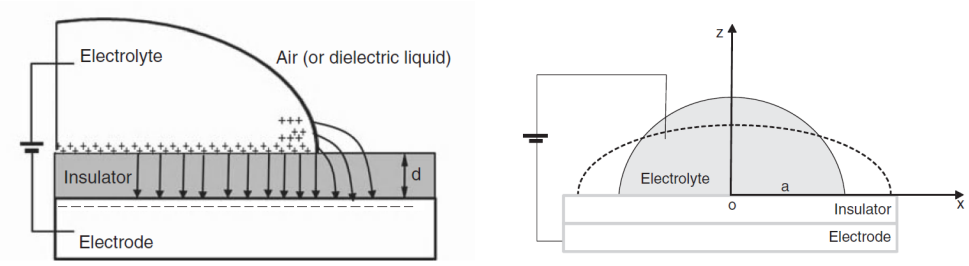

(a) (b)

Figure 2.11: (a)Schematic representation of how the electrowetting phenomenon is used in adaptive lenses. (b)Surface profiles of a droplet with voltage-off (solid curve) and voltage-on (dashed curve) states.

[48]. This concept has subsequently become known as electrowetting on dielectric (EWOD).
Consider now a system as that in fig. 2.11. It consists of an electrode, a dielectric layer and a conductive liquid droplet. A coating layer on the insulator can provide a low surface tension so that the droplet can exhibit a large contact angle. When a voltage is applied between the electrolyte solution and the electrode, positive charges accumulate on the top surface of the insulator and negative charges accumulate on the bottom surface of the insulator (see fig. 2.11a). The generated electrostatic force can cause the contact angle to decrease. The altered contact angle will subsequently change the surface profile of the droplet (dashed curve in fig. 2.11b). Starting from the equilibrium of the interfacial tensions is possible to derive that the cosine of the contact angle is proportional to the square of the applied voltage across the solid-liquid interface and that the droplet surface is a parabola [38]. If the cell is placed in vertical direction, then the gravity force will take effect to drag the droplet downward. While in the cases of shaking or vibrating, the droplet will not firmly adhere to the substrate surface. To solve this problem, another liquid is preferred to fill the outside space of the droplet for balancing out the gravity effect. Moreover, the filled liquid can serve several purposes. One is to prevent the droplet from evaporating; the second is to lubricate the contacting surface, so that the contact angle hysteresis could be depressed. The third is to adjust the initial focal length of the droplet by selecting the confinement liquid with an appropriate refractive index.
We now describe four adaptive lenses that exploit the electrowetting phenomenon and has found their way in commercial applications.

- Figure 2.12a shows the device structure of a singlet lens [49] based on electrowetting. It consists of a glass substrate (1), an electrode (2), a dielectric layer (3), a surface coating (4) and a conductive liquid droplet (5). The electrode is made of ITO (indio-tin-oxide) a conductive material which is transparent to light (obviously its transmittance is a function of the wavelength). The dielectric layer prevents the conductive droplet contacting from the electrode. Fluoropolymer deposited on the dielectric layer is used as the coating layer. Such a material can provide a low surface tension so that the droplet can exhibit a large contact angle. When a voltage is applied between the droplet and the electrode, the conductive droplet expands on the bottom substrate surface as shown in 2.12a. This is due to the opposite charges accumulating on both surfaces of the dielectric layer, similar to the structure shown in fig. 2.11a. The pattern of the indium-tin-oxide (ITO) electrode is shown in fig. 2.12a. The electrode is divided in 5 parts in such a way that by applying an identical voltage to all the control electrodes the contact angle and the curvature of the droplet can be uniformly altered, while applying different voltages it is possible to move the droplet in the direction of the part with a higher potential. This kind of device would

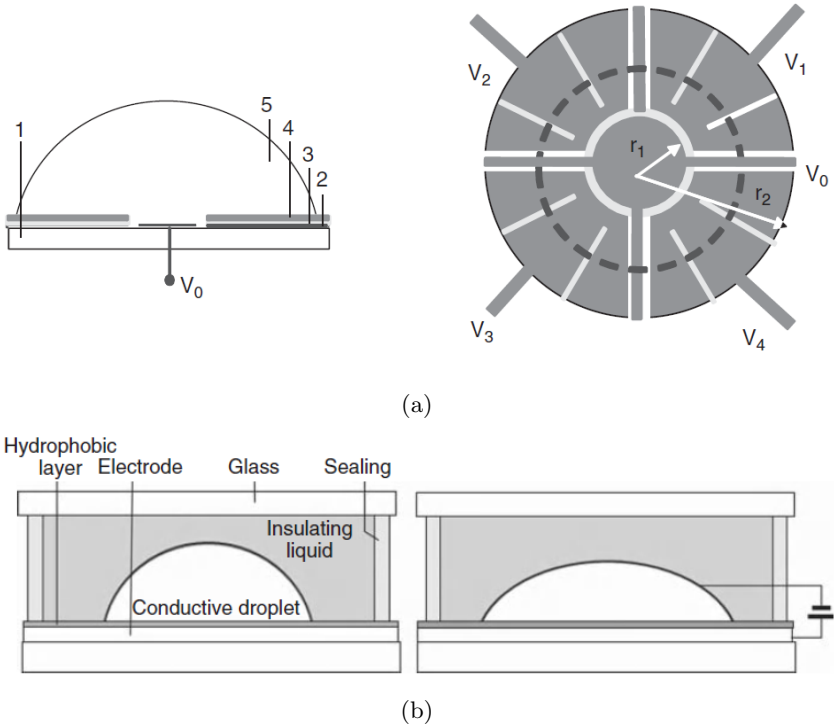

Figure 2.12: (a) Schematic representation of the tunable electrowetting lens [49]. On the left a cross-sectional view. Voltage applied to the ground electrode is indicated as V_0. On the right: electrode pattern. The white lines indicate etched areas on ITO. Applied voltages are indicated as V_0 through V_4. The dashed circle represents an approximate droplet position. (b) Cross-sectional view of a lens, exploiting the electrowetting phenomenon, in the relaxed (left) and active state (right).

not serve in vertical position because gravity would force the droplet downwards. So a second liquid which surrounds the droplet is needed to prevent the droplet to move away from its position or thrill under vibrations. Such a device could be like that shown in fig 2.12b.

- In 2004, at the Philps Reasearch, a model of electrowetting lens which has then largely been used in phone cameras has been developed [50]. The lens cell is composed of a cylindrical chamber hosting dielectric oil and conductive water. For practical applications indeed, the conductive droplet must be firmly fixed on the electrode and not thrill with vibrations or movements of the device. The conductive water is in direct contact with the bottom electrode. The inner surface of the cylindrical chamber is coated with a dielectric layer. Outside the dielectric layer is an electrode. The height of the electrode is large enough to involve the meniscus between the two liquids, but shorter than the whole height of the cylinder. The inner pillared electrode can extend to outside and connects to the electrode coating on the outside lateral surface. When no voltage is applied, the water surface is concave, and the lens is divergent. by applying an opportune voltage, the surface can be made flat. With a higher voltage the contact surface becomes convex and the lens convergent. The diameter of the lens is 3 mm and the whole device is small enough to be used as phone camera. The focal length can be varied from -10 mm to 20 mm.

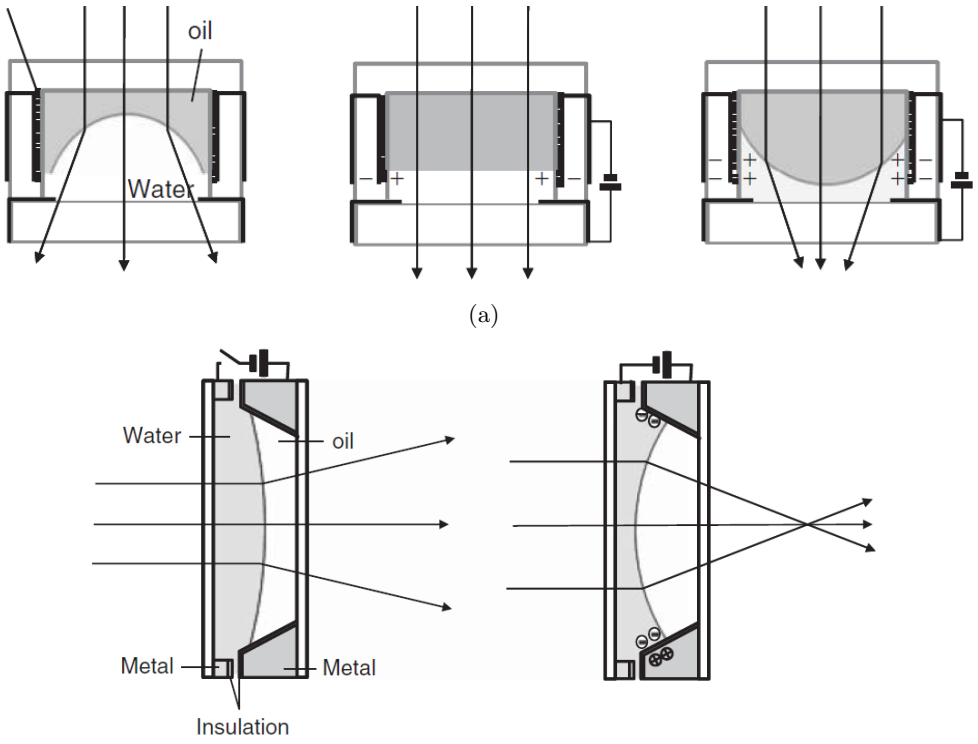

Figure 2.13: (a) Cross-sectional view of the electrowetting lens developed at the Philip Reasearch [50]. the lens is shown in the divergence (left), flat (middle) and convergent (right) conditions. (b) Cross-sectional view of the electrowetting lens developed by Berge and collegues [51]. The lens is shown in the divergence (left), and convergent (right) conditions.

- A similar device but with a lower heigth has been developed by Berge and collegues in 2010 [51]. It consists of a glass substrate, conductive water, insulating oil, and a glass window (see fig. 2.13b). The circular metal electrode on the periphery of the left glass substrate is in direct contact with the water. The circular electrode on the periphery of the right substrate is coated with an insulation layer. The inner surface of the electrode is tilted and an as well tilted insulation surface makes contact with the two liquids. When no voltage is applied the contact surface in convex and the lens divergent. Applying a sufficient voltage the surface can be made concave and the lens convergent. This lens can change the focal length from 60mm to infinite and its diameter can be varied from 6 to 10 mm.

2.4.3 Dielectrophoretic lenses

Dielectrophoresis (DEP) is a phenomenon that occurs when a neutral particle is placed in an electric field that is spatially non-homogeneous causing a force that is proportional to the gradient of the electric field. Numerous works have been done and various microfluidic devices have been developed based on the operation mechanism of DEP effect. An interesting application of the DEP force is to reconfigure the shape of a dielectric liquid droplet.
Considering the device in fig. 2.14 from top to bottom, it is composed by a planar glass plate, indium-tin-oxide (ITO) electrode, surrounded liquid (1), droplet liquid (2), a dielectric layer,

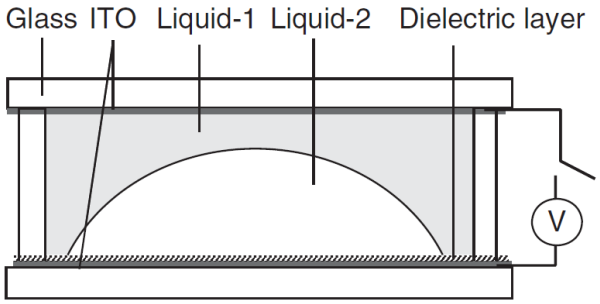

Figure 2.14: Side-view structure of a dielectrophoretic lens cell [38].

an ITO electrode, and a planar glass plate. The two liquids are immiscible but with different dielectric constants. In the relaxed state, the droplet exhibits a spherical shape with the lowest surface energy. Because of the cohesive force, molecules in the droplet are bonded together without separation. When a voltage is applied, a inhomogeneous electric field creates in the chamber because of the different dielectric constants of the two liquids and the droplet has to reshape to balance the generated dielectric force. The drop will expand or shrink depending on the dielectric constants of the two liquids.
The shape-deformable droplet actuated by DEP force could function as an adaptive lens as well. This has potential application in various fields as in imaging processing, optical beam steering, cell phone cameras, optical modulators, optical fiber switches, amplifiers, machine vision, and lab-on-a-chip.
Dielectrophoretic lenses are very stable, can bear a high operating voltage and their power consumption is low because of little heat generation. These devices has been realized in different way: with a the hole-patterned electrode technique [52], with concave electrodes [53] and with striped-patterned electrodes [54].
Dielecrtophoresis has become a strong competitor with electrowetting: they are much more attractive for practical applications due to low power consumption, high voltage bearing, less evaporation, and good stability. Although dielectrophoresis using is still at its beginning, it will surely be improved further.

2.4.4 Other types adaptive lenses

2.4.4.1 Acoustic liquid lenses

When an ultrasound beam is used to irradiate the interface of two immiscible liquids that have different densities, an acoustic irradiation force is generated at their interface. Such a force can reshape the surface profile of the two liquids. Therefore, a lens with a tunable focus can be obtained. Adaptive liquid lenses actuated by acoustic radiation force have been reported by several groups [55, 56]. Due to the simple construction, compact structure, and tunability, this kind of lenses are useful for optical manipulation, optical trapping, and imaging particle manipulation.
As represented in fig. 2.15b, two immiscible liquids (water and silicon oil) are filled in a cylindrical chamber. The bottom terminal is sealed with an acoustic transducer. The transducer has a concave surface, so that it can enhance the acoustic radiation force at the focal point. The top terminal is covered with a glass plate. Because water and silicon have different densities (sound speed is different) and refractive indices, they are suitable materials for making such an acoustic lens. Due to the surface tension force, the water and silicon oil have a curved interface [56].

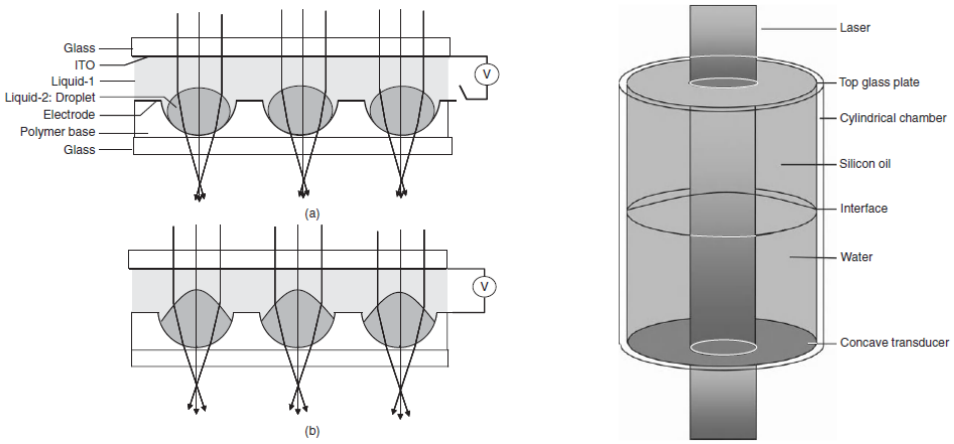

(a) (b)

Figure 2.15: (a) Cross-sectional view of a dielectrophoretic array with concave electrodes [38]. (b) Lens driven with ultrasound modulation of the contact surface of two immiscible liquids (water and silicon oil) [38].

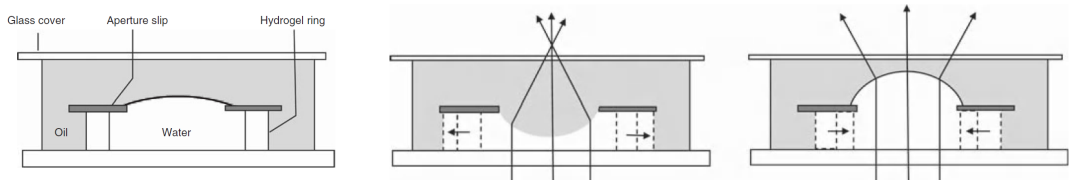

(a) (b)

Figure 2.16: (a) Side view on a hydrogel lens. The interface between two immiscible optical liquids (water and oil) with different refractive indices forms an optical surface. The water is confined between the glass plate, the oil, and the hydrogel ring. The ring contracts when subjected to an external stimuli (temperature, pH, etc.) with the consequent change of the water-oil meniscus curvature. (b) Contracting state (left), expanding state (right).

2.4.4.2 Hydrogel lens

An adaptive lens that allows autonomous focusing has been demonstrated using stimuli-responsive hydrogel intagrated into a microfluidic system and serving as container for a liquid droplet [45]. The expansion and contraction of hydrogel regulates the shape of a water-oil meniscus that serves as refractive surface of a lens (see fig. 2.16). The device can have a focal length from $-\infty$ to ∞ and may find applications as sensing, medical diagnostics and lab-on-chip technologies. Indeed has been demonstrated that various types of hydrogel can respond to different stimuli: pH, temperature, light, electric field and antigens.

2.4.5 Liquid crystal lenses

Liquid crystals (LCs) are substances that possess the properties of ordinary liquids together with some of crystalline solids. They may flow like a liquid while having molecules arranged or ordered in a crystal-like way. Three phase states which depends on the temperature can be defined: crystalline solid, liquid crystal or nematic, and isotropic liquid. A nematic LC has a permanent dipole or it is easy to polarize with an external electric field. In such situation

the molecules will align along the direction of the external electric field. In the absence of an external electric field, LC exists in the state of micro-domains. In each domain, LC presents ordered orientation, but for different domains their orientations are different. It is possible to align the molecules in one preferred direction with an electric field, as stated before, or sandwiching the LC between two substrates whose inner surfaces are treated with surface alignment layers. Polymide (PI) is an example of material used for the alignment layers. The average direction of the molecules defines what is called "director". LC presents two different refractive index and dielectric constants along the two axis defined by the director and the perpendicular plane. This anisotropy of LCs has been exploited to develop many optical devices including displays, adaptive focus, beam steering, spatial light modulators, variable optical attenuators, axial or radial polarization rotation, and other photonics devices. The discussion of all LC applications is not of our purpose, but we will describe briefly how they have been exploited for the development of adaptive lenses.
The main idea is to use LC crystals as phase modulators. Let's consider a cylinder of liquid crystals and suppose it is possible to vary the orientation of the molecules radially: the refractive index will change accordingly with the orientation of molecules. With some calculations [38], it's easy to see that the LC cylinder behaves as a grin lens (divergent or convergent, it depends on how the refractive index varies).
Several methods have been used to create this variation of refractive index along the lens (hence creating a non uniform electric field): curved electrodes of different shapes, Fresnel lenses, stripped electrodes, hole-patterned electrodes and polymer-LC composite lenses. Some examples are described in fig. 2.17.

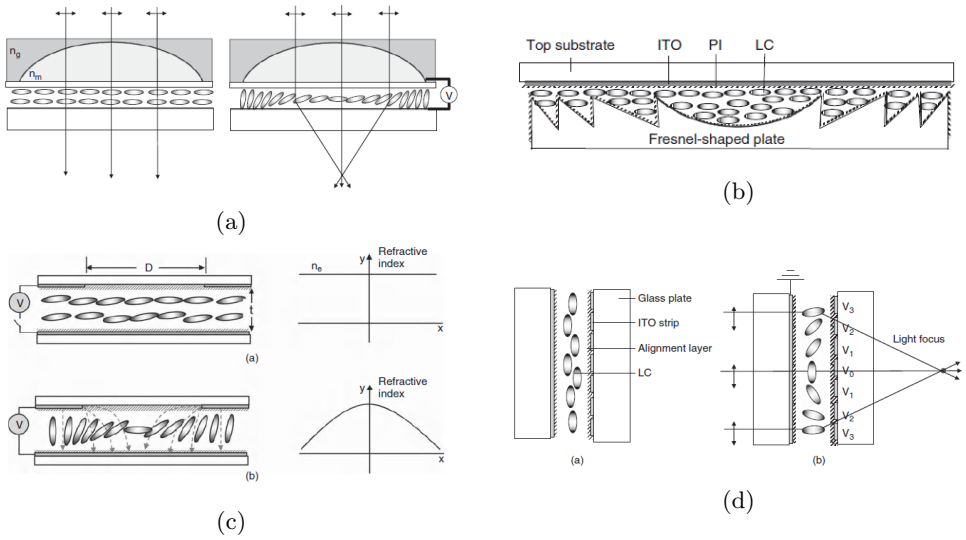

Figure 2.17: Some LC adaptive lenses approaches. (a) An LC lens with flat substrates and a curved electrode that creates a non uniform electric field in the LC cell. On the left: not focusing state at V = 0. On the right: focusing state by applying a voltage to the electrodes. (b) Cross-sectional structure of an LC-based Fresnel lens. The Fresnel lens is made by carving a conventional spherical lens into a set of concentric annular sections. The grooves act as individual refracting surfaces, like tiny prisms when viewed in cross section, bending parallel rays in a very close approximation to a common focal length. (c) LC orientation in the lens cell and the refractive index distribution in the hole area. Above: voltage-off state. Below: voltage-on state. (d) A tunable-focus lens with striped electrodes and a homogeneous LC layer. The inhomogeneous electric field is created with many electrodes at different voltage values.

2.4.6 Pros and cons of defocus lenses

In the previous sections, some adaptive defocus lenses based on different principles have been described. Some of them have found important applications in industries and research. Obviously, this chapter is not a complete review of the adaptive lenses that have been developed until now. For a more complete explaination in details about adaptive lenses it is possible to consult [38]. Here, we try to summarize what has been discussed before, pointing out the pros and cons of the adaptive lenses discussed.
One of the issues of PDMS membrane lenses is the influence of gravity on the shape of the lens surface. Due to the gravity effect, when the lens cell is placed in vertical direction, the larger the lens aperture, the worse the distortion of the lens shape. For lenses with two liquids but without a PDMS membrane gravity effect is conquered matching their densities. However, in such cases the lens structure is bulky and the fabrication complicated. Also solid lenses made of PDMS have been proposed, but their dynamic range of action is limited and they suffer of high aberrations problems. Most of adaptive lenses with an elastomeric membrane are still actuated with a mechanical system.
Electrowetting has also been exploited for adaptive lenses development. It represent a valid alternative to the elastomeric membrane lenses, indeed by using two density-matched liquids, the gravity effect of the liquids can be balanced. However, the dielectric thickness plays an essential role in the success of the device. If the dielectric layer is too thick the needed voltage for the actuation is too high, while if it is too thin there can be the break down of the dielectric layer. Also oil or dielectric charging can occur and compromise the device performances. Electrowetting lenses have been successfully used in many commercial devices as phone cameras. Their limit is the lens aperture which is always in the millimeter range.
In comparison to electrowetting lenses, dielectrophoretic liquid lenses are much more attractive for practical applications due to low power consumption, less evaporation, and good stability. They do not present problems of liquid charging and higher voltage bearing. Besides imaging, dielectrophoretic droplet lenses have potential applications for light shutters, beam diffusers, adaptive iris, and displays. The development of this kind of lenses is currently at the beginning and will be surely improved further.
For the acoustic liquid lens, the lens structure is compact and the dynamic tuning speed is very fast (2.18 MHz [55]). However, it is difficult to achieve a lens with high performance. Moreover, the lens aperture is confined by the acoustic (piezoelectric) transducer.
For the lens based on stimuli-response hydrogel, several different stimuli can cause the cylindrical hydrogel chamber to expand or shrink. The drawbacks of the stimuli hydrogel lens are the complicated fabrication process and slow response time.
Liquid crystals represents a good alternative to all this methods for the realization of adaptive lenses. Therefore, their usage is limited to low power laser application because they are polarization sensitive and monochromatic.

2.5 Lenses correcting higher order aberrations

2.5.1 Elastomeric lens with tunable astigmatism

In [57] it has been shown that the application of an azimuthally varying strain to a deformable elastomer lens can result in controlled variation of aberrations, particularly astigmatism. An equiconvex lens with identical radii of curvature was fabricated using PDMS with eight mechanical anchors embedded in opposing pairs at the periphery of the lens. Application of outwardly directed forces along one direction results in strain deformations of the lens. Since the volume is conserved, the radius of curvature of the lens decreases and the focal length increases (for rays in the plane defined by the direction of stretching and the axis of the lens). Stretching the lens

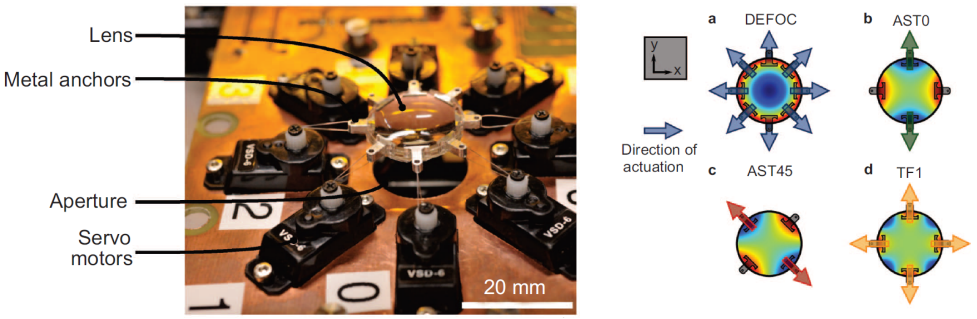

(a) (b)

Figure 2.18: (a) Photograph of the elastomeric lens including the actuators [57]. (b) Representation of selected wavefront errors as Zernike polynomials [57]. The arrows represent vectored actuation in different directions: (a) all axes, leading to defocus (DEFOC), (b) along y-axis, leading to negative astigmatism (AST0), (c) along the axis at 135°, leading to negative astigmatism (AST45), (d) joint actuation of x- and y-axis.

along only one axis correspond to create an astigmatism aberration. For example, deforming the lens along its x-axis results in an increasing astigmatism (corresponding to the aberration of the Zernike polynomial Z_2^2 that we will call AST0), while straining the lens parallel to its y-axis causes the same coefficient to decrease (see fig. 2.18b). If two orthogonal axes are actuated simultaneously, the effect of one axis on the AST0 polynomial is canceled out by the other. Straining the lens on both orthogonal axes simultaneously will therefore result in a negligible change in astigmatism for x-y direction. Stretching the lens along the orthogonal axes at 45° and 135° results in astigmatism relative to Z_2^{-2} (that we will call AST45). The AST0 astigmatism can be tuned independently from AST45 astigmatism. Applying the same force along all the four axis, it is possible to change the focal length of the lens of about the 7% with an initial focal length of about 32mm.
Overall wavefront aberrations of the unactuated elastomeric lens are comparable to those of the commercial singlet glass lens and the lens does not suffer of gravitational sagging.

2.5.2 Free shape lens with piezoelectric actuators

The number of adaptive optics applications could be significantly increased developing a lens capable of correcting high order aberrations. In [58] it has been presented a Multi-actuator Adaptive Lens (M-AL) that can correct aberrations up to the 4th order of the Zernike polynomials. The lens is composed by two thin glasses on which two rings of piezoelectric actuators are mounted. The space between the glasses is filled with a transparent mineral oil. Each of the two rings is composed by 9 actuators for a total of 18 actuators that act as bimorph piezoelectric actuators. The actuators attached to the bottom and top glass generate different deformations because those attached to the top glass are free to move, while those attached to the bottom ones are fixed at their border by an aluminium ring (see fig 2.19b). This has the effect of placing the maximum deformation of the glass surface inside the aperture. The shape of the top window is restrained in the center by gluing a transparent disc of borosilicate glass with the same refractive index as the liquid. In this way the bottom window is used to generate defocus and astigmatism while the top one generates coma and secondary astigmatism. The M-AL has been employed in a high resolution Optical Coherence Tomography (OCT) system to acquire in vivo mouse retina images, correcting aberrations with a wavefront-sensorless algorithm controlling the M-AL. Wavefront sensing in the mouse eye is challenging due to multiple reflections arising from differ-

ent retinal layers. In fig. 2.20 can be seen the remarkable improvement with the correction of the adaptive lens in comparison to the image captured without the correction. Also a comparison of the point spread functions profiles and an interferogram of the wavefront are reported. The M-AL has many potential applications thanks to its easiness to use and its remarkable results. Lenses of different dimensions can be built in order to satisfy different requirements for other systems.

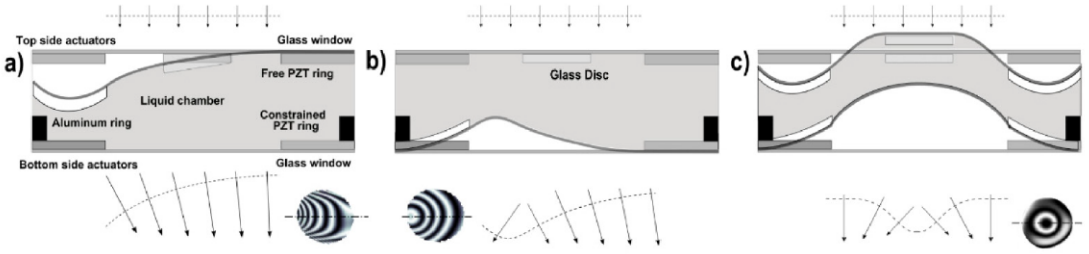

Figure 2.19: Measured wavefront deformations (arrows) and the interferograms relative to the actuation of the M-AL in three different configurations: a) one electrode on the top window, b) one electrode on the bottom window, c) all the actuators poked with the same voltage value. [58]

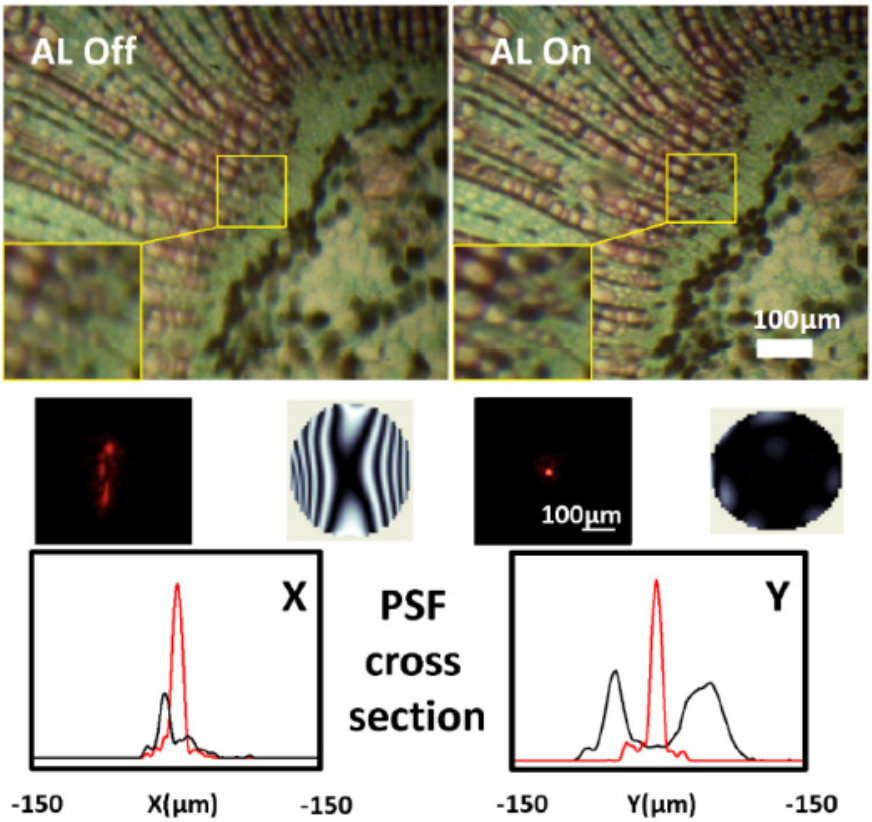

Figure 2.20: Top panel: image before and after closed loop corrections. The yellow insets show the central part magnified of two times. Bottom panel: Point Spread Function (PSF), PSF X and Y cross section before (black) and after (red) the correction and wavefront represented as an interferogram.[58]

2.6 Adaptive lenses actuated by SMAs

2.6.1 Variable focus lens with winding-type SMA actuator

In reference [59] a lens with variable focal length employing an actuator composed by two antagonistic wires has been proposed. The lens is composed by a PDMS lens encircled by eight load arms that join an outer ring that is rotated by SMA wires winding the ring. The PDMS lens is insensitive to gravity and external vibrations and can be realized into a bi-convex or aspheric geometry. The load arms are designed to encircle the PDMS lens, similar to the zonular fibers encircling the crystalline lens in the human eye, and connect the PDMS lens with the outer ring by grippers that hold the protruding parts of the PDMS lens. To distribute the force generated by the winding-type SMA actuator to the load arms equally, the outer ring is placed between the winding-type SMA actuator and the eight load arms. Similar to the mechanism of the human eye, in which the elastic crystalline lens is contracted or expanded by the ciliary muscles and zonular fibers, the PDMS lens is contracted or expanded by the muscle-like SMA actuator. The presence of two antagonistic wires ensures the capability of controlling the displacement in both the directions. When one wire is heated up. the outer ring rotates and the load arms pull the PDMS lens that expands with a consequent change of curvature and, thereby, of the focal length. Heating the other wire leads to a restoring of the initial focal length. Thin copper pipes are placed between the SMA wires and the outer ring to isolate the outer ring from the high temperature when the SMA wires are heated up. Finally, a friction pad is placed between the upper part and the outer ring to maintain the current focal length after turning off the power of the SMA actuator. Since there is a single actuator, there are not asynchronous movements of the load arms that can cause undesired errors.
This kind of lens has an initial aperture of 18 mm and an initial focal length of 16.8 mm that can be adjusted to 18.0 mm.

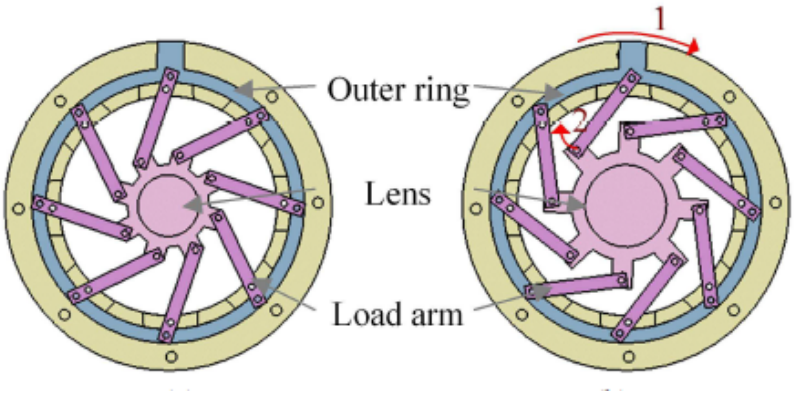

Figure 2.21: Schematic representation of the variable focus lens with winding-type SMA actuator [59]. On the left it is represented the condition with no current applied, on the right current is on and one SMA wire has undergone a displacement in the direction of the red arrow. As consequence, the load arms are stretching the PDMS lens.

2.6.2 Variable focus lens using SMA springs

The authors of [60] developed a lens with tunable focal length and a large aperture. It consists in a liquid filled chamber bounded with a compressible circular rim. The back surface is rigid, made of acrylic, while the other is an elastic membrane made of PDMS. The lens rim has three circular notches, placed 120 degrees apart, into which three SMA spring are placed. A rigid washer maintains the elastic membrane in place. When the SMA springs are electrically actuated,

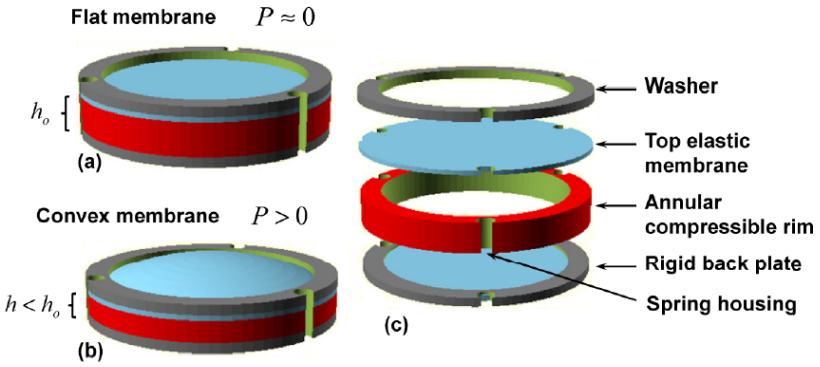

Figure 2.22: Schematic representation of the tunable-focus lens with SMA spring actuators [60]. The lens consists of a top elastic membrane that produces the lens curved surface, a rigid bottom plate and a compressible notched annular rim of height h_0 . The interior of the lens cavity is filled with an optical fluid and the cavity is compressed at the rim with three vertical SMA spring actuators spaced 120 degrees apart. (a) Lens in planar state, (b) Lens in convex state with compressed rim height $h < h_0$ when SMA springs are heated with electrical current, (c) open view showing the lens components excluding the spring actuators.

they shorten and consequently compress the elastic rim and the height of the fluid chamber decreases. Since the liquid trapped inside the lens chamber cannot leak outside, to maintain the total volume of the liquid constant, the flexible membrane bulges outward (thus producing a positive power). The lens is capable of changing its optical power between 0 and 4 diopters with a low applied voltage of about 3V and the response time of the lens was approximately 4 seconds.

2.7 Final remarks

The need of easily embeddable adaptive optical devices is recently increasing. To satisfy the demand, several adaptive lenses models have been proposed and some of them found remarkable commercial application and allowed very good results in the research field. The recent development of free shape lenses capable of correcting high order aberration has open the way for the wider usage of adaptive optics in ophthalmology, microscopy, astronomy, free space communication and medium power laser focusing. New kinds of more performing adaptive lenses will be and are expected to be developed.
Shape memory alloys have been exploited for adaptive lenses designing with promising results. Several and great improvements have be done respect to the current existing devices in order to achieve performances with perspectives in the research or commercial fields.
In the next tables we have summarized the main properties of some lenses discussed before when available.

	Elastomeric membrane lenses				
Actuation approach	Changing aperture [41]	Piezoelectric actuator [42] (fig. 2.8a)	Piezoelectric actuator [43] (fig. 2.8b)	Muscle-like actuator [61]	PDMS microlenses arrays [47]
Lens power variation (1/m)	9	17	31	23	333
Lens aperture (mm)	14/25	4	5	7.6	0.2
Operation frequency (Hz)	–	0.05	–	1−10	–
RMS wavefront error	–	–	$\lambda/2$	–	–

	Electrowetting lenses			Dielectrophoretic lenses	
Actuation approach	Drop on ITO electrode [49]	Philips [50]	Berge [51]	Concave electrodes [53]	Striped pattern electrodes [54]
Lens power variation (1/m)	45	100	17	445	227
Lens aperture (mm)	3	3	6/10	0.72	0.5
Operation frequency (Hz)	200	–	30	55	10
RMS wavefront error	–	–	$< 0.12\mu m$	–	–

	Other types of lenses			Lenses actuated by SMAs	
Actuation approach	Acoustic lens [55]	Hydrogel lens [45]	Free shape lens [58]	Biomimetic lens [59]	SMA springs [60]
Lens power variation (1/m)	2.4	40	1.4	4	4
Lens aperture (mm) 2.5	–	1-4	10	8	34
Operation frequency (Hz)	kHz	–	200	2	0.25
RMS wavefront error	–	–	0.042λ	–	0.77 μm to 1.68 μm

Table 2.2

Chapter 3

Modeling SMAs behaviours

When a smart material is employed in an actuation system, it is necessary to correlate in a univocal way the control signal and the response of the device or to develop a control system that takes into account the eventual hysteresis of a material. The increasing use of SMAs in actuation systems have made necessary the development of a theoretical model to describe and control their behaviour. The models that have been proposed from the 1980, when this kind of research started, until now, can be divided into three categories:

- **Microscale models**
  Microscale models focus on nucleation, interface motion, twin growth and other aspects from a microscopical point of view. These models are useful for a comprehension of what occurs at a microscopical level when shape memory alloys exploit a phase transformation but are not useful to simulate microscopical behaviours of SMA devices.

- **Micro-macroscale models**
  Micro-macro studies combine micromechanics and macroscopic continuum mechanics to derive constitutive laws of the material. Their predictions are often successful, but the required time-consuming computations make them inappropriate for engineering applications.

- **Phenomenological or Macroscale models**
  Phenomenological models use macroscopic variables to describe the material behaviour. This approach is suitable for engineering applications, it can be used to carry on numerical simulations (such as Finite Element Method - FEM) to predict the materials behaviour from a macroscopical point of view, that is of main importance in devices applications.

Since phenomenological models are more suitable for a simulation of devices that exploit SMAs, we have chosen one of these to carry on our simulations. Before describing this model, we will briefly present the main phenomenological models that have been proposed until now.

- **Phenomenological models without internal variables**
  These models use strain, stress, temperature and/or entropy to describe the material behaviour but no internal variables as quantities representing the phase percentages in the material. They can be divided into two groups:

  - **Polynomial potential models**
    In this approaches the behaviour of the material is based on a description of the free-energy in the form of a polynomial. The derivatives of this polynomial represent the constitutive equations for the variables of the model. In 1980, Falk proposed a

Landau-Devonshire like free-energy function based on the analogy between SMA uniaxial stress- strain curves and the electric field-magnetization curves of ferromagnetic materials [62, 63]. These models have the advantage to be very simply, but do not provide an accurate description of the processes involved in phase transformations for SMAs.

- **Hysteresis models**
  Hysteresis models aim to reproduce experimentally observed curves that involve high non linearity and complex looping as SMAs do. They have been widely used in several fields, in particular for magnetic materials. In this approach, constitutive equations are proposed directly on the basis of their mathematical properties, often without explicit focus on their link with the underlying physical phenomena of interest. These methods present a good match with experimental results and the use of a suitable algorithm allows the control of SMAs behaviour with a driving input. Two main algorithm classes can be identified. The first one is based on tracking sub-domain conversion/reversion and lead to integral based algorithms. The most common of these is known as the Preisach algorithm and it has been used to describe successfully the behaviour of different kinds of smart material that present hysteresis (magnetostrictive and piezoelectric materials, shape memory alloys) [64, 65, 66]. The second class of algorithms involves differential equations with separate forms for driving input increase and decrease. Differential equations of Duhem-Madelung form have been used to model SMA phase fraction evolution during thermally induced transformation [67].

- **Phenomenological models with internal variables**
  In this approach two types of variables are involved: mechanical and thermal *control variables*, and *internal variables*. Mechanical control variables can be either stress or strain, thermal control variables can be either temperature or entropy. Internal variables include one or more phase fractions. These models consider as an internal variable the volumetric fraction of martensite present in the material, which is expressed as a function of temperature and stress. The equation that describes its evolution is called "*kinetic equation*". The first model of this type was proposed by Tanaka and coworkers [68] and was initially thought to describe three dimensional problems involving SMAs, but it has been implemented only for one dimensional problems. Exponential functions were considered to describe the martensitic fraction in terms of stress and temperature. Liang and Rogers (1990) [69] presented an alternative evolution law for the volumetric fraction based on cosine functions. In 1993, Brinson [70, 71] proposed an approach in which two different kinds of martensite were considered: temperature-induced and stress-induced martensite (section 1.3), and also the elastic modulus has been considered as a function of the martensite fraction.

Great efforts have been made in constitutive modelling, but there has not been enough attention to the corresponding numerical implementation. This is due to the low propensity of the constitutive models to be numerically implemented. Moreover, the high non linear behaviour of the material and the complicated structure of models are other obstacles in numerical implementation. New development in 3D phenomenological constitutive models still have to be done to reach a better computational tool for design and analysis of SMA devices and structures.
The model that we have adopted for our simulation and calculations is the Brinson's model. This model is more useful to understand the behaviour of the SMA wires that we will employ, it matches well with experimental results, especially in one dimensional cases and can be easily simulated. However, this model is not very suitable to be implemented in a control system. After having described the model, we will discuss its limits and briefly talk about the control systems that are used in applications with SMA wires.

3.1 Brinson's model

In this section we will describe the one dimensional Brinson's constitutive model for SMA specimen that are thermally activated by current heating [70, 2]. The aim of this model is to describe the stress-strain behaviour in terms of temperature and time. In this model, the system is described on the basis of two equations: the *constitutive law* which describes the relation between stress, strain and the volume fraction of martensite in the material, and the *kinetic law* which describes the dependence of the volume fraction of martensite from temperature and stress. The evolution of the system in time is then obtained using the Joule's heating equation, considering the electrical heating of the SMA.

3.1.1 Constitutive law

Since the Brinson's model considers the presence of both stress and temperature induced martensite, the total volumetric fraction of martensite ξ is:

$$\xi = \xi_S + \xi_T \tag{3.1}$$

where ξ_S is the volumetric fraction of stressed induced (detwinned) martensite and ξ_T the fraction of temperature induced (twinned) martensite.
Considering a shape memory alloy specimen that is subjected to a tensile load along one axis, from statistical mechanics considerations [69, 70], it is possible to retrieve the constitutive law:

$$d\sigma = \frac{\partial \sigma}{\partial S} dS + \frac{\partial \sigma}{\partial \xi_S} d\xi_S + \frac{\partial \sigma}{\partial \xi_T} d\xi_T + \frac{\partial \sigma}{\partial T} dT \tag{3.2}$$

which can be written as:

$$d\sigma = Y dS + \Omega_S d\xi_S + \Omega_T d\xi_T + \Theta dT \tag{3.3}$$

where Y is the Young's modulus, Ω_S and Ω_T the transformation coefficients correspondent to the two types of martensite and Θ the coefficient of thermal expansion.
By assuming these coefficient constant and solving the previous equation considering the initial conditions σ_0, S_0, $\xi_{S,0}$, $\xi_{T,0}$, T_0 we obtain:

$$\sigma - \sigma_0 = Y(S - S_0) + \Omega_S(\xi_S - \xi_{S,0}) + \Omega_T(\xi_T - \xi_{T,0}) + \Theta(T - T_0) \tag{3.4}$$

The transformation coefficients can be obtained considering two different hysteresis processes. Consider a specimen in the initial conditions of zero strain and zero stress, $S_0 = 0$ and $\sigma_0 = 0$, in a full austenic phase, $\xi_{S,0} = \xi_{T,0} = 0$, at a temperature below the austenic start temperature A_S. If the material is loaded until it reaches the total martensitic phase and then unloaded to the condition of zero stress, as previously stated in section 1.3, a residual strain S_L remains and the final martensitic fractions are: $\xi_S = 1$ and $\xi_T = 0$. The constitutive law 3.4 hence becomes:

$$0 - 0 = Y(S_L - 0) + \Omega_S(1 - 0) + \Omega_T(0 - 0) - \Theta(T_0 - T_0) \tag{3.5}$$

and the solution of this expression is:

$$\Omega_S = -Y \cdot S_L \tag{3.6}$$

Note that S_L is the maximum residual strain that is possible to obtain. If the phase transformation is not complete, it is possible to obtain a residual strain lower than S_L. So, for a generic transformation of this type, we have $S_{res} \leq S_L$.

If we consider the same transformation as before, but with the material in a initial condition of fully temperature induced martensite, the constitutive law 3.4 becomes:

$$0 - 0 = Y(S_L - 0) + \Omega_S(1 - 0) + \Omega_T(0 - 1) - \Theta(T_0 - T_0) \tag{3.7}$$

Solving this expression, we obtain:

$$\Omega_T = 0 \tag{3.8}$$

In the light of these results, the constitutive law becomes:

$$\sigma - \sigma_0 = Y(S - S_0) + \Omega_S(\xi_S - \xi_{S,0}) + \Theta(T - T_0) \tag{3.9}$$

The constitutive equation 3.9 is quite trivial to obtain. However, experimental evidence shows how the Young's modulus has a strong dependence from the total fraction of martensite. As assumed by Tanaka [68] and Liang [69], Brinson assumes that the Young's modulus varies linearly with the total volumetric fraction of martensite:

$$Y(\xi) = Y_A + (Y_M - Y_A) \cdot \xi \tag{3.10}$$

where Y_M and Y_A are the Young's moduli in the totally martensitic and totally austenitic conditions respectively. Since, in the case of constant values, the condition of residual strain requires that the transformation coefficient Ω_S is related to the Young's modulus, it is reasonable to assume that also Ω_S is function of ξ. Expanding in a Taylor Series about ξ_0 and stopping the expansion at the first order:

$$\Omega_S = \Omega_S(\xi_0) + (\xi - \xi_0)\dot{\Omega}_S(\xi_0) \tag{3.11}$$

Substituting eq. 3.10 in 3.11 and assuming that $\Omega_S(\xi_0) = -Y(\xi_0)S_L$ (as previously derived):

$$\Omega_S(\xi) = -S_L Y(\xi_0) + (\xi - \xi_0)[-S_L \dot{Y}(\xi_0)] \tag{3.12a}$$
$$\Omega_S(\xi) = -S_L Y_A - S_L \xi (Y_M - Y_A) \tag{3.12b}$$
$$\Omega_S(\xi) = -S_L Y(\xi) \tag{3.12c}$$

According to the derivation for constant values of the coefficients, we consider $\Omega_T = 0$ and, due to the relatively small value of Θ (five orders of magnitude less than $Y(\xi)$ [70]), we neglect the term of the thermal expansion. Renaming Ω_S as Ω and taking into account the results, eq. 3.9 can be rewritten as:

$$d\sigma = Y(\xi)dS + \Omega(\xi)d\xi_S \tag{3.13}$$

with:

$$\Omega(\xi) = -S_L Y(\xi) \tag{3.14}$$

Integrating this differential equation:

$$\int d\sigma = \int [Y_A + \xi(Y_M - Y_A)]dS - S_L \int [Y_A + \xi(Y_M - Y_A)]d\xi_S \tag{3.15}$$

we obtain:

$$\sigma + K = Y_A S + \xi(Y_M - Y_A)S + C(\xi) - S_L Y_A \xi_S - S_L(Y_M - Y_A)\left[\xi_T \xi_S + \frac{\xi_S^2}{2}\right] \tag{3.16}$$

where K is an arbitrary constant and $C(\xi)$ an arbitrary function of ξ.
Rearranging the terms and recognizing that:

$$Y(\xi)\xi_S = Y_A \xi_S + (Y_A - Y_M)\xi_S^2 + (Y_A - Y_M)\xi_S \xi_T \tag{3.17}$$
$$-(Y_A - Y_M)\xi_S \xi_T = Y_A \xi_S + (Y_A - Y_M)\xi_S^2 - Y(\xi)\xi_S \tag{3.18}$$

we obtain:

$$\sigma + K = [Y_A + \xi(Y_M - Y_A)]S + C(\xi) - S_L Y_A \xi_S - S_L(Y_M - Y_A)\frac{\xi_S^2}{2} + \\ + S_L Y_A \xi_S + S_L(Y_M - Y_A)\xi_S^2 - S_L Y(\xi)\xi_S \tag{3.19a}$$

$$\sigma + K = Y(\xi)S + \Omega(\xi)\xi_S + S_L(Y_M - Y_A)\xi_S^2 + C(\xi) \tag{3.19b}$$

Applying the initial conditions S_0, $\xi_{S,0}$, σ_0 the constant K results:

$$K = Y(\xi_0)S + \Omega(\xi_0)\xi_{S,0} + S_L(Y_M - Y_A)\xi_{S,0}^2 + C(\xi_0) \tag{3.20}$$

and the constitutive law becomes:

$$\sigma - \sigma_0 = Y(\xi)S - Y(\xi_0)S_0 + \Omega(\xi)\xi_S - \Omega(\xi_0)\xi_{S,0} + (Y_M - Y_A)\left[\frac{\xi_S^2}{2} - \frac{\xi_{S,0}^2}{2}\right] + C(\xi) - C(\xi_0) \tag{3.21}$$

If we imagine, to load the material from a condition of zero stress and strain until it reaches a martensitic fraction ξ_S and then to unload it to the condition of zero stress, a residual strain $S_{res} \leq S_L$ remains and the final martensitic fractions are: ξ_S and $\xi_{T,0} = 0$. Since the residual strain is due to the "physical memory" that the alloy has of the stress it has undergone and that the maximum residual strain S_L is the strain that remains upon unloading a material that has been sufficiently stressed to become totally martensitic ($\xi_S = 1$), it is reasonable to imagine that the generic residual strain can be written as:

$$S_{res} = S_L \xi_S \tag{3.22}$$

Consequently, considering a transformation of loading and unloading as that previously described with initial conditions: $\sigma_0 = 0$, $\xi_{S,0}$, $\xi_{T,0}$, $S_0 = S_L \xi_{S,0}$ and final conditions $\sigma = 0$, ξ_S, $\xi_T = \xi_{T,0}$, $S = S_{res} = S_L \xi_S$, remembering eq. 3.1 the constitutive law is:

$$0 - 0 = Y(\xi)S_{res} - Y(\xi_0)\cdot S_0 + \Omega(\xi)\xi_S + \Omega(\xi)\xi_S - \Omega(\xi_0)\xi_{S,0} + (Y_M - Y_A)\left[\frac{\xi_S^2}{2} - \frac{\xi_{S,0}^2}{2}\right] + C(\xi) - C(\xi_0) \tag{3.23}$$

that, recalling eq. 3.14 and eq. 3.22, yelds to:

$$C(\xi) = C(\xi_0) - (Y_M - Y_A)\left[\frac{\xi_S^2}{2} - \frac{\xi_{S,0}^2}{2}\right] \tag{3.24}$$

We can now write the final form of the constitutive law substituting eq. 3.24 into 3.21 :

$$\sigma - \sigma_0 = Y(\xi)S - Y(\xi_0)S_0 - S_L(Y(\xi)\xi_S - Y(\xi_0)\xi_{S,0}) \tag{3.25}$$

The first two terms of eq. 3.25 corresponds to the generic Hooke's law with a non-constant Young's modulus, while the other two terms show a linear dependance of the stress from the martensitic fraction present in the shape memory alloy.

3.1.2 Kinetic law

The kinetic law describes how the martensitic fraction varies as function of the stress and temperature. Since Brinson takes into account both types of martensitic fractions, ξ_S and ξ_T, and since the tranformations are not univocal in the direction (see section 1.3), the kinetic law is quite complicated. Recalling that the transition temperatures are different if the material is changing form martensite to austenite or *vice versa*, it can be noticed that also the kinetic law

has to be different in the two cases. First we suppose that the transition temperatures depend on stress with linear coefficients $1/C_A$ and $1/C_M$:

$$M^*_{s,f} = M_{s,f} + \frac{\sigma}{C_M} \tag{3.26a}$$

$$A^*_{s,f} = A_{s,f} + \frac{\sigma}{C_A} \tag{3.26b}$$

Furthermore, sufficiently increasing the stress below the martensitic finish temperature M_F yelds to stressed induced martensite but decreasing it does not lead to temperature induced martensite but to a maintainance of the fraction of stressed induced martensite. Brinson considers the change of the martensitic fraction to be a cosine function of stress and temperature, and takes into account all the possible transformations. We here report the kinetic law in all the different cases in conjunction to the phase diagram in fig. 3.1.

- From martensite to austenite: $T > A_s$ and $C_A(T - A_f) < \sigma < C_A(T - A_s)$

$$\xi = \frac{\xi_0}{2}\left\{cos\Big[a_A\big(T - A_f - \frac{\sigma}{C_A}\big)\Big] + 1\right\} \tag{3.27a}$$

$$\xi_S = \frac{\xi_{S,0}}{\xi_0}\xi \tag{3.27b}$$

$$\xi_T = \frac{\xi_{T,0}}{\xi_0}\xi \tag{3.27c}$$

$$a_A = \frac{\pi}{A_f - A_s} \tag{3.27d}$$

- From austenite to martensite: $T > M_s$ and $\sigma^{cr}_S + C_M(T - M_s) < \sigma < \sigma cr_f + C_M(T - M_s)$

$$\xi_S = \frac{1 - \xi_{S,0}}{2} cos\left\{\frac{\pi}{\sigma_s - \sigma_f}\Big[\sigma - \sigma_f - C_M(T - M_s)\Big]\right\} \tag{3.28a}$$

$$\xi_T = \xi_{T,0} + \frac{\xi_{T,0}}{1 - \xi_{S,0}}(\xi_S - \xi_{S,0}) \tag{3.28b}$$

$$\xi = \xi_T + \xi_S \tag{3.28c}$$

- From austenite to martensite: $T < M_s$ and $\sigma^{cr}_s < \sigma < \sigma^{cr}_f$

$$\xi_S = \frac{1 - \xi_{S,0}}{2} cos\Big[\frac{\pi}{\sigma^{cr}_s - \sigma^{cr}_f}(\sigma - \sigma^{cr}_f)\Big] + \frac{1 + \xi_{S,0}}{2} \tag{3.29a}$$

$$\xi_T = \xi_{T,0} - \frac{\xi_{T,0}}{1 - \xi_{S,0}}(\xi_S - \xi_{S,0}) + \Delta(T, \xi_{T,0}) \tag{3.29b}$$

with (3.29c)

$$\Delta(T, \xi_{T,0}) = \frac{1 - \xi_{T,0}}{2}\Big[cos\Big[a_M(T - M_f)\Big] + 1\Big] \tag{3.29d}$$

$$a_M = \frac{\pi}{M_s - M_f} \tag{3.29e}$$

if $M_f < T < M_s$ and $T < T_0$, otherwise

$$\Delta(T, \xi_{T,0}) = 0 \tag{3.29f}$$

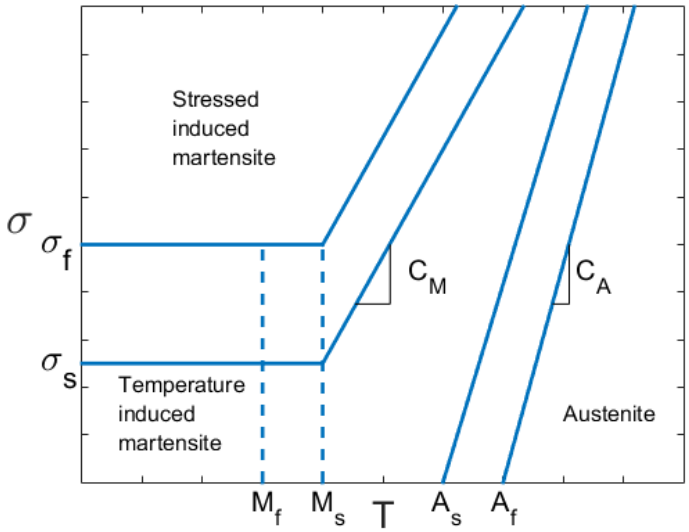

Figure 3.1: Generic phase diagram for shape memory alloys. Stress is on the y axis, temperature on the x axis. M_f, M_s, A_s, A_f are the transition temperatures at zero stress while σ_s^{cr} and σ_f^{cr} are the start and final critical stresses at which the transformation from temperature induced to stressed induced martensite respectively starts and finishes.

3.1.3 Free strain recovery

Let's imagine that the material, in an initial zero strain condition and with no boundary constraints, is loaded at a temperature lower than A_s until a certain fraction of stressed induced martensite ξ_M creates in the material and then unloaded to zero stress. Residual strain is $S_{res} = S_L \xi_M$. If we increase the temperature below A_s the material starts changing towards the austenitic phase and the transformation will be complete if the temperature exceeds A_f. In such case, since stress is constant during the transformation (in this case it is zero), the strain can be analytically obtained using the constitutive law (eq. 3.25) and the kinetic law (eq. 3.27):

$$S = \frac{S_{res}}{2}\left\{cos\left[a_A\left(T - A_f - \frac{\sigma}{C_A}\right)\right] + 1\right\} \tag{3.30}$$

If the temperature returns to the initial value no strain change remains.

Matlab simulation of SMAs

A shape memory effect and a pseudoelasticity cycles have been simulated with Matlab using the constitutive and kinetic laws on a shape memory alloy wire. The parameters of the model that depend on the specimen properties have been assumed as from literature [2]. The results of these first simulations are shown in fig. 3.2 and 3.3.

- Shape Memory Effect (3.2a,3.3a): The specimen is initially at zero stress and strain in a complete temperature induced martensite phase. It is loaded until it is completely changed in stress induced martensite (blue arrow), then it is unloaded (red arrow) and a residual strain $S_{res} = 0.06$ remains, as shown in 3.3a. Increasing temperature at a higher value than A_f (green arrow) the material becomes completely austenitic and a strain recovery shows up (see 3.3a). Decreasing temperature to the initial value (magenta arrow) does not lead to

a strain change and the material recovers the initial temperature induced martensite phase.

- Pseudoelastic Effect (3.2b,3.3b): The specimen is loaded (blue arrow) and unloaded (red arrow) at a temperature above A_f. Loading leads to a strain change in the material that is then recovered when the stress is reduced to zero.

3.1.4 Controlled recovery with bias spring

In many applications, SMA wire actuators are used to move spring-like objects, i.e. which respond with a force that is proportional to their displacement. Suppose now to fix one extreme of a wire of shape memory alloy and to bound the other one to a bias spring of stiffness k, as explained in figure 3.4a. If the wire is initially at zero stress and strain and the spring is pulled and then fixed (or you fix the spring and pull the wire, it's the same), the relationship between the stress and the strain of the wire will be:

$$\sigma - \sigma_0 = \frac{kL}{A}(S_0 - S) \tag{3.31}$$

where L is the length of the specimen along the direction of stress and A is the cross-sectional area, S_0 the initial strain and T_0 the initial stress which depends on how much the spring has been pulled. Using eq. 3.31, the strain can be written as a function of the stress:

$$S = S_0 - (T - T_0)\frac{A}{kL} \tag{3.32}$$

and rearranging the constitutive law 3.25, we can write:

$$\big(\sigma - \sigma_0\big)\left[1 + \frac{Y(\xi)A}{kL}\right] = \big(Y(\xi) - Y(\xi_0)\big)S_0 - \big(Y(\xi)\xi_S - Y(\xi_0)\xi_{S,0}\big)S_L \tag{3.33}$$

Since ξ_S and ξ are function of temperature and stress, which are inside the argument of cosine functions, the eq. 3.33 can not be solved analytically. It can be noticed that, choosing a temperature, eq. 3.33 can be written as:

$$g(\sigma) = \sigma - \sigma_0 - f(\sigma) = 0 \tag{3.34}$$

This relationship can be solved numerically to determine the stress that corresponds to the chosen temperature.

Matlab simulation of SMAs

The behaviour of the previously described system has been simulated with Matlab, changing the temperature of the wire. The considered properties of the wire are the same as in the previous simulations. The initial temperature has been chosen under A_s, and the system has been sufficiently prestressed to induce a transformation in complete stressed induced martensite. When the temperature is increased below $A_s^* = A_s + \sigma/C_A$, the wire starts contracting and the stress rises because of the effect of the spring. The transformation in the austenitic phase completes when $A_f^* = A_f + \sigma/C_A$. Decreasing the temperature, the system returns at the initial conditions. The interval between initial and final temperature has been divided in a certain number of values. The stress that corresponds to each value of temperature has been calculated solving numerically eq. 3.34. Since the zeros could be more than one, the solution has been chosen as the nearest to the previous one, providing an efficient method. The results of the simulation and the phase diagram of the transformations can be seen in fig. 3.4c.

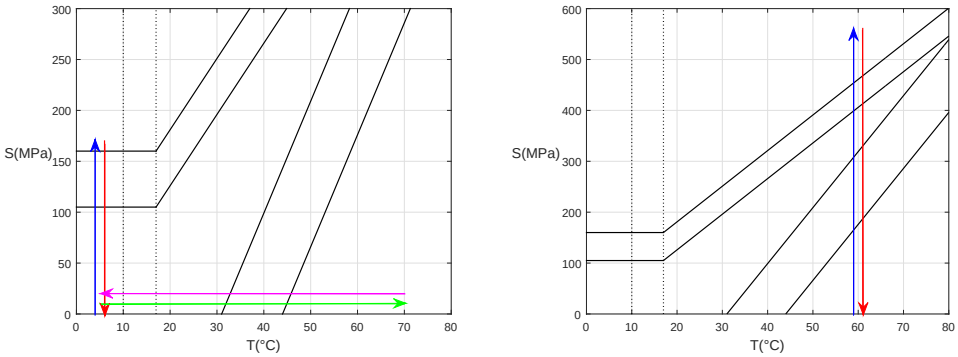

(a) (b)

Figure 3.2: Phase diagrams with simulated Shape Memory (3.2a) and Pseudoelastic (3.2b) cycles. The blue and the red arrows, as the green and the magenta ones, should be superimposed since they correspond to transformations occurred at the same temperature or stress, but they are kept separated for clarity.

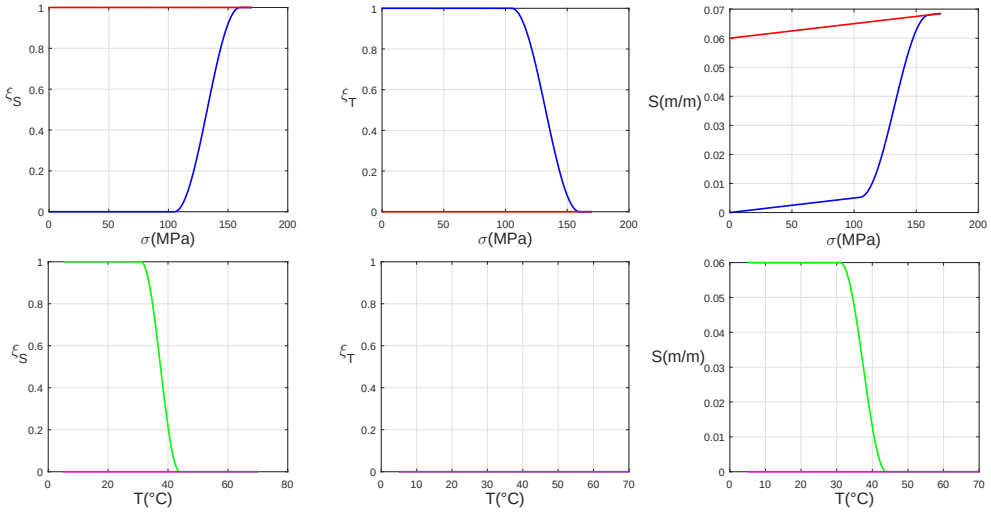

(a) Volumetric fraction of stress induced and temperature induced martensite and strain during the transformation of the SME cycle. Values are plotted as function of stress or temperature depending on which one is varied in the transformations. The colors refer to the transformations of fig. 3.2a.

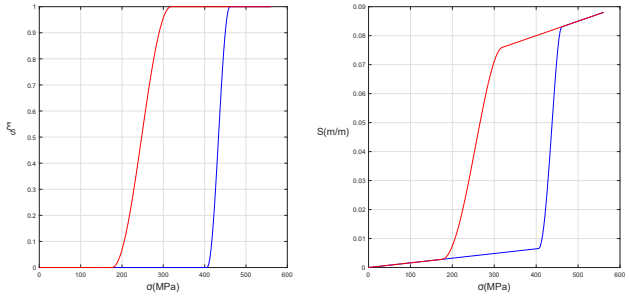

(b) Volumetric fraction of stressed induced martensite and strain during the tranformation of a PSE cycle. They are plotted as function of stress,since temperature is maintained constant. The colors refer to the transformations of fig. 3.2b.

Figure 3.3: Results of a simulation of the Shape Memory and Pseudoelastic Effects.

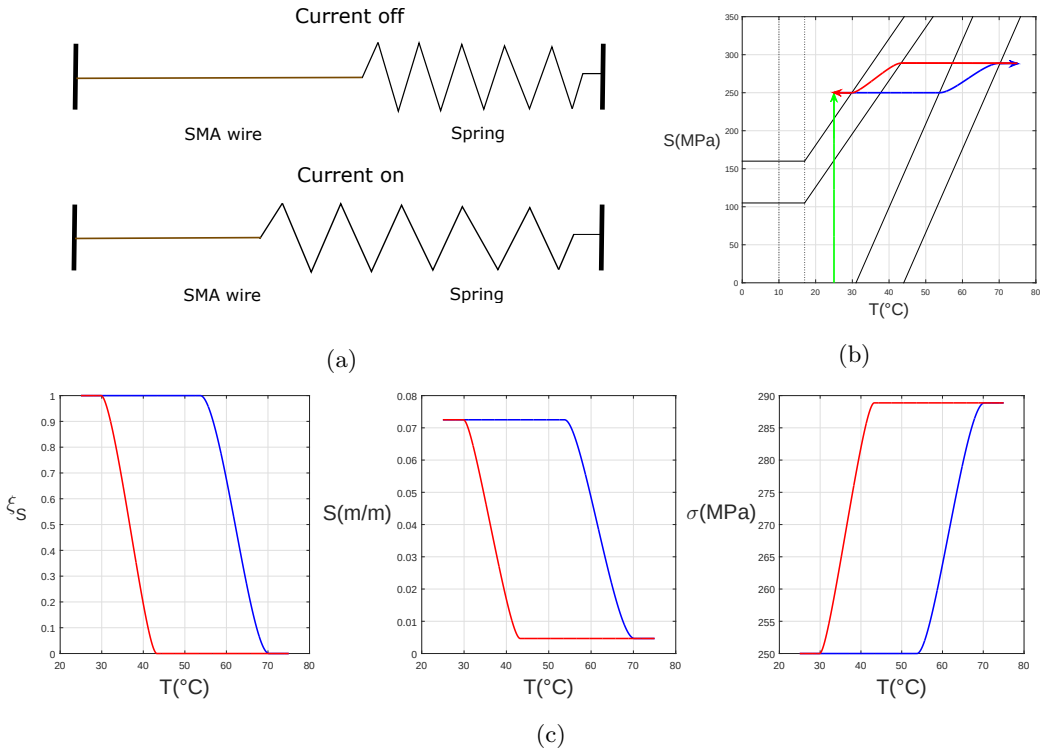

Figure 3.4: (a) Schematic representation of a system of a SMA wire and a bias spring. The wire is stressed by the spring. When current is incresed, the temperature of the wire rises implying a strain recovery of the wire and a stretching of the spring. (b) Phase diagram with a simulated cycle of the transformation of a SMA wire bounded to a bias spring. (c) Volumetric fraction of stress induced and temperature induced martensite and strain during increasing and decreasing temperature in a SMA wire with a bias spring. They are plotted as function of stress or temperature depending on which is varied in the transformations. The colors refer to the transformations of fig. 3.4c.

3.2 Electrical activation of a SMA wire

As previously mentioned, since SMAs are metals, it is possible to increase their temperature with current to control the strain recovery. To understand the relationship between current and temperature in the material we have to consider the heat transfer associated to the electrical heating, employing the *Joule heating* equation. If we consider a SMA wire with length L and circular section with diameter D, the equation is:

$$(\rho V)c_p\frac{dT(t)}{dt} = i^2R - h_cA_c\big(T(t) - T_\infty\big) \tag{3.35}$$

where ρ is the density of the material, V its volume, c_p the specific heat, i the current, R the wire resistance, h_c the heat transfer coefficient and $A_c = \pi DL$ is the circumferential area and T_∞ is the ambient temperature. Assuming that current and ambient temperature are constants, the solution of equation 3.35 is:

$$T(t) - T_\infty = \frac{R}{h_cA_c}\Big(1 - e^{-\frac{t}{t_h}}\Big)i^2 + \Big(T_0 - T_\infty\Big)e^{-\frac{t}{t_h}} \tag{3.36}$$

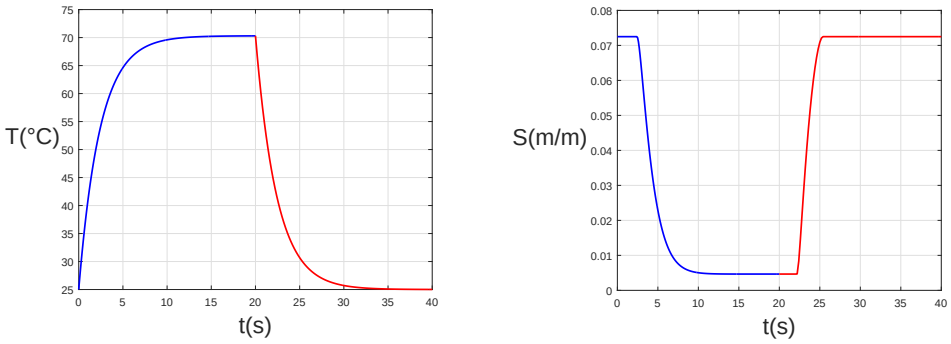

(a) (b)

Figure 3.5: (a) Simulated evolution in time of the temperature of a SMA wire when heated with current (red line) and then when it cools down (blue line). The time employed by temperature to stabilize when cooling or heating is the same. (b) Simulated evolution in time of the strain of a SMA wire when heated with current (blue line) and then when it cools down (red line). The temperature induced transformation is complete. When the wire cools down it returns to the initial value because it is bounded to a bias spring as in the example of figure 3.4c. The time employed by strain to stabilize when cooling or heating is not the same because the transition temperatures at which it changes are different in the two cases.

where the time constant t_h is defined as:

$$t_h = \frac{\rho V c_p}{h_c A_c} = \frac{\rho \pi r c_p}{2 h_c \pi} \tag{3.37}$$

and since A_c is proportional to L, the time constant is independent from the length of the wire but depends on the radius of the wire section When the initial temperature is equal to the ambient temperature the second term of eq. 3.36 is zero and we have:

$$T(t) - T_\infty = \frac{R}{h_c A_c}\left(1 - e^{-\frac{t}{t_h}}\right) i^2 \tag{3.38}$$

The steady temperature T_s is obtained by letting t going to infinite:

$$T_s = \frac{R}{h_c A_c} i^2 + T_\infty \tag{3.39}$$

An example of the evolution of temperature in time, and consequently of strain, when heating or cooling a SMA wire is reported in fig. 3.5.
It can be easily seen that the proportional constant between the steady state temperature and the square current does not depend on the wire length since the resistance of the wire is $R = \frac{rL}{A}$ where r is the resistivity of the material, L the length of the wire and A the cross-sectional area. The time employed to reach the desired temperature can be lowered when heating by applying a higher current than that needed to reach the desired temperature and, when it is reached, adjusting its value to that necessary to maintain the steady state. This improvement of the response in time can not be realized when cooling, because time depends only from the initial and final temperatures. An example of a possible improvement of the rising time is shown in fig. 3.6 while the decreasing time can be improved creating external conditions which reduce the time constant t_h or using peltier cells [72].

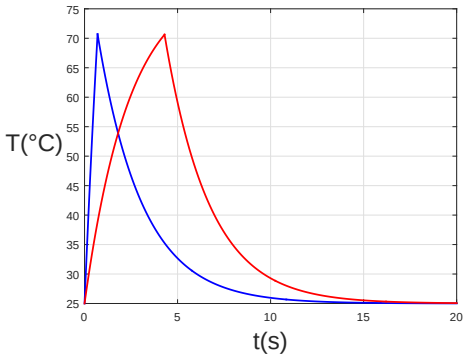

Figure 3.6: Simulated curves representing the temperature of a SMA wire heated with current and then let cooling down when a certain temperature has been reached. The rising time of the blue curve is lower than that of the red one because, in the former case, the current used to heat the wire is quite higher than that needed to reach the desired temperature value while, in the latter, it is only a bit higher.

3.3 SMA wires actuation control

An actuation system that employs a SMA wire is usually composed by two elements: the SMA wire and an element that is used to develop a bias force needed to strain the wire in the state of no applied current. Actuation systems with SMA wires can be divided into three types on the basis of the element that is used to develop the bias force:

- **SMA wire under constant load** - The simplest way an actuator with a SMA wire can be created with is to put the wire under constant load. At ambient temperature, the wire is strained under the stress of the load and contracts when heated leading to a displacement of the loading element.
- **SMA wire and spring-like element** - Alternatively the bias force can be provided by a spring-like element, i.e. that exerts a force proportional to its displacement.
- **Antagonistic SMA wires** - With the previous methods, the response of the system is limited when cooling down by the time constant with which the wire responds. Using two antagonistic wires permits to control the movement in both directions because when one wire is heated the other provides a bias force and *vice versa*.

Whatever it is the actuation mechanism, the control systems of SMA actuators have to face the main problem of hysteresis. The behaviour of a SMA element can be described with four variables: temperature, generated force or stress, displacement or strain and the electric resistance. Each of these variables can be chosen as feedback parameter for the control system. Control systems for SMAs actuators can be divided into two types: actuation systems with a sensor and sensorless systems. If you decide to use displacement, force or temperature, you will need a sensor. Displacement is the most used feedback variable because a simple potentiometer can be used as sensor [25]. Force can be measured using a strain gauge. The temperature feedback is not practical because it needs a thermal sensor isolated from the SMA element and it is difficult to measure the temperature of a little SMA element, as a wire. But even if these problems would be overcome, the relationship between temperature and strain shows up hysteresis. However, actuation systems with sensors present a higher size and cost and are not suitable for small applications.
As an alternative, electrical resistance (ER) can be measured without using any sensor, simply by monitoring the current and the voltage difference at the ends of the wire. Furthermore, ER

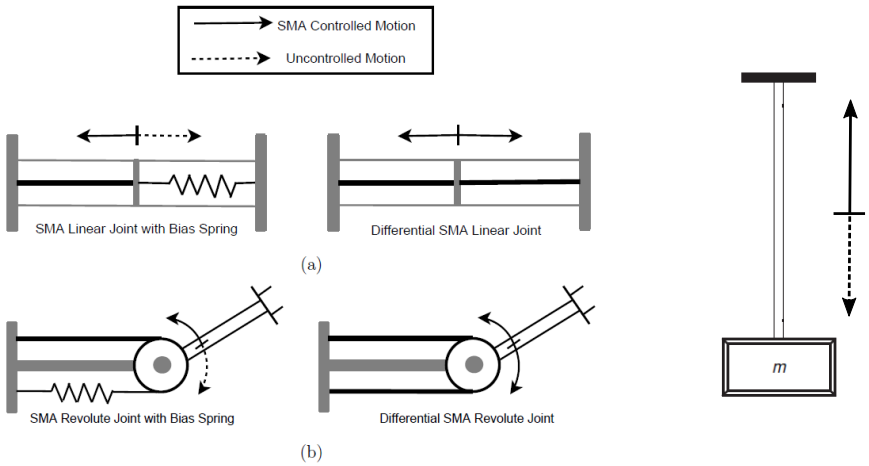

Figure 3.7: Types of actuators exploiting SMA wires [65, 2].

shows a linear dependence from strain under certain conditions and can overcome the hysteresis problem. As common metals, the ER of SMAs changes linearly with temperature and stress at a stable individual phase. However, the ER is also closely related to phase transformations induced by stress and/or temperature and martensite reorientation induced by applied stress, which is in contrast to the behaviour of common metals. Besides, it is possible that a third phase, called *R-phase* because of the rhombohedral crystal structure, appears between the martensitic and austenitic phase [1]. As stated in [1], the presence of the R-phase is also related to the percentages of alloying. When the R-phase appears in SMA, the ER also changes linearly with R-phase distortion induced by temperature. Consequently, ER variations are attributed to the direct and indirect effect of stress and/or temperature for a certain given SMA wire. But as demonstrated in [73, 74], when the applied stress is large enough (see fig. 3.8), R-phase is inhibited and the relationship between ER and strain is linear. However, when the applied stress is small, the resistance-strain curve has two different trends with very different slopes during cooling and heating, caused by the presence of the R-phase. So, ER can be used as feedback parameter only in condition of sufficient stress to eliminate the R-phase. In [73] it has also been demonstrated that also using a bias spring, so with stress that varies during the phase transformations, the resistance presents a negligible hysteresis and can be used as feedback parameter.
PI [75], PID [76, 77, 78], fuzzy-logic [79] and neural networks [80] control have been exploited as resistance feedback control systems in several applications.

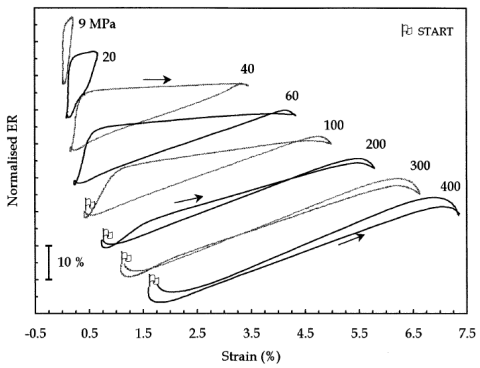

Figure 3.8: Electrical resistance hysteresis cycles at different stress values [74].

Chapter 4

Characterization of the SMA wires

4.1 Methods of characterization for SMAs

In order to develop an accurate model to predict the behaviour of SMAs, it is of fundamental importance to characterize these materials. In general, the characterization of SMAs properties is based on the same principles used to test other materials, but particular considerations are required due to their complex behaviour.
As described in detail in chapter 1, the parameters required to construct the phase diagram and completely describe the SMAs behaviour are:

- The transition temperatures at zero stress: M_f, M_s, A_s and A_f.
- The *stress influence coefficients* C_M and C_A which determine the linear relationship between transition temperatures and stress.
- The start and finish stresses σ_s and σ_f for the detwinning of temperature induced to stressed induced martensite.
- The Young's moduli in the austenitic and martensitic phases, Y_A and Y_M.
- The coefficients of thermal expansion in the austenitic and martensitic phases, α_A and α_M.
- The *maximum residual strain* S_L.

Since SMAs exhibit a particular thermomechanical coupling is necessary to define specific *loading paths* to be applied to the material in order to derive the required parameters. Standard methods for SMAs characterization usually consist in:

- **Differential scanning calorimeter (DSC) testing** - Employing a DSC, the heat flow to the SMA specimen is measured while its temperature is varied. When temperature is increased the heat flow is positive and presents a positive peak when the transformation from martensite to austenite happens. On the contrary, when temperature is decreased the heat flow presents a negative peak in correspondence to the phase change. From the initial and final temperature of the heat flow peaks it is possible to determine the initial and final transition temperatures. An example is shown in fig. 4.1 where the intersections between tangent lines to the base line of the heat flow curve and to the initial and final part of the peak are considered as possible values of the transition temperatures.

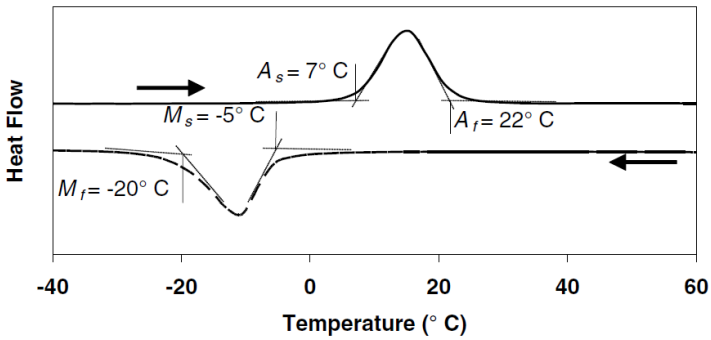

Figure 4.1: Determination of stress-free transformation temperatures from DSC testing using tangent lines to the curve (NiTi, untrained material) [1].

- **Monotonic loading** - The specimen is monotonically mechanically loaded and unloaded at a temperature lower than M_f. Following this loading path, the specimen undergoes a transformation from temperature induced to stressed induced martensite. The transformation occurs between the initial σ_s and final σ_f critical stresses. Monitoring the load with a load cell and the strain, it is possible to esteem the two critical values as can be seen in fig. 4.2a. From such loading path it also possible to determine the maximum residual strain value as the strain that remains after the full transformation.
  If the same loading and unloading is performed at a temperature above A_f, the specimen exhibits the so called pseudoelastic effect changing from austenite to martensite and *vice versa*. Again, monitoring the applied load and strain, it is possible to measure the Young moduli in the austenitic and martensitic phases by a linear fit in the stress-strain graph. As can be seen in fig. 4.2b, the values of the Young's modulus in the martensitic phase measured with the paths at temperatures under M_f (fig. 4.2a) is higher than that measured at a temperature above A_f (fig. 4.2b). Since that reported in fig. 4.2 are real cases, this fact can be due to the remaining of austenite in the latter case.

- **Isobaric testing** - The temperature of the specimen is varied at a constant value of stress. In such case the specimen undergoes a shape change. Monitoring the strain, it is possible to determine the transition temperatures, by linear fitting of the strain-temperature curves, at that specific value of stress (see 4.3a). Repeating the test at different values of stress it is possible to determine the *stress influence coefficients* C_M and C_A as can be seen in fig. 4.3b.
  From the strain-temperature data is also possible to determine the coefficient of thermal expansion by linear fits of the curves below A_s when temperature increases and above M_s when temperature decreases.

- **Cyclic loading** - To determine the effects of cyclic loading the specimen is subjected to a repetitive thermomechanical transformation. This transformation can consist in the variation of temperature with a constant load or the same transformation that the specimen has to undergo in the application in which it will be inserted. The latter case is often referred as *training*. For example a SMA wire that has to be used in a actuation system with a bias spring would be tested with multiple thermal cycles when attached to the bias spring in order to understand the material response to the effective transformation it will have to undergo. If the material response stabilizes under cycling transformation (as usually occurs), the material should be tested with a number of cycles superior to those that the material would undergo in the application. In fig. 4.4 the results of multiple cycling under constant load of a SMA specimen are shown.

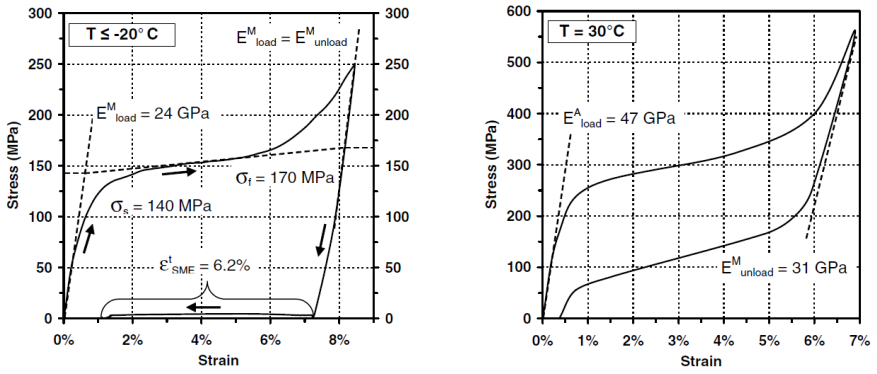

(a) (b)

Figure 4.2: (a) Monotonic loading test at $T < M_f$ [1]. (b) Monotonic loading test at $T > A_f$ [1]. The Young's modulus is here named by E.

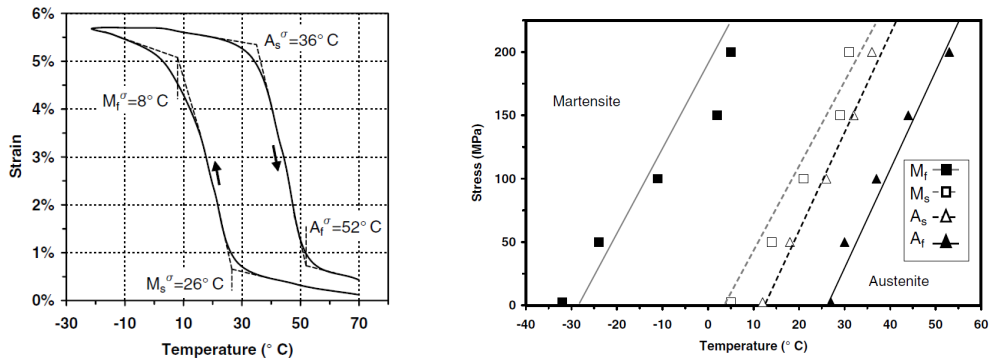

(a) (b)

Figure 4.3: (a) Strain of a SMA element under constant stress when its temperature is varied. The transformation temperatures at constant stress are determined as the interseption of lines tangent to the strain curve as shown in the graph. (b) Evaluation of the *stress influence coefficients* by linear fitting of the transition temperatures determined at different stress values [1].

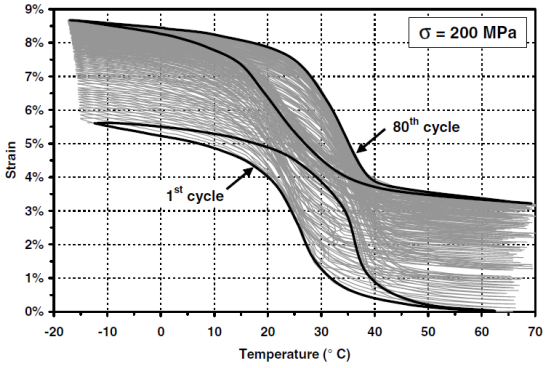

Figure 4.4: Results of an isobaric test at 200 MPa [1]. The response stabilizes after about 80 cycles.

4.2 Objectives of the characterization

The previously listed experiments to characterize SMAs are usually executed with special equipments like DSCs or servohydraulic machines with integrated load cells and strain gauges. Since we have none of these equipments, we have designed our own method to determine good estimates of the quantities we are interested in.
First of all, the SMA specimen that we had to test is wire shaped. This is a strong limit because the zero stress strain is difficult to determine, since SMA wires are not straight without a minimum stress but they curl.
Critical stresses are usually measured exploiting a load cell. Since we are not truly interested in knowing critical stresses but we only want to be certain that the wires are sufficiently stressed to be completely in the stressed induced martensitic phase, we have only confirm this condition considering data sheet information (suggested and maximum force) and experimental results.
We are interested in evaluating the strain capabilities of the wire and the necessary currents that we need to control it. However, the temperature of a SMA wires is not easily measurable because every contact with the wire would influence it. Furthermore, we are not interested in the temperature directly but we want to evaluate the current that we need to control the wire. From section 3.2, we know that if we are in a steady state condition, the temperature is proportional to the square of the current:

$$T_s = T_\infty + \frac{R}{h_c A_c} I^2 \tag{4.1}$$

Then, if we are in a steady state condition, we can consider the correspondent *transitions currents* instead of *transition temperatures*. This transition currents still linearly depend on stress. We can rewrite the kinetic laws as function of current instead of temperature. This is very useful since we want to use current to control the strain of the wire. Unfortunately, the coefficient of proportionality between temperature and the square current depends on the external conditions because it contains h_c, the heat flow coefficient. Because of this strong dependence from external conditions the transition currents calculated with the characterization setup will be different from that in the device, where external conditions will be different. So, the estimates of transition currents will have to be done again when the device will be tested. However, an initial evaluation of transition currents has been carried out in order to have an initial estimate of the values.
It is worth to remember that the coefficient of proportionality between the temperature and the square current does not depend on the length of the wire but only from its diameter and resistivity. Moreover, since the variation of resistivity with temperature is small, we can consider the coefficient as constant once the external conditions and the wire diameter are determined.
Since we are interested in working only with the wire in stressed induced martensite and austenite conditions, we can consider only one type of martensite (the stressed induced one), that we now call ξ.
The kinetic laws that we consider for our wires are:

- Austenite to martensite

$$\xi = \frac{1-\xi_0}{2} cos\left[\frac{\pi}{I^2_{M_s,0} - I^2_{M_f,0}}\left(I^2 - \frac{\sigma}{C_{M,I}} - I^2_{M_f,0}\right)\right] + \frac{1+\xi_0}{2} \tag{4.2}$$

- Martensite to austenite

$$\xi = \xi_0 cos\left[\frac{\pi}{I^2_{A_f,0} - I^2_{A_s,0}}\left(I^2 - \frac{\sigma}{C_{A,I}} - I^2_{A_s,0}\right)\right] \tag{4.3}$$

where ξ_0 is the initial fraction of martensite and $I^2_{M_s,0}$, $I^2_{M_f,0}$, $I^2_{A_s,0}$, $I^2_{A_f,0}$ are the "transition square currents" at zero stress.

Transition square currents depends on stress, according to the following linear expressions:

$$I^2_{M_s} = I^2_{M_s,0} + \frac{\sigma}{C_{M,I}} \tag{4.4a}$$

$$I^2_{A_s} = I^2_{A_s,0} + \frac{\sigma}{C_{A,I}} \tag{4.4b}$$

$$I^2_{M_f} = I^2_{M_f,0} + \frac{\sigma}{C_{M,I}} \tag{4.4c}$$

$$I^2_{A_f} = I^2_{A_f,0} + \frac{\sigma}{C_{A,I}} \tag{4.4d}$$

The objectives of the characterization is to evaluate the strain capabilities of the wires and the maximum residual strain, the Young's moduli and all the parameters mentioned before in order to be able to simulate the behaviour of the wires with the only inaccuracy that the transition currents will be different if the external conditions are changed.
In tab. 4.1 and fig. 4.5 the information about the wire from the data sheet are reported [8]. Since wires with different diameters were available (from 25 to 500μm) from the same supplier, we chose those with a nominal diameter of 50 μm on the basis of the recommended and maximum force, and because a thin wire means a lower current needed to heat it. The wire with a nominal diameter of 25 μm has been discarded because too thin to be handled efficiently, but could be reconsidered in the future.
In order to achieve all the information we needed, SMA wires have been heated at different constant loads. Firstly, the time response was determined observing the wire strain when signals of different current values were applied. Then, the current has been varied step by step, waiting enough time to reach a stationary temporary before recording the position of the wire. In such a way the strain-current curve could be reconstructed. The strain of the wire was evaluated from its position considering the geometry of the setup. The methods adopted are described in details in the next sections.

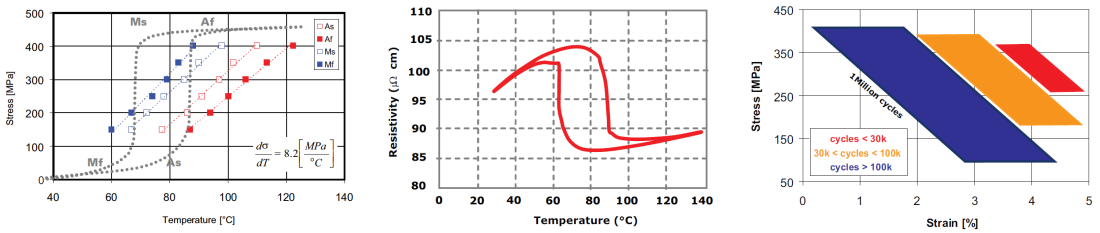

(a) (b) (c)

Figure 4.5: Figures form the data sheet of the used SMA wire [8]. (a) Transformation temperature of a wire loaded of different stress level, (b) Resistivity of the material changing during martensitic transformation, (c) Transformation temperature of a wire loaded of different stress level.

Diameter	Maximum force	Maximum strain	Recommended force	Recommended strain
50 μm	1.2 N (611 MPa)	5%	0.3 N (153 MPa)	3,5 %

Table 4.1: ata about the chosen wire from the datasheet [8] .

4.3 Experimental setup

The aim of this experimental setup is to measure the strain of a SMA wire stressed with a constant load and heated with a certain current. The setup consists of a control circuit capable of delivering a current independently form the load. The circuit is placed into a box on the top of a support column (see fig. 4.6a). The extremities of a SMA wire are hanged to two bushings that protrude out of the circuit. The wire passes through a holed plastic screw (see fig. 4.6b). A load consisting of a cylindrical steel weight with a hole for setscrews on the top is hanged by the plastic screw to the SMA wire as to make it assuming a V shape (see fig. 4.6c). The weight is inserted into a vertical guide in order to not make the wire swinging.
When a sufficient current passes through the wire, this contracts and the load is lifted. Because of the angle between the two sides of the V-shaped wire and the vertical line changes of a very small amount with the wire length, the stress can be considered as constant if the wire is sufficiently long. It is possible to vary the load on the wire by using a different weight. The scheme of this mechanism is reported in fig. 4.6c.

4.3.1 Control circuit

As previously introduced, the SMA wire is hanged to two bushings that protrude from a box containing the driving circuit (see fig. 4.7a). The circuit is powered by a 12 V power supply (V_{CC}) and provides a current that is proportional to an input voltage signal and is independent form the resistance load. The internal scheme of the circuit is shown in fig. 4.7b. In this case the resistance "R_{load}" represents the resistance of the SMA wire. The following equation can be written for the branch of the circuit that goes from V_{CC} to the ground passing by the transistor:

$$V_{CC} = R_{load} I_{max} + V_{drop} + R_5 I_{max} \tag{4.5}$$

where $V_{drop} = 0.7$ V is the voltage drop in the transistor. The maximum current I_{max} that can pass through that branch, and thus, in the SMA wire is:

$$I_{max} = \frac{V_{CC} - V_{drop}}{R_{load} + R_5} \tag{4.6}$$

Therefore, once the length and diameter of the SMA wire are known, R_{load} can be determined and it is possible to calculate the maximum current that the circuit can set as output. V_{CC} can eventually be increased to raise the maximum current, but not too much because the operational amplifier has a limit to its power voltage and would risk to be ruined. Since the resistance of the SMA wire has been measured to be about 4 Ω/cm and that, with the SMA wire in air as in the setup for the characterization, the current needed to complete the transformation to the austenitic phase of the SMA wire was about 85 mA, the length of the wire that we can use is limited to about 25 cm.
The input voltage signal to control the output current was provided by a National Instruments (NI) Multifunctional BUS-Powered DAQ device (USB-6008 [81]) which can be controlled from a laptop by the Matlab software. The NI DAQ has 4 differential and 8 single-ended analogic input channels and 2 analogic output channels. Either the input and the output resolution of the analogic channels is 12 bits. The circuit has been calibrated by changing the driving voltage and measuring the output current with an ammeter. Since the DAQ device has analogic input channels, one of them has been exploited to measure the voltage at the ends of the wire. This link to the NI DAQ device has been verified not to influence the current output. The scheme of the entire control system is shown in fig. 4.8.

(a) (b) (c)

Figure 4.6: (a) Image of the setup system. (b) Image of the plastic screw used to hang the loads to the SMA wires and the needle used to determine the strain. (c) Scheme of the wire actuation system. The SMA wire is connected to two bushings and stressed by a hanging load wich makes it assuming a "V shape". When current is on, the wire heats and contracts pulling up the load.

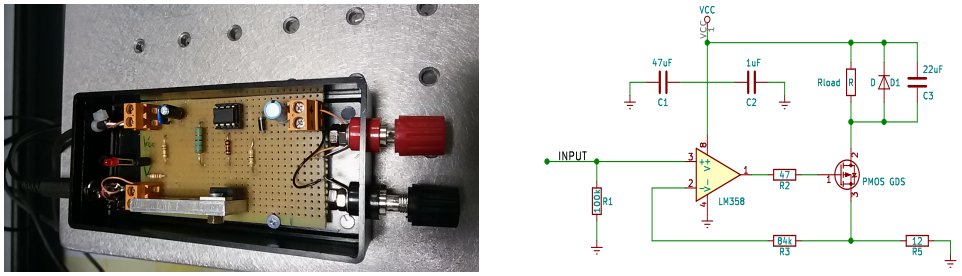

(a) (b)

Figure 4.7: (a)Image of the box containing the driving circuit. (b) Electrical scheme of the driving circuit.

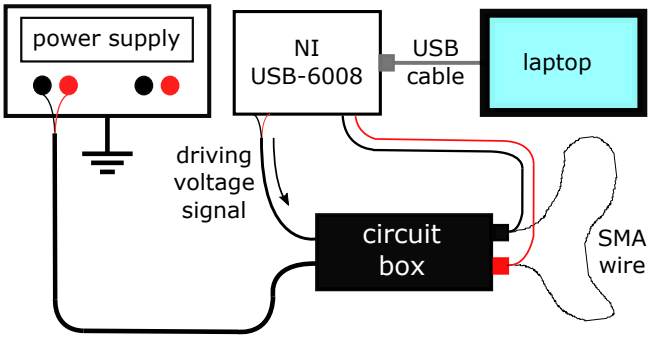

Figure 4.8: Scheme of the control system for the characterization.

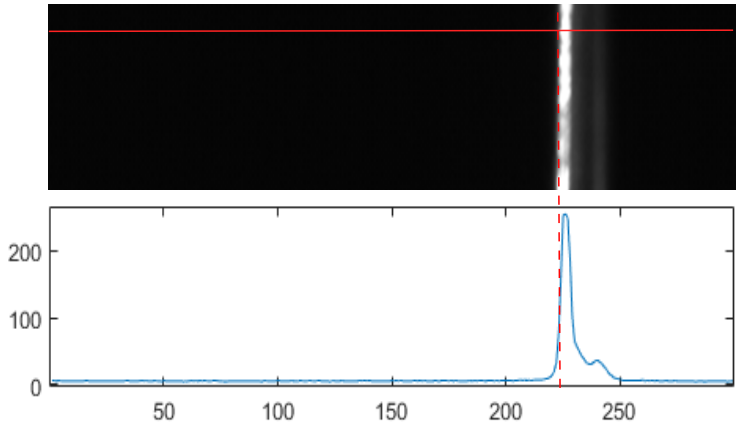

Figure 4.9: Method used to measure the position of the needle. Above: captured image with a portion of the needle. The image is rotated of 90 degrees. Below: intensity profile of the row highlighted with red color in the first image. The dotted red line shows the column that corresponds to the pixel evaluated as position of the needle.

4.3.2 Position measurement

A needle is anchored horizontally to the load (see fig. 4.6b). Through image analysis it is possible to reconstruct the variation of the length of the wire. The pixel correspondent to the needle position was evaluated by fitting the intensity profile of one column of images like that in fig. 4.9 which contains a portion of the needle. The points around the maximum are fitted in groups of five and the third point of the fit with the highest positive slope is considered as the position pixel of the needle. This method was adopted instead of choosing the maximum or a gaussian fit because sometimes there were multiple maxima at the top of the peak. Observing several images it was clear that, while the centre of the peak was not so regular, the correspondence between the zone of maximum slope and the border of the needle was more reliable as an esteem of the position of the needle.
Exploiting the results of an initial calibration using a special target (fig. 4.10), it is possible to calculate the distance Δx travelled by the needle along the vertical axis. If the calculated pixel positions are p_1 and p_2:

$$\Delta x = c(p_2 - p_1) \tag{4.7}$$

where c is the linear coefficient derived from the calibration of fig. 4.10. The calibration has been performed every time the camera position was changed.

4.3.3 Strain calculation

Firstly, we want to calculate the length of the wire without an applied stress. This task however can not be performed directly because the wire curls if no stress is applied. Let us suppose to apply an arbitrary stress to the wire and apply a sufficient current to reach the complete austenitic phase. Referring to fig. 4.11, y is the distance between the bushings, d is the length of the wire inside the plastic screw, l is the length of the wire between a bushing and the plastic screw in the condition described before and x its projection on the vertical axis. The total length of the wire is $L = 2l + d$. And x can be calculated as:

$$x = \sqrt{\left(l\right)^2 - \left(\frac{y-d}{2}\right)^2} \tag{4.8}$$

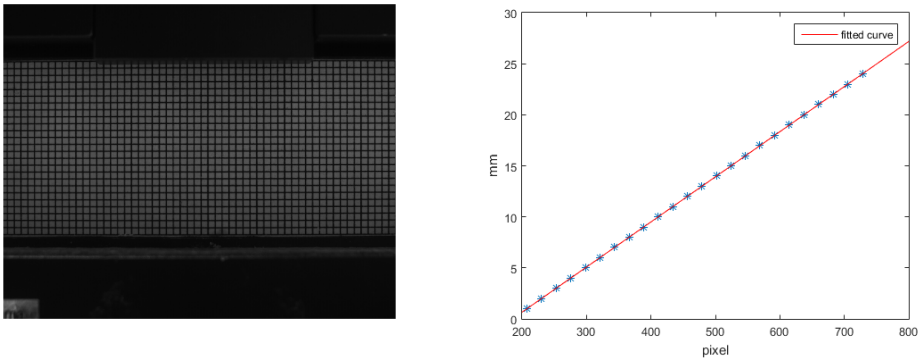

Figure 4.10: Calibration of the correspondence between pixels and distance. On the left there is the special target use for the calibration. On the right the fit of the positions of the black lines in left image and the correspondent pixels. The red line shows the column used for evaluating the position of the black lines.

The total length of the wire when the maximum current is applied increases linearly with stress if we are in the complete austenitic phase:

$$L = L_0 + \frac{L_0}{Y_A}\sigma \tag{4.9}$$

where L_0 is the total length of the wire with no stress applied that we want to calculate. We denote with 0 the correspondent values of l and x. If we consider the angle between the two wire sides and the vertical axis very small, we can do the approximation: $l_0 \simeq x_0$ and $l \simeq x = x_0 + \Delta x$, where Δx is the vertical displacement that we can measure as described in the previous paragraph 4.3.2. Therefore $L = 2l + d \simeq 2x + d$ and $L_0 = 2l_0 + d \simeq 2x_0 + d$. We obtain from eq. 4.9:

$$\Delta x \simeq \frac{L_0}{2Y_A}\sigma \tag{4.10}$$

and recalling eq. 4.7 we find:

$$p \simeq p_0 + \frac{L_0}{2Y_A c}\sigma \tag{4.11}$$

where p_0 is the pixel that corresponds to a total length of the wire L_0 and p to a total length L. Therefore, if we stress the wire with different loads, we can fit the measured pixel positions when the current is maximum for each load value (fig. 4.12). The intercept with the y axis p_0 corresponds to the pixel that we would measure if the wire would not be stressed. We measured the length of the wire sides l' when the current was applied with the minimum load. With this information and by knowing the pixel position p' that corresponds to the position in which we measured l', the length of the wire without an applied stress is:

$$L_0 = 2\sqrt{\left(\frac{y-d}{2}\right)^2 + \Big(x' + c\big(p_0 - p'\big)\Big)^2} + d \tag{4.12}$$

where x' is calculated with eq. 4.8. In such case the quantity $c\big(p_0 - p'\big)$ is negative because L_0 is obviously less than L'.
The strain is defined as $S = \frac{\Delta L}{L_0}$ where $\Delta L = L - L_0$. Since the pixel p_0 correspondent to the length L_0 has been determined, it results:

$$S = \frac{2\sqrt{\left(\frac{y-d}{2}\right)^2 + \Big(x_0 + c\big(p - p_0\big)\Big)^2} + d - L_0}{L_0} \tag{4.13}$$

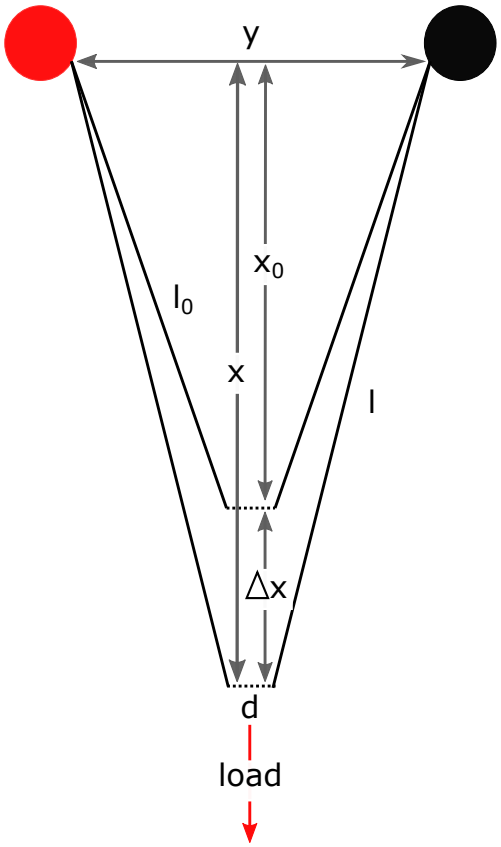

Figure 4.11: Scheme showing the conditions of the wire when a sufficient current to determine the complete transformation in austenite is applied. If no load is applied the wire recovers its original length $L_0 = 2l_0 + d$. Conversely, if a load is applied the wire does not recover completely but a strain proportional to the load remains. In such case the total length of the wire is $L = 2l + d$.

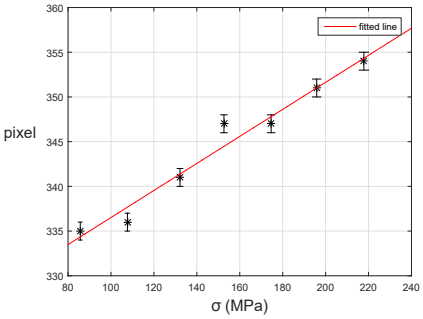

Figure 4.12: Graph showing the linear fit of pixel position as function of the stress applied to a wire with a sufficient current to determine the complete transformation in austenite.

where p is the pixel position found from image analysis.

4.3.4 Measurement of the wire diameter

We measured the diameter of the wire with the *ImageJ* software, analysing the images captured with an optical microscope (objective 10X, fig. 4.13). The software was initially calibrated exploiting a *"1951 USAF resolution test chart"*, then several measurements of the wire diameter were performed. The measurements were taken in different points of the wire to check if there were consistent variations but no one was observed. The mean of the measurements have been considered as the esteem of the diameter and it results in good agreement with the value reported by the data sheet, i.e. $50\mu m$: $D = 50.3 \pm 0.9$.

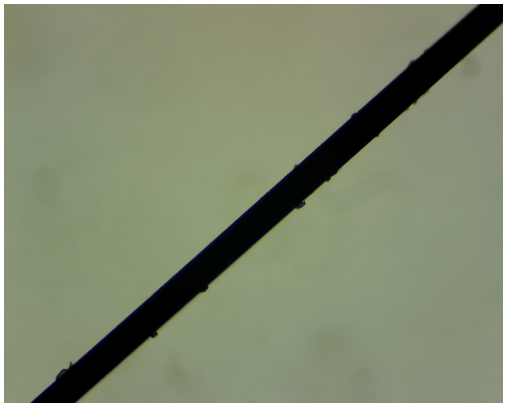

Figure 4.13: Wire image captured with an optical microscope used for determine the wire diameter.

4.4 Time response

The first test that have been performed on the SMA wires consisted in monitoring the evolution of the wire strain in time when current was suddenly increased and when the current was switched off. These measurements have been performed with different wires under several constant loads with different final currents. Images of the needle used to reconstruct the wire strain as explained in section 4.3.2 have been acquired continuously after current was switched on or off and have been time labelled; in such way it was possible to reconstruct the evolution in time of the wire strain.
In tab. 4.2 the stress and current values with which the experiment has been carried on are reported. Higher stress values have not been tried because the guide in which weigths used for stressing the wire during the experiment were not long enough for heavier longer weights. Since the same wire was used for acquisitions with several loads and currents, after each measurement the wire were "reset" by a sufficient current to induced the complete recovery of the strain in the unloaded condition. Furthermore, the adopted loads were used from the lowest to the highest to minimize the impact of possible residual deformations. The ambient temperature was verified to be constant at about 25°C during the different measurements.
In fig. 4.14a the strain evolution in time for the same wire stressed with the highest load for different input currents is shown. In each case the current was maintained high for a sufficient time to let the strain stabilize and then switched off while continuing monitoring the strain. As it can be seen from fig. 4.14a, the strain difference from the moment in which current is switched and the value at which it stabilizes increase with the final current value. In fact, the transformation is complete for the maximum current (100mA) but not for the lower current values, i.e. there still is a fraction of martensite. There was no further recovering for currents above the maximum current.
In fig. 4.14b a comparison between the strain evolution with same load and applied current for two different wires is shown. The strain is slightly different but, considering the highly unideal behaviour of SMAs and that some difference in the stressing could occur, the comparison can be considered good and the experiment repeatable.
Once the current is applied to the wire, the evolution of temperature in time is described by eq. 3.36. The strain begins to change when the temperature of the wire exceeds the initial austenitic temperature A_s and stabilizes once the austenitic finish temperature A_f is reached or overcome. We recall that the time employed by the temperature to stabilize when cooling or heating is the same, but since the transformation temperatures are not equal the strain behaves differently. This can be seen in fig. 3.5 in which simulated temperature and strain evolutions in time are shown. Since transformation temperatures change with the applied stress, we expect that also the response time change accordingly.
In the light of these considerations, we evaluated the response time and studied its behaviour with respect to the applied stress and current applied to the wire. Then we exploited the data to calculate the possible strain variation ΔS and maximum strain S_{max} of the wire under a certain stress and to esteem the Young's moduli in the austenitic and martensitic phases and the maximum residual strain S_{res}.

Stresses	85 MPa	107 MPa	131 MPa	151 MPa	173 MPa	194 MPa	216 MPa
Currents	70 mA		80 mA		90 mA		100 mA

Table 4.2: Current and stress values for the velocity test.

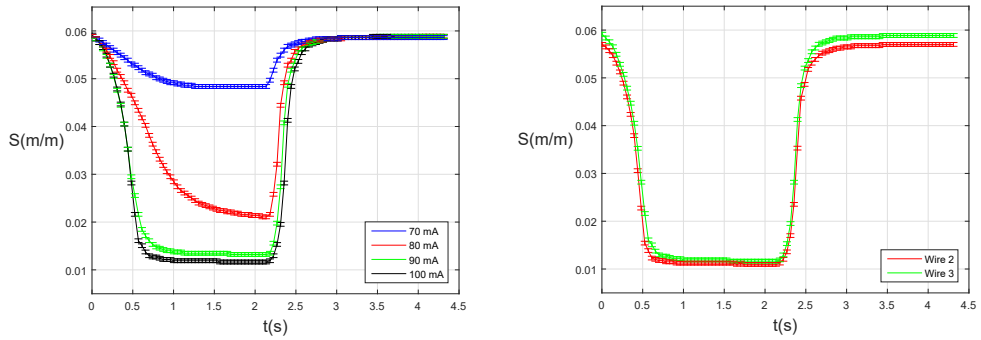

(a) (b)

Figure 4.14: (a) Strain evolution in time when different currents (70mA, 80mA, 90mA, 100mA) are applied to a SMA wire under constant load ($\sim$ 216 MPa). (b) Comparison between strain evolution in time for two different wires with same applied current (100 mA) under the same stress ($\sim$ 216 MPa).

4.4.1 Response time

We define the "rise time" as the time that the strain employs, when the SMA wire is heated, to go from the 90% to the 10% of the curve:

$$t_{rise} = t_{10\%} - t_{90\%} \text{ when heating} \tag{4.14}$$

(4.15)

We define in an analogous way the "fall time" as the time that the strain employs, when the wire is cooling, to go from the 10% to the 90% of the curve:

$$t_{fall} = t_{90\%} - t_{10\%} \text{ when cooling} \tag{4.16}$$

The rise and fall time are en esteem of the response time of the wire when heating and cooling respectively. A graphic representation of the method employed to calculate them is reported in fig. 4.15.
The mean of the times that elapsed between two consecutive image acquisitions has been considered as the error on time esteems

$$\sigma_{time} = \frac{\sum_{i=1}^{N-1} \left(t_i + 1 - t_i\right)}{N-2} \tag{4.17}$$

where N is the number of images and t_i the times of acquisition of each image. This time corresponds to that required on average for image acquisition and saving. Therefore, the error on the rise and fall time is:

$$\sigma_{rise,fall} = \sqrt{2}\sigma_{time} \tag{4.18}$$

We want to understand how the rise and fall time depends on stress and the heating current. To determine the expected behaviour we have to recall the solution of the *Joule's heating equation* from chapter 3 that describes the evolution of the temperature in time when the wire is heated with a current i:

$$T(t) - T_\infty = \frac{R}{h_c A_c}\left(1 - e^{-\frac{t}{t_h}}\right) i^2 + \left(T_0 - T_\infty\right) e^{-\frac{t}{t_h}} \tag{4.19}$$

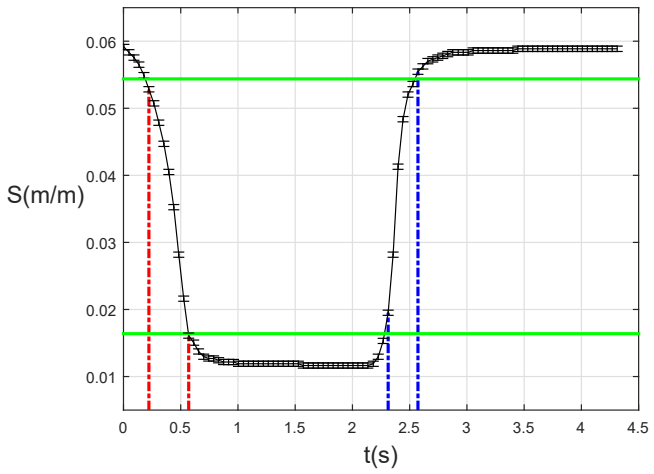

Figure 4.15: Graph showing the strain evolution in time. Continuous green lines corresponds to the 90% and 10% of the strain curve. The acquisition times of the first images that presented a strain lower(red dashed lines)/higher(blue dashed lines) than the 90% and 10% of the strain difference have been considered to calculate the rise/fall times.

As stated by eq. 4.19 and assuming an initial temperature T_0 equal to the ambient temperature T_∞, the temperature of a wire increases as $1 - e^{t/t_h}$ when it is heated with a current i. This implies that the more the temperature approaches the final value (ideally an asymptote), the slower it grows. Let us suppose to heat the wire at different stress values and that the current is sufficient to reach the complete austenitic phase. The strain changes only when temperature is between the austenitic transition temperatures and increasing the stress means increasing the austenitic transition temperatures. This means that the higher the stress of the wire, the higher the time that the strain takes to go from the initial to the final value. If the current is not sufficient to complete the transformation the strain will continue changing with temperature until it will stabilize. Therefore we expect the rise time to increase with the applied stress if the wire is heated with a sufficient current to start the phase transition and then the strain recovery. Since the temperature decreases when cooling, we expect the fall time to decrease with stress on the contrary of the rise time.
Let us suppose to heat a wire with two different currents i_L and i_H at the same stress value such that:

$$i_L < i_H \tag{4.20}$$

If the heating current is i_H, we define t_1^H and t_2^H the times at which the temperature is equal to the start and finish austenitc transformation temperatures respectively, t_1^L and t_2^L when the current is i_L. Considering eq. 4.19 and that the start temperature is $T_0 = T_\infty$ in both cases, we can write:

$$T(t_2^H) - T(t_1^H) = \frac{R}{h_c A_c}\left(e^{-\frac{t_1^H}{t_h}} - e^{-\frac{t_2^H}{t_h}}\right) i_H^2 \tag{4.21}$$

$$T(t_2^L) - T(t_1^L) = \frac{R}{h_c A_c}\left(e^{-\frac{t_1^L}{t_h}} - e^{-\frac{t_2^L}{t_h}}\right) i_L^2 \tag{4.22}$$

Since the stress is the same in the two cases, the transformation temperatures remain the same too. Therefore:

$$\left(e^{-\frac{t_1^H}{t_h}} - e^{-\frac{t_2^H}{t_h}}\right) i_H^2 = \left(e^{-\frac{t_1^L}{t_h}} - e^{-\frac{t_2^L}{t_h}}\right) i_L^2 \tag{4.23}$$

t_1^L and t_1^H are defined such that the temperature in the two cases we are considering is the same. This condition is satisfied if the following relationship, obtained from 4.19, is valid:

$$\frac{i_H^2}{i_L^2} = \frac{1 - e^{-\frac{t_2^L}{t_h}}}{1 - e^{-\frac{t_2^H}{t_h}}} \tag{4.24}$$

If we define as $\Delta t_{H,L} = t_2^{H,L} - t_1^{H,L}$ the time that the temperature of the wire takes to go from the start austenitic temperature to the finish austenitic temperature, i.e. the time in which the strain changes. Then eq. 4.23 becomes:

$$\frac{e^{\frac{t_1^L}{t_h}} - 1}{e^{\frac{t_1^H}{t_h}} - 1} = \frac{1 - e^{\frac{\Delta t_H}{t_h}}}{1 - e^{\frac{\Delta t_H}{t_h}}} \tag{4.25}$$

Since $t_1^H < t_1^L$, the left term of eq. 4.25 is lesse than one. Applying the same inequality to the rigth term we derive:

$$\Delta t_L > \Delta t_H \tag{4.26}$$

Therefore we expect to find the rise times increasing as the heating current decrease, at least until the current is sufficient to induce a strain change, i.e. to reach a temperature above the start austenitic temperature. Otherwise, the strain remains stable (neglecting thermal expansion). Let us suppose to let the wire cool down. The situation is quite different. The evolution of temperature is:

$$T(t) = (T_0 - T_\infty)e^{\frac{t}{t_h}} \tag{4.27}$$

If we consider the two cases before, the initial temperatures are different:

$$T_0^H = \frac{R}{h_c A_c} i_H^2 + T_\infty \qquad\qquad T_0^L = \frac{R}{h_c A_c} i_L^2 + T_\infty \tag{4.28}$$

We define t_3^H and t_4^H the times at which the temperature is equal to the start and finish martensitic transformation temperatures when the heating current has been i_H, t_3^L and t_4^L when it has been i_L. With analogous considerations to the heating case we can write:

$$\left(e^{-\frac{t_4^H}{t_h}} - e^{-\frac{t_3^H}{t_h}}\right) i_H^2 = \left(e^{-\frac{t_4^L}{t_h}} - e^{-\frac{t_3^L}{t_h}}\right) i_L^2 \tag{4.29}$$

Likewise to the heating case, t_3^L and t_3^H are such defined that the temperature in the high current and low current cases is the same. This condition is now satisfied if the following relationship, that is different from the heating case (eq. 4.24), is valid:

$$\frac{i_H^2}{i_L^2} = \frac{e^{-\frac{t_2^L}{t_h}}}{e^{-\frac{t_2^H}{t_h}}} \tag{4.30}$$

If we define $\Delta t'_{H,L} = t_4^{H,L} - t_3^{H,L}$, from eq. 4.29 and 4.30 we obtain:

$$\left(e^{-\frac{\Delta t'_H}{t_h}} - 1\right) = \left(e^{-\frac{\Delta t'_L}{t_h}} - 1\right) \tag{4.31}$$

Therefore:

$$\Delta t'_H = \Delta t'_L \tag{4.32}$$

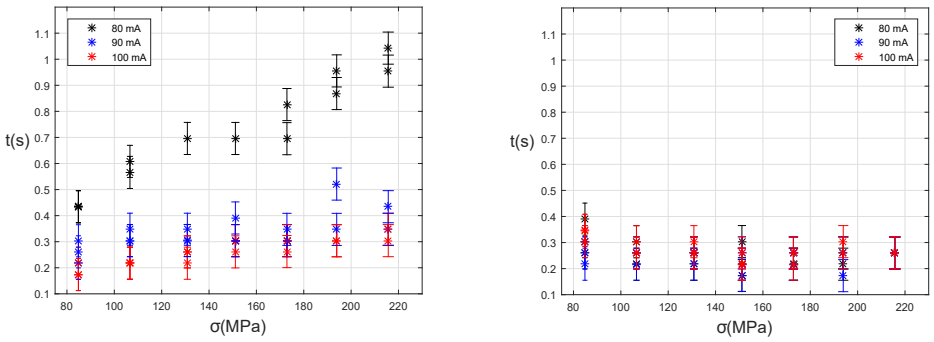

(a) (b)

Figure 4.16: (a) Rise time as a function of stress with different heating current. (b) Fall time as a function of stress with different heating current.

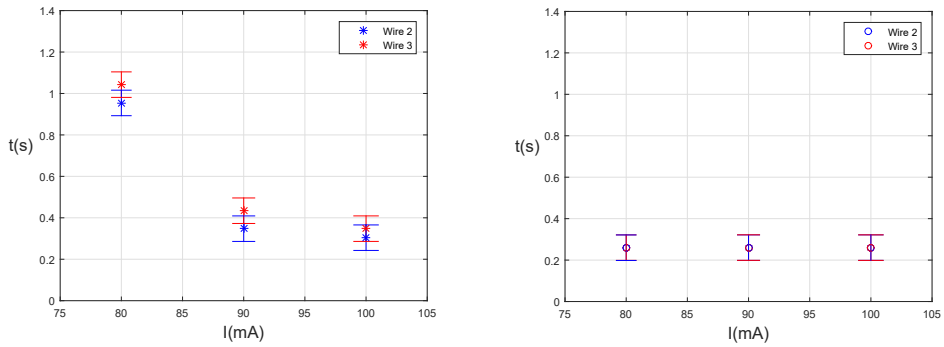

(a) (b)

Figure 4.17: (a) Rise time as a function of the applied current for wires stressed at about 216 MPa. (b) Fall time as a function of the applied current for wires stressed at about 216 MPa.

Differently from the heating case we expect the fall time not to depend on the current with which the wire has been heated.
The experimental rise and fall time as functions of stress are reported in fig. 4.16. Rise time increases with stress for all currents as expected. The slope is higher for lower currents because in these case the transformation is not complete and the strain continues to change until temperature stabilizes.
We can not confirm the expected decrease of the fall time with the applied stress. The fall time seems to remain constant, at least, inside the error. Measurements with a higher time resolution are needed to determine better the fall time behaviour.
The rise and fall time with respect to the applied current are shown in fig. 4.17 for wires stressed at about 216 MPa. The same behaviour is confirmed at lower stresses. As expected, the rise time increases when the current decreases while the fall time remains constant.

4.4.2 Young's moduli and maximum residual strain

The Young's moduli in the two phases and the maximum residual strain are essential to carry out a simulation of the SMA wires since these are parameters that appear in the constitutive

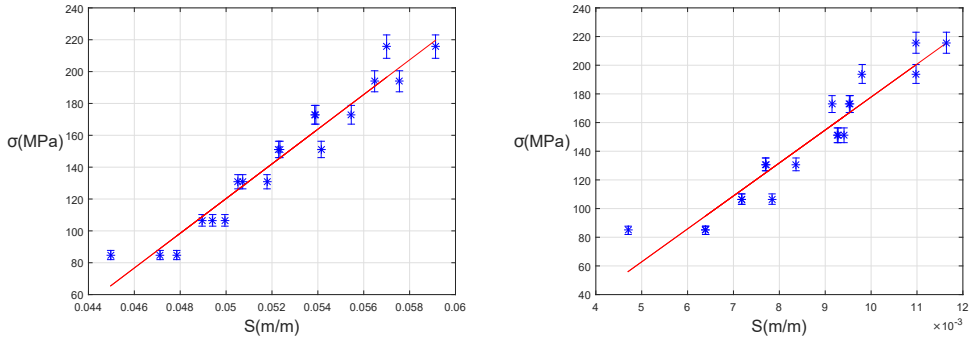

(a) Strain in the martensitic phase as function of stress. The angular coefficient of the linear fit represents the Young's modulus in the martensitic phase Y_m.

(b) Strain in the austenitic phase as function of stress. The angular coefficient of the linear fit represents the Young's modulus in the austenitic phase Y_a.

Figure 4.18

law 3.25 that governs the relationship between stress, strain and the phase of the SMA wire:

$$\sigma - \sigma_0 = Y(\xi)S - Y(\xi_0)S_0 - S_L\big(Y(\xi)\xi_S - Y(\xi_0)\xi_{S,0}\big) \tag{4.33}$$

where S_L is the maximum residual strain and:

$$Y(\xi) = Y_a + \big(Y_m - Y_a\big)\xi \tag{4.34}$$

Y_m is the Young's modulus in the martensitic phase and Y_a in the austenitic one.
When current is off, the wire is in the complete martensitic phase. In such condition $\xi = \xi_S = 1$, then the constitutive law 4.33 becomes:

$$\sigma = Y_m S - S_L Y_m \tag{4.35}$$

Therefore, from the linear fit of the stress as a function of the the maximum strain, it is possible to calculate Y_m and S_L. In fig. 4.18a the linear fit of strain data measured with different wires is shown. If m and q are the two parameters of the fit such that $\sigma = mS_{max} + q$, then:

$$Y_m = m \tag{4.36}$$

$$S_L = -\frac{q}{m} \tag{4.37}$$

When applying a sufficient current to make the wire completely austenitic, the constitutive law is:

$$\sigma = Y_a S \tag{4.38}$$

Then, from the linear fit in fig. 4.18b where the strain values after the recovery are reported, it is possible to esteem Y_a as the angular coefficient of the fit.
From the calculations above the results are:

$$Y_m = 10.9 \pm 0.6 \text{ GPa} \tag{4.39}$$

$$Y_a = 22.9 \pm 1.8 \text{ GPa} \tag{4.40}$$

$$S_L = 0.0389 \pm 0.0008 \text{m/m} \tag{4.41}$$

The error on the maximum residual strain has been calculated considering the not null covariance between the esteemed parameters q and m.

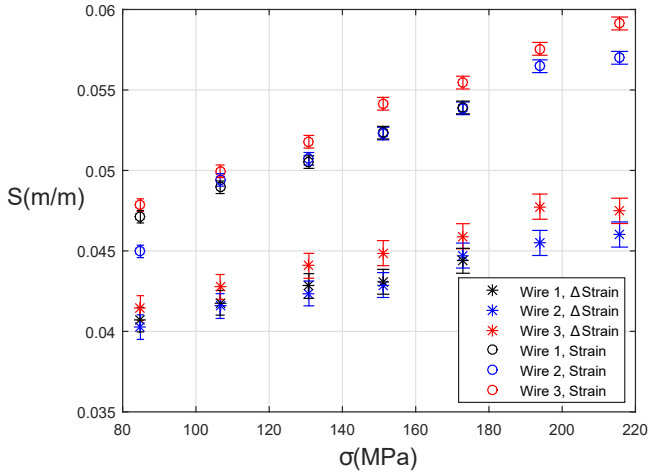

Figure 4.19: Maximum strain and strain difference between the austenitic and martensitic phases as function of stress.

4.4.3 Maximum strain and strain variation

One of the objectives of the characterization is to determine the dependence on stress of the maximum strain S_{max} and the strain variation ΔS, i.e. how much strain the wire is capable to recover when heated. The strain of the wire before switching current on has been considered as S_{max}, while the difference between S_{max} and the strain value at which the wire stabilizes after the current has been applied has been considered as ΔS. Both S_{max} and ΔS are plotted as functions of stress in fig. 4.19.
As expected, the maximum strain increases with the applied stress. With the maximum stress applied of about 216 MPa, a strain of 0.06 is reached. Since we are quite below the maximum stress suggested, with a higher stress it would be possible to reach higher strains depending on the Young's modulus of the martensitic phase.
Also ΔS is found to increase with stress. Indeed, the Young's modulus in the austenitic phase is lower than that in the martensitic one, i.e. the strain of the wire in the martensitic phase increases more than in the austenitic phase. Therefore the difference between them increases.

4.5 Cycling measurements

As mentioned before in section 4.1, the strain curve as a function of temperature under constant stress can be exploited to obtain the transition temperatures. Since we did not measured the wire temperature, we performed a similar test referring to the applied current.
We analysed the strain curve as function of the applied current, varying it step by step from zero to a value sufficient to transform the wire in complete austenite and *vice versa*. The strain of the wire was measured for each current value waiting enough time to consider the current as steady. These measurements have been realized with two different wires under several constant loads (the same employed for the rise and fall time estimates). Furthermore, for each step the voltage drop at the wire extremes has been measured in order to calculate the resistivity of the wire.
In fig. 4.20a the strain curves of one wire for all the applied loads are reported. When current is increased, the strain remains constant until the temperature reaches the austenitic start temperature A_s, then it begins to decrease up to the austenitic finish temperature A_f. When current

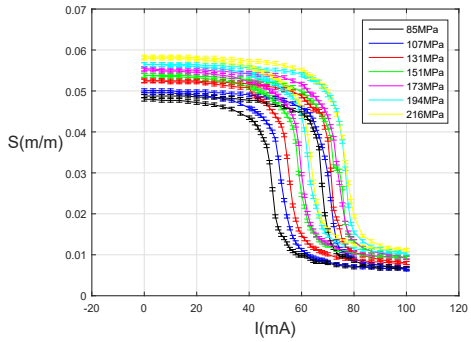

(a) Strain of one wire as function of the applied current for different applied constant stresses.

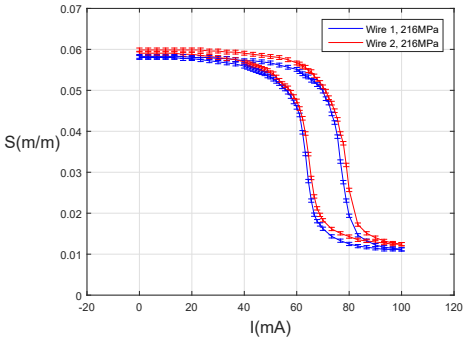

(b) Strain curves of two wires under the same applied load ($\sim$ 216 MPa) as function of the applied current.

Figure 4.20

decreases, the strain remains constant at temperature above the martensitic start temperature M_s, then is starts to increase and stops when the temperature decreases below the martensitic finish temperature M_f.
The maximum and minimum strain, correspondent to the complete martensitic and austenitic phase respectively, increase linearly with stress. The minimum stress increases less than the maximum one, confirming that the Young's modulus in the austenitic phase is lower.
In fig. 4.20b the strain curves with the same applied load for the two wires are reported, showing a good compatibility of the measurements and therefore their repeatability. The data acquired with these measurements have been exploited:

- To provide further estimates of the Young's moduli and the maximum residual strain to be compared with the previous ones.
- To calculate the transition currents as functions of stress and the stress influence coefficients that define the relationship between stress and the transition square currents.
- To analyse the behaviour of the resistivity of the SMA wire.

4.5.1 Young's moduli and maximum residual strain

The Young's moduli Y_m and Y_a have been calculated as done in the paragraph 4.4.2. The values obtained are:

$$Y_m = 11.2 \pm 0.9 \text{ GPa} \tag{4.42}$$
$$Y_a = 20.3 \pm 2.5 \text{ GPa} \tag{4.43}$$
$$S_L = 0.0403 \pm 0.0011 \text{m/m} \tag{4.44}$$

The compatibilities with the values at 4.41 are good (< 1):

$$c(Y_m) = 0.3 \tag{4.45}$$
$$c(Y_a) = 0.9 \tag{4.46}$$
$$c(S_L) = 1.1 \tag{4.47}$$

Therefore, the average with the previously obtained values have been considered as final esteems.

$$Y_m = 11.03 \pm 0.05 \text{ GPa} \tag{4.48}$$
$$Y_a = 21.66 \pm 0.15 \text{ GPa} \tag{4.49}$$
$$S_L = 0.0397 \pm 0.0007 \text{m/m} \tag{4.50}$$

4.5.2 Transition currents and stress influence coefficients

As stated in the paragraph 4.2, we did not try to esteem the transition temperatures but just the correspondent transition currents. The method used to obtain the transition currents is outlined in fig. 4.21a. The strain curve has been linearly fitted where it varies the most, i.e. when current is between the two transition currents (between I_{A_s} and I_{A_f} when current is increasing, between I_{M_s} and I_{M_f} when current is decreasing). The intercepts of these two lines with the horizontal lines correspondent to the maximum and minimum strain have been considered as the transition currents.
The strain is not strictly constant outside the intervals defined by the transition currents, as can be clearly seen in fig. 4.21a. This is due to the not null coefficient of thermal expansion (which is different in the austenitic and martensitic phase). When the wire temperature is known, it is possible to esteem the coefficients by fitting linearly the strain curve below M_s when heating and above A_s when cooling down. In the absence of this behaviour it could have been possible to esteem the transition currents by considering the current values at which the strain starts to change, but, since the strain change is also due to the thermal effect and not only to the phase transition, the method described above has been adopted.
Once the transition currents are deduced for each stress and wire, and considering that the square current is proportional to the temperature, the parameters of eq. 4.4d can be obtained by linearly fitting the stresses at which the measurements were performed as function of the four square transition currents. In fig. 4.21b the linear fits correspondent to the four lines described by eq. 4.4d are shown. A phase diagram is reproduced with the square current instead of temperature.
We unavoidably found different coefficients for each transition current from the fits in fig. 4.21b, while the "stress influence coefficients" considered in eq. 4.4d are two: one for the martensitic transition currents and one for the austenitic ones. We considered separately as the mean of the coefficients concerning the martensitic transition currents and the austenitic ones as their esteems . The results are:

$$C_{M,I} = 73 \pm 4 \; GPa/A^2 \tag{4.51}$$
$$C_{A,I} = 93 \pm 7 \; GPa/A^2 \tag{4.52}$$

The transition currents at zero stress are calculated as the square root of the intercept of the fitted lines with the x axis:

$$I_{M_f,0} = 0.031 \pm 0.002 \tag{4.53}$$
$$I_{M_s,0} = 0.040 \pm 0.002 \tag{4.54}$$
$$I_{A_s,0} = 0.057 \pm 0.001 \tag{4.55}$$
$$I_{A_f,0} = 0.063 \pm 0.002 \tag{4.56}$$

4.5.3 Resistivity

As previously seen in chapter 3, the resistivity of SMA wires presents an hysteresis when the wire is heated and cooled because it is related to the phase of the alloy. The hysteresis path depends also on how much the wire is stressed. The voltage drop on the SMA wire has been

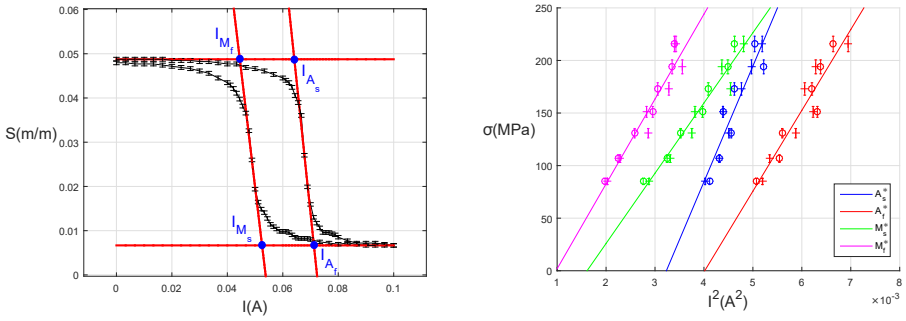

(a) (b)

Figure 4.21: (a) Strain curve as function of the current applied to a wire under a stress of ~ 85 MPa. The horizontal lines correspond to the maximum and minimum strain. The oblique lines are obtained by partially fitting the strain curve. The intercepts between the oblique and horizontal lines (blue dots) are considered as the transition currents. (b) Stress of the wires as function of correspondent transition currents. The points concerning the same transition current at different stresses and for each wire have been fitted to determine the "stress influence parameters" and the transition currents at zero stress.

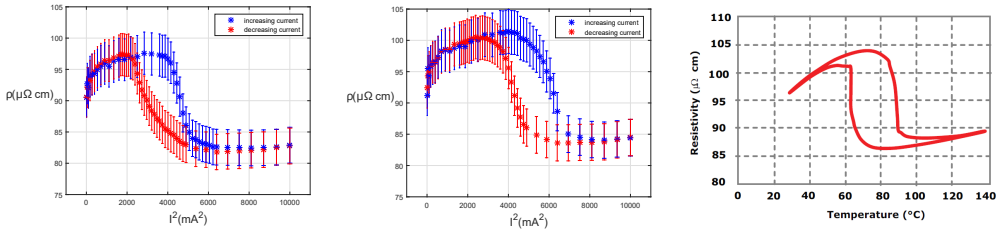

(a) (b) (c)

Figure 4.22: (a) Resistivity as a function of the square current applied to a SMA wire stressed at about 85 MPa (a) and 216 MPa (b). (c) Graphic of the resistivity behaviour with temperature from the wire datasheet [8].

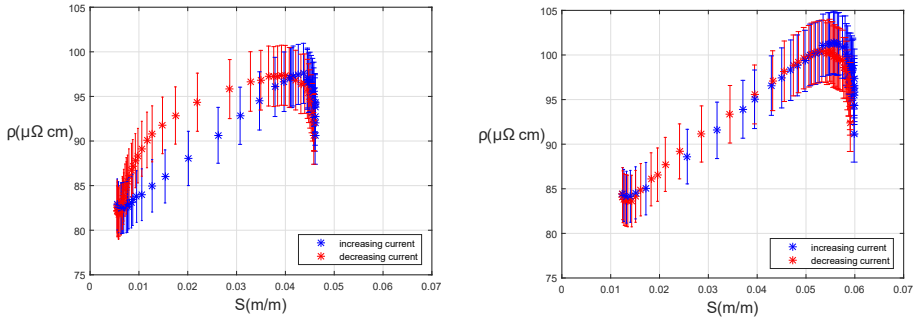

(a) (b)

Figure 4.23: Resistivity of a SMA wire stressed at 85 MPa (a) and at 216 MPa (b) as a function of strain. Data corresponding to the heating phase are highlighted in blue, to the cooling phase in red.

measured and, by knowing the current and the wire length and diameter, the resistivity has been calculated.
In fig. 4.22 the measured resistivity as function of the square current, i.e. a quantity proportional to temperature, is compared to the graph of the resistivity as function of temperature from the data sheet of the wire (see fig. 4.22c). The graph in fig. 4.22a and 4.22b represent the resistivity measured with the lowest and highest loads used respectively. In the latter case the resistivity path resembles that from the data sheet (the graph can be compared because the square current is proportional to temperature) while in the former case the path is slightly different when the SMA wire cools down (red data). Unfortunately, the stress of the wire is not specified in the data sheet but the resistivity value is compatible with the measured one. The graph concerning the measurements with intermediate loads show a slight change from the path in fig. 4.22a to that in fig. 4.22b.
If the resistivity of the previous graph is plotted against the strain of the wire as in fig. 4.23, the resistivity presents an hysteresis in the case of the lowest load but presents a linear and univocal relationship with he strain in a certain interval in the case of the highest load. Again, for intermediate loads the path slightly varies from the former to the latter case.

4.6 Comments on the characterization results

We built an experimental setup for the characterization of the SMA wire, i.e. to determine those parameters needed to perform a simulation on the basis of the model described in section 4.2 (Young's moduli, maximum residual strain, transition currents at zero stress and stress influence coefficients on transition currents) and to esteem the performance of the SMA wire (maximum strain and current needed to an efficient use of the wires). Furthermore, the behaviour of the resistivity has been analysed as function of current and strain because of its possible use as feedback parameter in a control system for the SMA wires.
We measured the time response of the SMA wires to the application of a certain current and then when cooling down. The wire temperature, as stated by the solution of the Joule's equation of heating eq. 4.19, depends on the external conditions (heat flow coeffcient h_c) and on the diameter of the wire. We are interested in the strain response that depends on that of the temperature, the applied current and stress, as explained in paragraph 4.4.1. The aim of these measurements is to determine a first esteem of the response time and to verify the behaviour of the response time with the stress and current applied to the wire with the awareness that a further analysis will be necessary when the wire will be implemented in a device.
The expected behaviour has been confirmed by experimental data, with the exception of the response time behaviour with respect to the applied stress when cooling. This seems to remain constant as the stress is changed on the contrary of the expected decrease. A higher time resolution is probably requested to observe it.
When the wires are heated, their response time decreases with the applied current. As stated in section 3.2, the response time can be lowered by using the maximum current to heat the wire whatever the desired strain is and then adjusting it when it is reached. The time response with the maximum current for a complete strain recovery is about 0.3 s.
We measured the strain while varying the current "step by step" from zero to a sufficient value to induce a complete transformation of the wire and then *vice versa*. Repeating this procedure at different stresses, it was possible to determine all the parameters of the model described in section 4.2 as the transition currents at zero stress and the stress influence coefficients concerning the transition currents. These parameters are needed to carry on a simulation of the SMA wire.
The stress influence coefficients found in literature [2] concern the relationship between the transition temperatures and strain. Therefore, it is necessary to multiply the calculated coefficients by the proportionality constant between current and temperature. Since this constant depends on the heat flow coefficient h_c that we do not know, we used a value from literature, $h_c = 140$

J/(s m^2 °C) [2]. A unique coefficient $C = 8.2$ MPa/°C for the austenitic and martensitic temperatures is reported in the wire data sheet. We obtain the correspondent coefficient with respect to the square current as $C' = C\frac{\rho}{2\pi^2 r^3 h_c}$, where $\rho \simeq 90\mu\Omega \cdot cm$ is the average wire resistivity and r the wire radius. It results $C' = 170$ GPa/A^2. The experimental coefficients are both lower than the expected value. This can be due to the fact that the actual value of h_c is lower than that found in literature.
The Young's moduli in the austenitic and martensitic phase and the maximum residual strain were esteemed from data. The experimental values, $Y_m^{exp} = 11.03 \pm 0.05$ GPa, $Y_a^{exp} = 21.66 \pm 0.15$ GPa and $S_L = 0.0397 \pm 0.0007$ m/m, are lower than the expected values found in literature ([2]), $Y_m^{th} \simeq 20$ GPa, $Y_a^{th} \simeq 60$ GPa and $S_L = 0.06$ m/m.
As expected, the behaviour of resistivity varies with the applied stress. Only with a sufficient stress (> 200 MPa) the relation between resistivity and strain is linear and therefore, it could be used as feedback parameter in a control system. This means that, if we want to control the wire through resistivity, we will have a lower stress limit when designing the device.

Chapter 5

Prototype test

The objective of this project is to realize a deformable lens based on SMA wires. The design of such a lens is based on two thin glass sheets, among which there is a transparent gel, that are bent using SMA wires. In this chapter the realization of a prototype lens of this type is discussed.
Let us consider a rectangular thin glass sheet under which two pins are placed in the middle of the long side. Let us suppose to bend symmetrically the glass using two SMA wires that hook the glass at the extremities of the long side and to fix the wires in that position. If the SMA wires have been sufficiently stressed, they are in the complete stressed induced martensitic phase and have undergone the consequent elongation. The glass curvature will depend on the stress applied to the wires and on the dimensions and properties of the glass. Let us now suppose to heat the wires by Joule effect using the same current. If the current is sufficient, they start to transform to the austenitic phase and to recover the previous elongation, hence further bending the glass. The system behaviour is similar to that in which the SMA wire is bounded to a bias spring whose elastic constant now depends on the elastic modulus of the glass and its dimensions. Provided that a deformable, transparent material with a refractive index higher than that of air is placed beneath the glass, this system acts as a converging lens, although only along the sagittal plane, i.e. the rays are focussed only along one direction and a circular optical beam is focussed on a line instead of a point. Let us now suppose to bend another glass in the perpendicular direction to that along which we bent the first glass as represented in fig. 5.1b and that the material inside the glasses has the same refractive index of the glass. Each glass contributes to the focusing of rays which belong to planes that are parallel to the direction along which each of them is bent. The contemporary action of the two glasses makes the device behave as a biconvex lens, hence focusing the incoming light into a spot. Since we are able to change the curvature of the glasses by heating or cooling the wires, we obtain a lens with a variable focal length.
Before realizing a prototype of deformable lens, we firstly built a glass cantilever as that in fig. 5.1c and studied its response when bent with a SMA wire, comparing the experimental results with those obtained from a simulation carried out employing the parameters determined with the characterization (see previous chapter).
We then built and characterized a complete device that has been used to provide a first practical demonstration of the feasibility of this project.

5.1 Simulation of the prototypes

We carried out a simulation of the devices that we would have built in order to determine an esteem of the glass displacement depending on its dimensions and the initial conditions and compare it with the experimental results.
The simulation has been carried out considering the theoretical model for the SMA behaviour

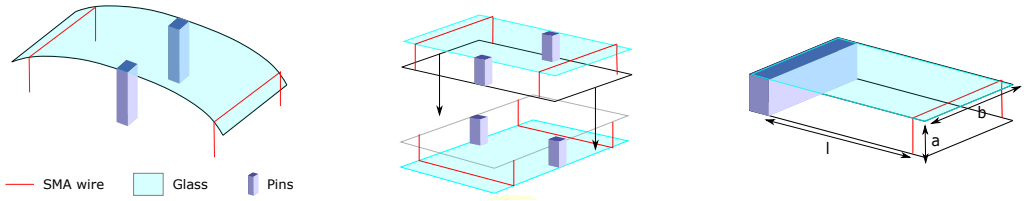

(a) (b) (c)

Figure 5.1: (a) Scheme of the bending system of one glass (light blue) on two central pins along the long sides by employing SMA wires (red lines). (b) Scheme of the structure of a lens with variable focal length. The lens is composed by two glasses on two central pins along the long sides of the glass and bent along orthogonal directions by two SMA wires each. Between the two glasses there is an elastomeric material with the refractive index of glass. (c) Scheme of the structure of a glass cantilever as it was realised. The cantilever is bent by a SMA wire that hooks the glass at a distance l from the fixed extreme of the glass. The SMA wire drops perpendicularly from the glass sides and its extremities are fixed at a distance a from the height defined by the glass when it is in the horizontal position. The width of the glass is defined as b.

described in chapter 3 and already adopted to simulate the SMA wires. The glass behaviour has been determined considering the linear theory of elasticity which provides a method of calculating the deflection characteristics of beams. An approximated focal length has been calculated as esteem of the device performance exploiting elements of geometrical optics.
Let us consider a thin glass on a central pin, symmetrically bent by two prestressed SMA wires at its extremes (see fig. 5.1a). First of all, we determined the relationship between the glass curvature and the stress of the SMA wire. Considering the wire position around the glass, it is clear that the force applied on the glass is double with that applied to the wire. The glass has been considered as a beam of section $A = bh$ and length $2l$, where b and h are the glass width and height respectively. We define the x axis as that perpendicular to the beam section so that the $x = 0$ position coincides with the center of the glass length as in fig. 5.2a (where only half of the glass profile is shown).
The equations that govern the shear force and the bending moment along the beam are:

$$\frac{dF}{dx} = -q \tag{5.1}$$

$$\frac{dM}{dx} = -T \tag{5.2}$$

where q is the load (force per unit length) applied on the beam. Ignoring the load due to the glass weight ($q = 0$), the shear stress and bending moment results:

$$F = -P\ , \quad M = -P(x + l)\ , \quad \text{when } x < 0 \tag{5.3}$$

$$F = P\ , \quad M = P(x - l)\ , \quad \text{when } x > 0 \tag{5.4}$$

where P is the force with which the glass is pushed down. The differential equation of linear elasticity that describes little deformations of a beam under a bending moment is:

$$EJ\frac{d^2y}{dx^2} = -M \tag{5.5}$$

where E is the elastic modulus of the beam (in our case of glass) and J is the second moment of area with respect to the neutral axis:

$$J = \frac{bh^3}{12} \tag{5.6}$$

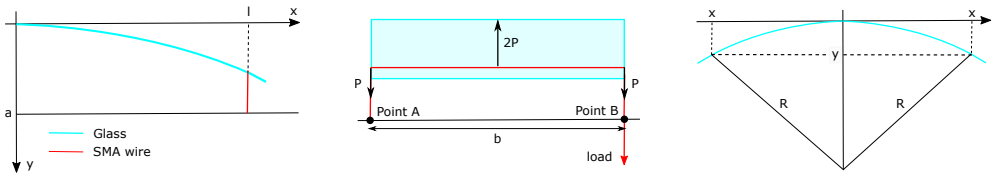

(a) (b) (c)

Figure 5.2: (a) Frame of reference and curvature of the cantilever glass under the stress of the SMA wire. (b) Side view of the cantilever bent by the SMA wire. P is the tension of the wire, while the glass is subjected to a double force equal to 2P. (c) Curvature of the glass in a central pin and bent by two forces at its extremities. The curvature is here approximated to an arc of a circle.

Eq. 5.5 can be solved by integration with the initial conditions $\frac{dy}{dx}(0) = 0$ and $y(0) = 0$. It results:

$$EJ\frac{dy}{dx} = Plx + P\frac{x^2}{2}\ , \quad \text{when } x < 0 \tag{5.7}$$

$$EJ\frac{dy}{dx} = Plx - P\frac{x^2}{2}\ , \quad \text{when } x > 0 \tag{5.8}$$

$$EJy = Pl\frac{x^2}{2} - P\frac{|x|^3}{6} \tag{5.9}$$

Considering a cantilever stressed at a distance l from the fixed extreme and a beam with a constant section (J = constant), its curvature results the same of that of half the complete beam for symmetry reasons. Due to this fact, we could limit the simulation to a cantilever bent by one wire at its free extreme (fig. 5.2a).
In the simulation we supposed, as it has been subsequently realized, to fix the wire at one extreme (point A in fig. 5.2b), then to make it pass over the glass and then stress it with a certain load. Afterwards, the other extreme of the wire has been fixed (point B in fig. 5.2b). The points at which the wire is fixed are also the points at which it is connected to the control circuit. Therefore, the part of the wire in which the current will flow and that will undergo a phase transition is only that comprehended between these two points.
Once the wire is stressed and fixed, we have to determine the length at zero stress of the portion of the wire in which the current will flow. If the wire is sufficiently stressed to induced a complete transformation to the martensitic phase, the initial strain is:

$$S_{in} = \frac{\sigma_{in}}{Y_m} + S_L \tag{5.10}$$

where σ_{in} is the stress of the wire. Considering eq. 5.9 and that $P = 2\sigma_{in}A$, the initial displacement of the glass at the distance l at which the wire hooks the glass results:

$$y_{in}(l) = \frac{2\sigma_{in}Al^3}{3EJ} = \frac{2\sigma_{in}A}{k} \tag{5.11}$$

where A is the SMA wire section and:

$$k = \frac{3EJ}{l^3} \tag{5.12}$$

the elastic constant that defines the relationship between the applied force to the glass and its displacement. We can calculate the initial length of the wire:

$$L_{in} = b + 2\big(a - y_{in}(l)\big) \tag{5.13}$$

and the length at zero stress as:

$$L_0 = \frac{L_{in}}{1 + S_{in}} \tag{5.14}$$

With this information it is possible to determine the evolution of the strain of the wire when a certain current is applied to it. The displacement y correspondent to a certain strain S is:

$$y(l) - y_{in}(l) = -\frac{L - L_{in}}{2} = -\frac{S - S_{in}}{2} L_0 \tag{5.15}$$

Therefore, considering eq. 5.9 at $x = l$, the relationship between the wire strain and stress determined by the glass response is:

$$S - S_{in} = \frac{4A(\sigma_{in} - \sigma)}{L_0 k} \tag{5.16}$$

Considering the constitutive law (eq. 3.25) and the previous result we obtain:

$$\Big(\sigma - \sigma_{in}\Big)\left(1 + \frac{4Y(\xi)A}{L_0 k}\right) = \Big[Y(\xi) - Y(\xi_0)\Big]S_0 - S_L\Big[Y(\xi)\xi_S - Y(\xi_0)\xi_{S,0}\Big] \tag{5.17}$$

Eq. 5.17 is similar to eq. 3.33 that concerns the system with a bias spring attached to a SMA wire. In this system the constant k has the dimension of a spring constant but depends on the dimensions and material properties of the glass. By resolving numerically eq. 5.17 and using the kinetic laws described in section 4.2 to describe the martensitic fraction behaviour, it is possible to determine the strain evolution of the wire when heated and then the glass displacement.
As for eq. 5.9, the glass curvature is represented by a cubic polynomials. Realizing a lens surface of this type will inevitably introduce some aberrations, but it is possible to reduce them using only the central part of the glass. In order to determine the lens focal power, we need to determine the glass radius of curvature that can be written as:

$$R = \frac{\left(1 + \left(\frac{dy}{dx}\right)^2\right)^{\frac{3}{2}}}{|\frac{d^2y}{dx^2}|} \tag{5.18}$$

which in our case results:

$$R = \frac{1 + \left(\frac{Pl}{EJ}\right)^2 x^2 - \left(\frac{P}{EJ}\right)^2 l x^3 + \left(\frac{P}{2EJ}\right)^2 x^4}{\frac{P}{EJ}\Big(l - x\Big)} \tag{5.19}$$

If x is sufficiently small, we can approximate the radius to a constant:

$$R \simeq \frac{EJ}{Pl} \tag{5.20}$$

Considering $x = l/4$ and the stress and dimensions of the order of the device we built, we are committing an error of about the 30% for the external rays.
Recalling that the focal length of a thin lens of a material with refraction index as n_L, curvature radii R_1 and R_2 and refraction index of the external medium n can be determined with the lensmaker equation:

$$\frac{1}{f} = \frac{n_L - n}{n}\left(\frac{1}{R_1} - \frac{1}{R_2}\right) \tag{5.21}$$

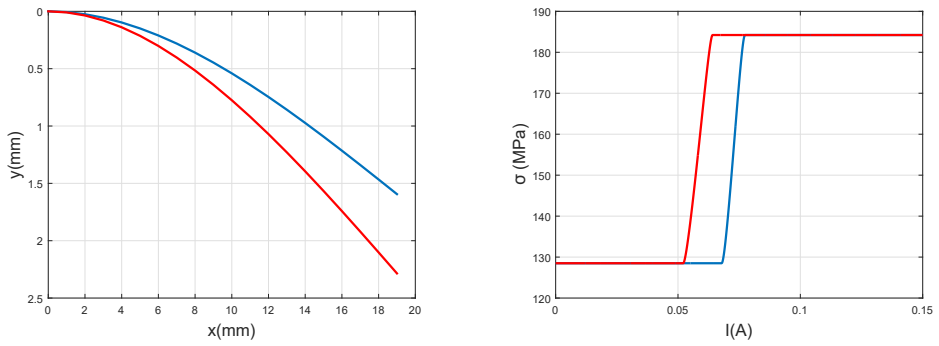

(a) (b)

Figure 5.3: (a) Simulated curvature of the glass at the initial position (blue) and when the SMA wire has completely recovered its strain (red line). (b) Simulated stress of the SMA wire that hook the glass when heating (blue) and cooling (red) as function of the applied current.

and considering the device as a lens with a flat surface on one side and one with curvature radius R on the other, the focal length results:

$$f = \frac{R}{n_L - 1} = \frac{EJ}{\Big(n_L - 1\Big)Pl} \tag{5.22}$$

In fig. 5.3 we report the simulated glass displacement and stress change for a cantilever with the dimensions of one which we then effectively realised (length $l = 19.7 \pm 0.5$ mm, width $w = 23.0 \pm 0.5$ mm, thickness $h = 0.17 \pm 0.005$ mm, wire prestress $\sigma_{in} \simeq 130$ MPa). The glass displacement is reported for the maximum current and when current is off. As previously said, the glass is bent also when the applied current to the wire is null because the wire is prestressed. It would not be possible to start from a flat glass because the wire stress is necessary to the repeatability of the strain recovering.
As expected, the wire stress increases with current similarly as in the case of a SMA wire bounded to a bias spring. Indeed the response of the glass to the wire stress is elastic. Moreover, the simulation does not consider any gel under the glass. The gel can be considered as solid, therefore, with a gel below the glass, the response of the device will still be elastic but with a higher elastic constant and the final stress of the wire will be higher too. The gel, as well as being necessary to create a device with a refractive index higher than that of the air, also allows to reach higher wire stresses. This could be useful to reach the condition of linear relationship between resistivity and strain.

5.2 The cantilever

In particular, we realized two cantilevers with different height and similar width and length in order to verify the simulation results. The cantilevers have been built by using 0.17 mm thick microscope slides glass sheets. Since we did not have thicker glasses we built them by gluing together two thinner glasses using an optical UV adhesive. The result was a glass with an effective thickness of 0.5 mm because the thickness of the glue layer is not negligible. The response of a cantilever constituted by a unique glass would have been certainly different but similar.
A cantilever was built by gluing together some thick rectangular glasses into a column and then on one extreme of a thick glass. Then a thin glass has been glued on the column in order to fix one of its extremities and create a cantilever. The object built in such a way is shown in fig. 5.4a. Some adhesive tape has been attached to the superior glass in order to minimize the wire

Dimensions and initial conditions					
Cantilever	l(mm)	b(mm)	h(mm)	a(mm)	σ_{in}(MPa)
1	19.7 ± 0.5	23.0 ± 0.5	0.17 ± 0.005	8.1 ± 0.5	128 ± 4
2	24.0 ± 0.5	23.0 ± 0.5	0.05 ± 0.5	8.3 ± 0.5	220 ± 8

Table 5.1: Dimensions and initial conditions of the realized cantilevers.

Simulation results				
Cantilever	k_{th}(N/m)	k_{exp}(N/m)	k_{comsol}(N/m)	k^{gel}_{comsol}(N/m)
1	302 ± 27	376 ± 6	311	641
2	4263 ± 158	4143 ± 237	4367	4831

Table 5.2: Theoretical and experimental results about the glass cantilevers.

Simulation results				
Cantilever	$\Delta y(l)_{th}(mm)$	$\Delta y(l)_{exp}(mm)$	$\Delta D_{th}(m^{-1})$	$\Delta D^{gel}_{th}(m^{-1})$
1	0.74 ± 0.07	0.75 ± 0.03	1.3262 ± 0.5187	0.6 ± 0.2
2	0.48 ± 0.02	0.5 ± 0.02	0.5844 ± 0.0439	$0.58 + -0.04$

Table 5.3: Theoretical and experimental results about the glass cantilevers.

friction on the glass and to prevent the glass cutting the wire.
The cantilevers were fixed on a previously prepared stripboard in such a way that the SMA wires could hook the glass and be fixed by screws. Electric contacts have been previously prepared on the stripboard to connect the SMA wire to the same control circuit used for the characterization (see fig. 5.4b). After having prepared the cantilevers, we followed the procedure described in the previous paragraph: we fixed one extreme of the SMA wire to the stripboard, make it hooking the cantilever glass and then stressed it by hanging a load to the other extremity. Then, also this extremity has been fixed to the stripboard. The result of this procedure is shown in fig. 5.4c. The dimensions and initial prestress of the cantilever that we have realised are reported in tab. 5.1.
We measured the glass displacement by image analysis, similarly to what has been done to measure the SMA wire strain in the characterization. We calibrated a camera and found the correspondence between pixel and space differences exploiting a millimeter sheet placed on the side of the glass (see 5.5a), as similarly done for the characterization measurements (see paragraph 4.3.2). The profile of the cantilever glass was highlighted with white and black color in correspondence of the point in which it was hooked by the wire (see fig. 5.5b) in order to better distinguish the glass border. The position of the glass was identified by fitting the intensity profile of a column of pixel as shown in fig. 5.5c.
Once the cantilever was fixed and stressed, the current was varied step by step from zero to a sufficient value to induce a complete transformation. Since the SMA wire was in contact with the glass, the heat flow coefficient was higher than in the characterization measurements. Therefore, we expected the transition currents to be higher than in the characterization measurements. An other factor that contributed to the increase of the transition currents was the the higher stress that was reached when the heated SMA wire contracted. After each acquisition the wire was relaxed and the pixel correspondent to the horizontal position of the glass was determined. In such a way it was possible to calculate the glass displacement.
By the measurement of the initial stress and the initial glass displacement, we have been able to determine the experimental value of the constant k and to compare it with the theoretical

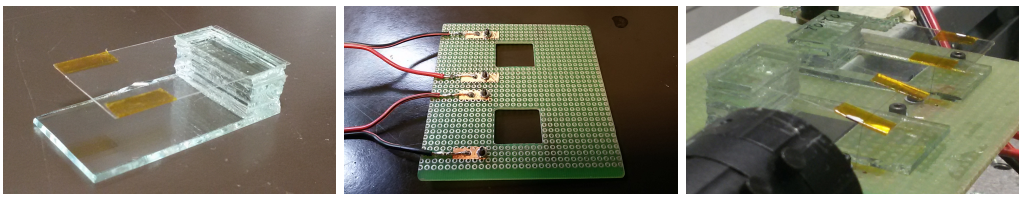

(a) (b) (c)

Figure 5.4: (a) Image of one of the realized glass cantilevers. The cantilever has been made by gluing together in a column some little rectangular glasses, then the column has been glued between the extremities of a thick and a thin glass. The latter is the glass that has been bent by exploiting a SMA wire. (b) Back of the stripboard on which the cantilevers as that in fig. 5.4a has been attached. The SMA wire were made to pass through the holes of the stripboard in correspondence of the contacts on the back and fixed by a washer. The washer secured the contact between the wire and some copper scotch that was connected to a cable. (c) Cantilevers stressed with SMA wires and fixed on the stripboard. the black object in the image is the objective of the camera used to determine the position of the cantilever.

values. The theoretical values are calculated as:

$$k_{th} = \frac{3EJ}{2l^3} \tag{5.23}$$

While the experimental values are:

$$k_{exp} = \frac{2F_{in}}{y_{in}} \tag{5.24}$$

where F_{in} is the initial force with which the SMA wire is stressed and y_{in} the initial glass displacement. The factor 2 is present because the force on the glass is double with respect to that of the wire.
The values of the constant k were also determined by exploiting the "COMSOL-Multiphysics®" software (see fig. 5.7a). Since the relationship between the displacement of the glass at the point of the load application $\delta y(l)$ and the load P is $P = k\delta y(l)$, the cantilevers were simulated under a unitary load and the elastic constant has been calculated as:

$$k_{comsol} = \frac{1}{\delta y} \tag{5.25}$$

The values of the elastic constants determined for each simulation are reported in tab. 5.2. The values are slightly different, but considering that the geometry of the devices is subject to errors and that also the materials properties (such as the glass elastic modulus) are subject to variations due to different materials processing, we can consider the result as good.
A further comparison between theory and the experimental results, which does not depend on the initial position of the glass as the esteem of k, can be done considering the difference form the initial and final displacement of the glass (which obviously depends on the wire prestress). The comparison between the theoretical and experimental results is good as demonstrated by the values in tab. 5.3.
In tab. 5.3 there are also reported the correspondent focal power variation for the two simulated devices expressed in diopters and calculated as:

$$D = \frac{1}{f_{fin}} - \frac{1}{f_{in}} \tag{5.26}$$

where f_{in} and f_{fin} are calculated by using eq. 5.22.

During the tests of the cantilevers, we also measured the voltage drop at the wire extremes

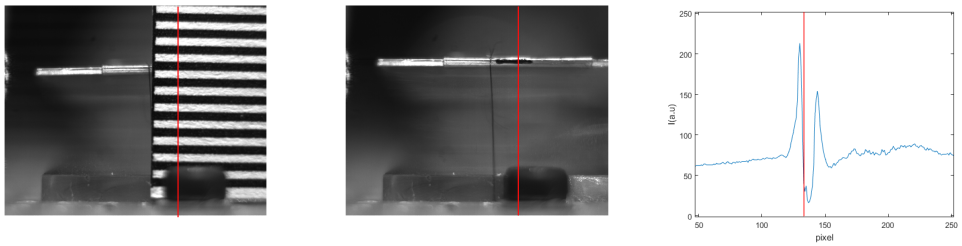

(a) (b) (c)

Figure 5.5: (a) Side view of the cantilever with the calibration target. The white and black stripes are 1 mm large and the intensity variation between them along the pixel column highlighted in red has been exploited to obtain the calibration data. (b) Side view of the cantilever. The glass profile was highlighted with white and black color in order to better determine its position by image analysis. (c) Intensity profile the column of pixel in correspondence of the red line in (b). The intensity variation between the black and white zones in correspondence of the glass border has been fitted in order to determine the glass position. The correspondent pixel position is highlighted with a red line.

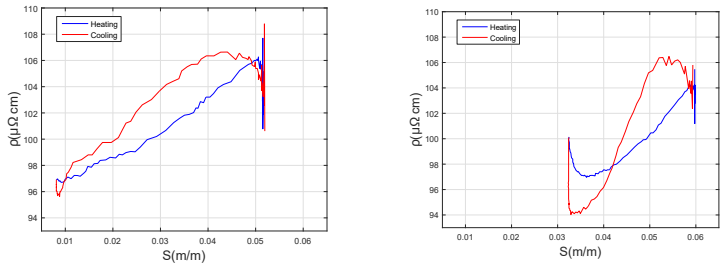

(a) (b)

Figure 5.6: (a) Resistivity of the wire stressing a glass cantilever (cantilever 1 in tab 5.1) when heating (blue) and cooling (red). (b) Resistivity of the wire stressing a glass cantilever (cantilever 2 in tab 5.1) when heating (blue) and cooling (red).

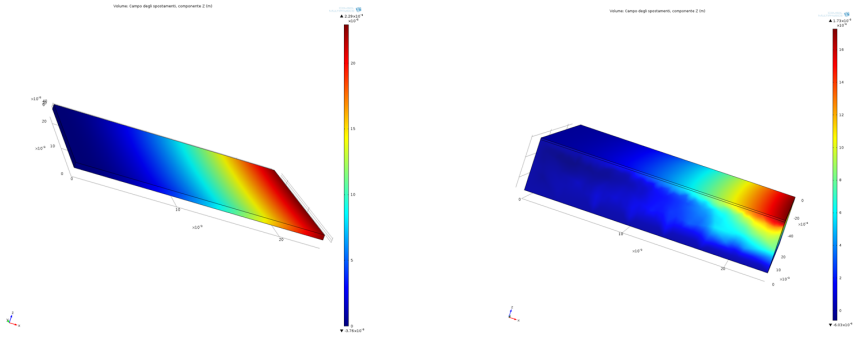

(a) (b)

Figure 5.7: Images from the "COMSOL-Multiphysics®" simulation of the glass cantilevers without (a) and with the gel below. The color scale indicates the displacement from the position before the application of the stress.

and, by knowing the input current, we calculated the resistivity of the wire. Two examples of the resistivity behaviour are reported in fig. 5.6. In such cases there is no linear relationship between the wire strain and the resistivity. This fact could be due to the variation of the stress during the strain recovery of the wire.
A material with a refractive index higher than that of air will be inserted between the glasses of the final device. For this purpose we have chosen a gel [82] obtained by mixing two liquid components: easy to be poured between the glasses as liquid and to make it solidify.
Moreover, the gel can be considered a solid and therefore the response of the glass to the SMA wire will continue to be elastic but with a higher elastic constant k. With the presence of the gel will be possible to increase the initial prestress of the wire reaching the same glass displacement that we had without. The simulation with the "COMSOL-Multiphysics®" software has been carried out considering the presence of the elastomeric material under the cantilever (see fig. 5.7b). As it can be deduced from the values in tab. 5.2, the presence of the gel is not relevant in the case of the thick glass while it is in the case of the thin one.
We can make a simple calculation to determine the variation of the focal lengths with the presence of the gel using the elastic constant values k^{gel}_{comsol}. Since k can be calculated as:

$$k = \frac{3EJ}{l^3} \tag{5.27}$$

we can define an equivalent value of the flexural modulus EJ as:

$$\Big(EJ\Big)_{eq} = \frac{k^{gel}_{comsol} l^3}{3} \tag{5.28}$$

and calculate the correspondent focal lengths with eq. 5.22:

$$f = \frac{\Big(EJ\Big)_{eq}}{\big(n_L - 1\big)Pl} \tag{5.29}$$

The variation of diopters obtained for the realized cantilevers are reported in tab. 5.3 and, as expected, are lower than the variations calculated without considering the presence of the gel.

5.3 The final prototype

We finally implemented two devices to prove the possibility to create a lens with variable focal length by exploiting SMA wires. This two devices consist in a thin rectangular glass (0.17 mm thick) leaning on two pins placed along the long sides of the glass. A thick rectangular glass of the same dimensions act as base. A gel ("Dow corning 3-6575" [82]), obtained by mixing two liquid components, has been poured and made to solidify between the glasses in order to fill the gap between the two. The superior glass (the thinner one) is meant to be bent by two SMA wires that hook it at its extremities while the thick one to act as base. Two smaller rectangular glasses have been glued on the extremities of the superior glass provide a symmetrical bending, while maintaining the glass surface flat.
A special support has been designed and built by exploiting a 3D laser printer.The glasses with the gel inside have been placed in the centre of the support over a circular hole. The SMA wires pass through four 0.5 mm diameter holes, placed in such a way that the wire hooks the glass at a defined position. The wires have been stressed according to the following procedure. They have been initially fixed at one extremity by a screw. Then they have been contemporary stressed by hanging a load to the other extremity in order to bend the glass symmetrically. Finally also the second extremity has been fixed by a screw maintaining the glass in the position reached after the wire loading.
The wires have been fixed by using screws on the sides of the support that also acted as contact

Dimensions and initial conditions					
Device	l(mm)	b(mm)	h(mm)	a(mm)	σ_{in}(MPa)
1	15.0 ± 0.5	25.0 ± 0.5	0.17 ± 0.005	8.7 ± 0.5	165 ± 6
2	15.0 ± 0.5	25.0 ± 0.5	0.17 ± 0.005	8.7 ± 0.5	165 ± 6

Table 5.4: Dimensions and initial conditions of the realized devices.

Simulation results							
Device	f_{in}^{th}(cm)	f_{fin}^{th}(cm)	f_{in}^{exp}(cm)	f_{fin}^{exp}(cm)	$\Delta D^{th}(m^{-}1)$	$\Delta D^{exp}(m^{-}1)$	$\Delta D_{gel}^{th}(m^{-}1)$
1	36 ± 4	19 ± 2	42.0 ± 0.5	22.0 ± 0.5	2.4 ± 0.6	2.2 ± 0.1	1.8 ± 0.4
2	36 ± 4	19 ± 2	37.5 ± 0.5	20.0 ± 0.5	2.4 ± 0.6	2.3 ± 0.1	1.8 ± 0.4

Table 5.5: Theoretical and experimental results about the devices that have been realized.

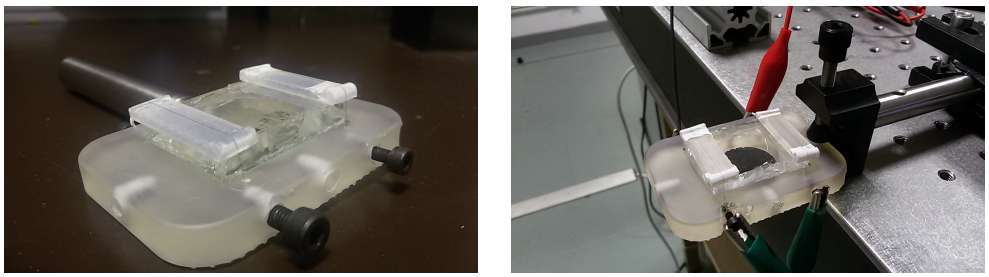

(a) (b)

Figure 5.8: Glass bent by SMA wire and support system. In fig. (b) the support is fixed by a clamp an protruding out in order to be able to stress the wires by hanging a certain load to them.

for the heating of the SMA wires with current. Some steel spheres have been inserted between the screws and the wires to avoid the damage of the wires.
Actually, since the device and the procedure have been made manually, it has been impossible to bend the glass in an exact symmetrical fashion.

Two plastic caps created with the 3D laser printer have been inserted between the wires and the thin glass in order to avoid the glass cutting the wires. Furthermore, some teflon tape has been applied under the contact points with the wire to reduce friction. The SMA wires have been connected in series, by exploiting the screws as contacts, to the same control circuit used for the characterization and the control of the previously realized cantilevers.
The plastic support has been fixed to a post by a screw and set in vertical position such that the glass is bent along the horizontal axis. A collimated laser beam has been made to pass through the circular hole as schematised in fig. 5.9a. The device acts as a lens: the first surface in fact is plane and lets the beam undisturbed while the second surface focuses the beam. Since the glass is bent only along one axis, this lens has two different curvature radii and focuses the light in just one direction. Therefore, the beam is focused on a line.
The glass curvature can be increased by applying the same current to the two SMA wires. In this case, the focal length is reduced. By placing a target at a distance from the device equal to the focal length when the current is off, it is possible to show the focused and unfocused laser beam when the current is respectively off and on as in fig 5.9b.
Furthermore, we placed a camera besides the device and two similar striped targets at the initial (when non current is applied to the SMA wire) and final (when the curvature has changed the most) focal lengths as showed in fig. 5.12a. In this case the total focal length of the system is

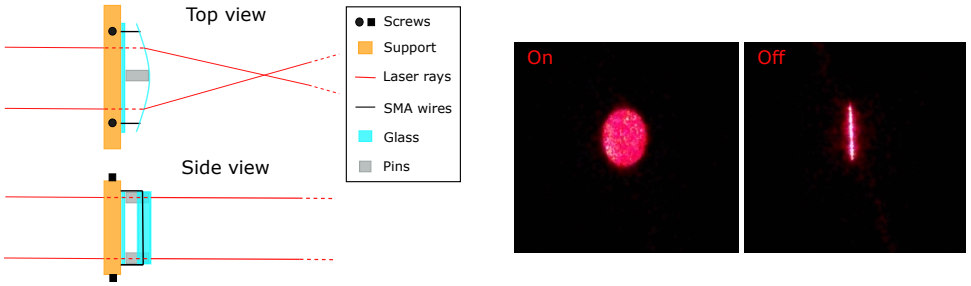

(a) (b)

Figure 5.9: (a) Scheme of the focusing of a collimated laser beam by one glass bent with SMA wires. (b) Laser beam section when the current which heat the SMA wire is off and on.

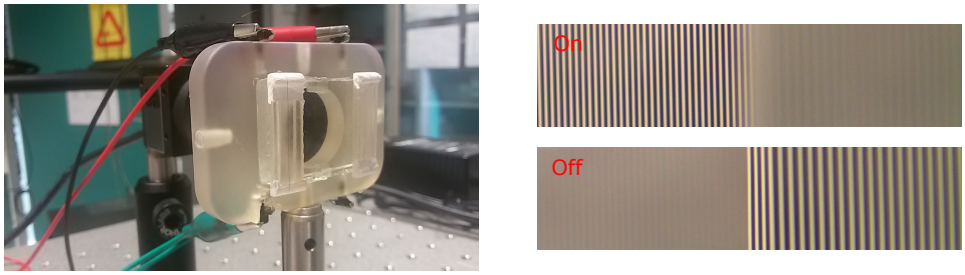

(a) (b)

Figure 5.10: (a) Image of the camera and the device used to capture the images of two striped targets in (b) placed at the maximum and minimum focal lengths of the system. (b) Striped targets alternatively at focus when current is switched on and off.

determined by the composition of the device and the camera objective. In fig. 5.10b we reported two images of the two targets acquired with the current on and off respectively. As expected the targets are alternatively on focus when the focal point of the system corresponds to the point in which they are placed. From fig. 5.10b it is clear that such a system has some aberrations. First of all, we have to consider that the system is focusing only along one axis. Therefore, the rays which are not on planes in parallel to the bending axis are not focused on the camera. This effect is minimized by the fact that we are observing a target represented by stripes perpendicular to these planes. Other aberrations are due to the unavoidable asymmetrical bending of the glass and possible inhomogeneities of the gel.

As mentioned before we built two of these devices. In tab. 5.4 the dimensions of the superior glass with which we have built the devices are reported. The measured focal length and the correspondent variation of diopters are reported in tab. 5.5 and compared with the esteemed values calculated with the simulation. The two devices have different focal lengths because the building procedure was hand made and slight differences in the wire stress imply a slightly different curvature and, therefore, a different focal length.

However, the focal lengths are both superior to the values esteemed by the simulation. This fact is due to the presence of the gel under the glass that is not taken into account in the Matlab simulation. With the gel, the glass curvature is lower and, therefore, the focal length is higher. The variation of diopters with the presence of the gel can be calculated exploiting the k^{gel}_{comsol} estimated from the "COMSOL-Multiphysics®" simulation as made in the previous section. The obtained values are reported in tab. 5.5.

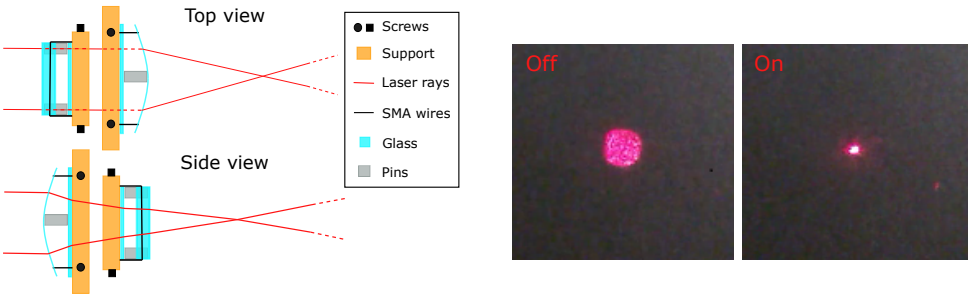

(a) (b)

Figure 5.11: (a) Scheme of the focusing of a collimated laser beam by two glass bent with SMA wires along perpendicular directions. (b) Laser beam section when the current which heat the SMA wire is off and on.

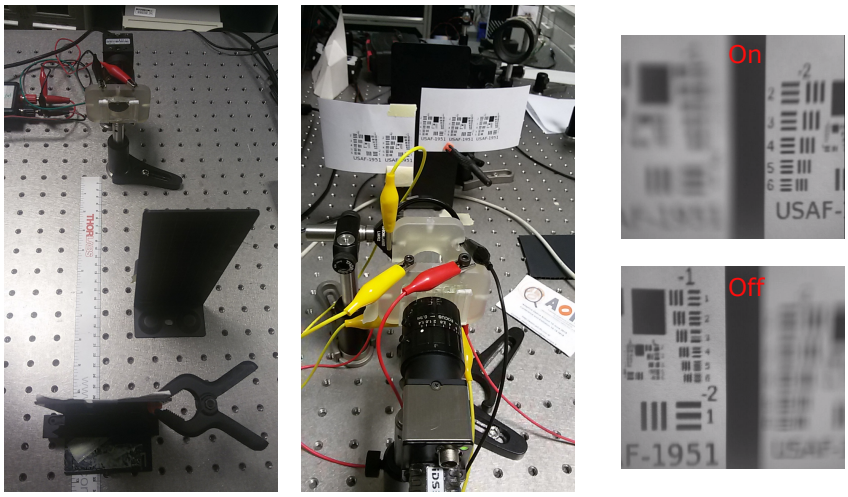

(a) (b) (c)

Figure 5.12: (a) Image of the system composed by a camera besides one of the built devices and the back of the supports of the striped targets reported in fig 5.10b. (b) Image of the system composed by a camera besides the two built devices and USAF targets placed at the maximum and minimum focal length of the system. (c) USAF targets alternatively at focus when current is switched on and off.

By placing the second device behind the first one such that the glass is bent along the vertical axis as schematised in fig. 5.11a, it is possible to focus a laser beam on a point rather than on a line as shown in fig. 5.9b. In such way we obtained a sort of lens with a variable focal length. The two devices do not have exactly the same focal lengths because of the unavoidably dimension and initial stress differences. Furthermore, they are not in the same position since they are placed side by side, and therefore they focus at different distances. In a lens composed only by two bent glasses with gel inside this effect would be much lower. Since the focal length along the horizontal and vertical axis are not exactly the same, the devices can be assumed to act like an astigmatic lens. We did not have the possibility to separately control the two devices, but we temporarily overcame the problem of the astigmatism by inserting a lens in an oblique position after the device as shown in fig. 5.12b. With this correction the performance of the device seems good from fig. 5.11b.

As made with the single device, we used a camera to focus two target placed at the maximum and minimum focal lengths. In this conditions the total focal length of the system is determined by the composition of the built devices, the objective of the camera and the lens we have used to "correct" the astigmatism. The pictures of the targets are reported in fig. 5.12c and show good result considering the strong unideal procedure with which we have built the devices.

5.4 Comments on the results

Some prototypes of SMA wire-based adaptive lens have been realized to prove the feasibility of the studied approach and provide an experimental confirmation of the theoretical simulations.
Firstly, we built glass cantilevers and bent them by means of SMA wires. By measuring the glass displacement under the stress of SMA wires heated with current, we determined the elastic constant of the cantilevers. The comparison between these measurements and the theoretical results is good, considering that the cantilevers were strongly idealized in the simulation with respect to those practically realized. Subsequently, we built two devices constituted by a glass that is symmetrically bent with respect to its center and leaning on a transparent gel substrate. Such devices have been exploited to reproduce the action of the designed deformable lens and allowed a first practical demonstration of the feasibility of devices based on this principle. We verified the ability of the device to focus a laser beam and compared the experimental focal lengths with those determined from the simulation results. The experimental values were slightly higher than those expected from the simulation. This means that the glass curvature was overestimated by the simulation. Such a result was expected because we neglected the presence of the gel under the glass. The focal lengths of the two devices are slightly different because of the unavoidable imprecisions in the stressing procedure of the SMA wires. Also the pouring of the gel under the glass has certainly lead to some differences between the two devices.
The simulation could be implemented in such a way to determine the relation between the dimensions and the wire pre-stress for the better performance of the device, i.e. the higher diopters variation. A new prototype could be designed and built considering the results of a simulation that consider the presence of the gel under the glass and using a more precise method to reduce the fabrication errors, in particular the stressing procedure could be monitored exploiting a load cell.

Conclusions and future perspectives

This thesis aimed at developing a deformable lens with variable focal length by exploiting SMA wires.
Firstly, we described the particular behaviour of the SMAs and why they can be used as actuation material in optics. We introduced a theoretical model of the behaviour of the SMA wires under different conditions (constant load or bound to a bias spring) and studied the case of a SMA wire heated by electrical current. The model presents several parameters which needed to be determined experimentally in order to carry out a simulation of the designed devices. With this aim we designed and build a setup for the characterization of SMA wires with 50 μm diameter. The SMA wires have been subjected to current cycles under constant load and their strain has been monitored through image analysis. In such a way, it has been possible to determine a first esteem of the time response of the wires, the maximum strain variation and the other parameters needed for the simulation.
From the characterization it is clear that higher stress of the wire leads to higher strain variation ΔS from the complete martensitic to the austenitic phase. For the maximum stress applied in the characterization, 216 MPa, the strain variation results $\Delta S \simeq 4.5\%$ m/m. This value is much higher than the strain of other actuation materials. For example the piezoelectric materials, which are already exploited in adaptive optics, have a maximum strain of about 0.1%.
We studied the relationship between the strain and the resistivity of the wire, that results linear and univocal only when a sufficient stress is applied.
After the characterization, we built some glass cantilevers with different thickness and bent them using a SMA wire in order to compare the simulations results carried out with the parameters determined by the characterization measurements with experimental data.The results showed a good agreement, confirming the characterization success.
Finally, we built a prototype of the deformable lens in order to verify the feasibility of the project. The glass sheets that compose the two refractive surfaces of the prototype are bent by two SMA wire placed on each one.With this prototype, we managed to build a device able to focus a laser beam and also objects at different distances on a camera sensor in an imaging setup.
At the light of the considerations made so far, we can consider the objective of this thesis to be achieved. We verified the large strain capabilities of SMAs and applied them in an adaptive optics application. These results clearly show the great potential of SMAs in the field of optics and opens up the route towards the development of small size adaptive lenses that can be easily integrated in several types of optical systems such as wearable optics.

Bibliography

[1] P. Kumar and D. Lagoudas, *Shape Memory Alloys, Modeling and Engineering Applications*. Springer, 2008.

[2] D. J. Leo, *Engineering Analysis of Smart Materials Systems,*. John Wiley and Sons, 2007.

[3] W. J. Buehler, J. V. Gilfrich, and R. C. Wiley, "Effects of low-temperature phase changes on the mechanical properties of alloys near composition tini," *Journal of Applied Physics*, vol. 34, 1963.

[4] C. M. Jackson, H. J. Wagner, and R. J. Wasilewski, "Nitinol - the alloy with a memory: Its physical metallurgy, properties and applications," tech. rep., Tech. Rep. NASA SP-5110 NASA Technology Utilization Office, Washington, D.C., 1963.

[5] F. E. Wang, W. J. Buehler, and S. J. Pickart, "Crystal structure and a unique 'martensitic' transition of tini," *Journal of Applied Physics*, vol. 36, pp. 3232–3239.

[6] L. Schetky, "Shape-memory alloys," *Scientific American*, no. 241, pp. 74–82.

[7] D. A. Miller and D. C. Lagoudas, "Thermo-mechanical characterization of niticu and niti sma actuators: Influence of plastic strains," *Smart Materials and Structures*, vol. 9, no. 5, pp. 640–652, 2000.

[8] "Smartflex® wire, 100% quality controlled shape memory wire for microactuators." https://www.saesgetters.com/sites/default/files/SMARTFLEX Accessed: 2016-12-20.

[9] J. M. Jani, M. Leary, A. Subic, and M. A. Gibson, "A review of shape memory alloy research, applications and opportunities," *Materials and Design*, vol. 56, pp. 1078–1113, 2014.

[10] G. Song, D. Patil, C. Kocurek, , and J. Bartos, "Applications of shape memory alloys in offshore oil and gas industry: A review," *Proceedings of earth and space 2010: engineering, science, construction, and operations in challenging environments*, vol. 366, pp. 14–17, 2010.

[11] A. LLC, "Sma fitting system benefits," 2017.

[12] A. Rao, A. Srinivasa, and J. Reddy, *Design of Shape Memory Alloy (SMA) Actuators*. Springer, 2015.

[13] J. H. Mabe, F. T. Calkins, , and G. W. Butler, "Boeing's variable geometry chevron, morphing aerostructure for jet noise reduction," *47th AIAA/ ASME/ ASCE / AHS / ASC Structures, Structural Dynamics and Materials Conference*, pp. 1–19, 2006.

[14] A. D. Johnson, "Non-explosive separation device," 1992. US Patent 5,119,555.

[15] B. Carpenter and J. Lyons, "Eo-1 technology validation report: Lightweight flexible solar array validation report," *Tech. rep., NASA Godard Space Flight Center*, 2002.

[16] C. I., "Status of application of smart structures technology to rotorcraft systems," *J Am Helicopter Society*, vol. 45, no. 4, pp. 228–252, 2010.

[17] Associated, Complexes, Adverse, and With, "(12) United States Patent (10) Patent No .: (45) Date of Patent :," 2015.

[18] D. C. Lagoudas, T. Kalmár-Nagy, and M. Z. Lagoudas, "Shape memory alloys for vibration isolation and damping of large-scale space structures," tech. rep., Texas A&M University, College Station, TX 77843-3409, USA, 2010.

[19] J. Paine and C. Rogers, "High velocity impact response of composites with surface bonded nitinol-sma hybrid layers," *Journal of Intelligent Material Systems and Structures*, vol. 5, no. 4, pp. 530–535, 1994.

[20] J. Painet, , and C. Rogers, "High velocity impact response of composite with surface bonded nitinol-sma hybrid layers," *ASME International Mechanical Engineering Congress and Exposition*, 2006.

[21] K. Otsuka and T. Kakeshita, "Science and technology of shape-memory alloys: New developments," *Material Reasearch Society Bulletin*, 2002.

[22] E. A. Williams, Shaw, Gordon, Elahinia, and Mohammad, "Control of an automotive shape memory alloy mirror actuator," *Mechatronics*, vol. 20, no. 5, pp. 527–534, 2010.

[23] K. Andrianesis and Y. Koveos, "Experimental study of a shape memory alloy actuation system for a novel prosthetic hand," *Shape Memory Alloys*, pp. 81–105.

[24] Maeno, Takashi, Hino, and Toshiyuki, "Miniature five-fingered robot hand driven by shape memory alloy actuators," *Proceedings of the 12th IASTEDInternational Conference, Robotics and Applications*, pp. 174–179, 2006.

[25] F. Solc and M. Vasina, "Modeling and control of sma actuator," *WSEAS, Transactions on Circuits and Systems*, vol. 3, pp. 1109–2734, 2004.

[26] J. Colorado, A. Barrientos, , and C. Rossi, "Biomechanics of morphing wings in a bat-robot actuated by sma muscles," *International Workshop on Bio-Inspired Robots*, 2011.

[27] S. J. Furst, G. Bunget, and S. Seelecke, "Design and fabrication of a bat-inspired flapping-flight platform using shape memory alloy muscles and joints," *Smart Matererial Structures*, vol. 22, p. 12pp, 2013.

[28] Festo, "Bionicopter." Brochure, 2017.

[29] J. Ryhanen, *Biocompatibility evolution of nickel-titanium shape memory alloy*. PhD thesis, Univeristy of Oulu, Finland, 1999.

[30] G. Andreasen and T. Hilleman, "An evaluation of 55 cobalt subsituted nitinol wire for use in orthodontics," *Journal of the American Dental Association*, vol. 82, pp. 1373–1375, 1971.

[31] Y. Haga, T. Mineta, W. Makishi, T. Matsunaga, and M. Esashi, "Active bending catheter and endoscope using shape memory alloy actuators," *Shape Memory Alloys*, pp. 107–126, 2010.

[32] M. Sasaki, Y. Arai, and K. Hane, "Automatic alignment of optical system using shape memory alloys," *Optical Review*, vol. 4, no. 5, pp. 584–587, 1997.

[33] B. Sutapun, M. Tabib-Azar, , and M. A. Huff, "Applications of shape memory alloys in optics," *Applied Optics*, vol. 37, no. 28, pp. 6811–6815, 1998.

[34] A. K. Maji, P. Wegner, and R. Rochin, "Surface actuation of lightweight mirrors with shape memory alloy," *Journal of Aerospace Enginieering*, vol. 17, no. 2, pp. 83–89, 2004.

[35] H. T. Inc., "Gemini sma ois," 2011.

[36] F. Butera and R. P. Chi-Wei Chiu, "Auto-focus device with shape memory actuator," June 19 2014. WO Patent.

[37] R. Topliss and A. B. D. Brown, "Sma actuation apparatus," Jan. 3 2013. US Patent.

[38] H. Ren and S.-T. Wu, *Introduction to adaptive lenses.* Jhon Wiley and Sons, 2012.

[39] D.-Y. Zhang, Y. B. V. Lien, J. Choi, , and Y.-H. Lo, "Fluidic adaptive lens with high focal length tenability," *Appl. Phys. Lett.*, vol. 82, pp. 3171–3172, 2003.

[40] J. Floyd, "Fluid filled and pressurized lens with flexible optical boundary having variable focal length," July 19 1995. US Patent.

[41] H. Ren and S.-T. Wu, "Variable-focus liquid lens by changing aperture," *Applied Physical Letters*, vol. 86, no. 21, 2005.

[42] S. Xu, Y. Liu, H. Ren, and S. T. Wu, "A novel adaptive mechanical-wetting lens for visible and near infrared imaging," *Opt. Express*, vol. 18, pp. 12430–12435, 2010.

[43] F. Schneidera, J. Draheima, C. Mullerb, and U. Wallrabea, "Optimization of an adaptive pdms-membrane lens with an integrated actuator," *Sensors Actuators*, vol. 154, pp. 316–321, 2009.

[44] H. Ren and S. T. Wu, "Variable-focus liquid lens," *Opt. Express*, vol. 15, no. 10, pp. 5931–5936, 2007.

[45] L. Dong, A. K. Agarwal, D. J. Beebe, , and H. Jiang, "Adaptive liquid microlenses activated by stimuli-responsive hydrogels," *Nature*, vol. 442, no. 7102, pp. 551–554, 2006.

[46] F. Carpi, G. Frediani, S. Turco, and D. D. Rossi, "Bioinspired tunable lens with muscle-like electroactive elastomers," *Advanced Functional Materials*, vol. 21, no. 21, pp. 4152–4158, 2011.

[47] N. Chronis, G. L. Liu, K. H. Jeong, and L. P. Lee, "Tunable liquid-filled microlens array integrated with microfluidic network," *Opt. Express*, vol. 11, pp. 2370–2378, 2003.

[48] B. Berge, "ElectrocapillaritÂ´e et mouillage de films isolants par leau," *C. R. Acad. Sci.*, vol. 317, pp. 157–163, 1993.

[49] T. Krupenkin, S. Yang, , and P. Mach, "Tunable liquid microlens," *Appl. Phys. Lett.*, vol. 82, no. 3, pp. 316–318, 2003.

[50] S. Kuiper and B. H. W. Hendriks, "Variable-focus liquid lens for miniature cameras," *Appl. Phys. Lett.*, vol. 85, pp. 1128–1130, 2004.

[51] E. Simon, B. Berge, F. Fillit, H. Gaton, O. Jacques-Sermet, M. Guillet, F. Laune, J. Legrand, M. Maillard, and N. Tallaron, "Optical design rules of a camera module with a liquid lens and principle of command for af and ois functions," *Proc. SPIE*, vol. 7849, no. 784903, 2010.

[52] H. Ren, S. H. Lee, , and S. T. Wu, "Reconfigurable liquid crystal droplets using a dielectric force," *Appl. Phys. Lett.*, vol. 95, p. 241108, 2009.

[53] S. Xu, H. Ren, Y. Liu, , and S. T. Wu, "Dielectric liquid microlens with switchable negative and positive optical power," *IEEE J. MEMS*, vol. 20, pp. 297–301, 2011.

[54] C. C. Yang, C. G. Tsai, , and J. A. Yeh, "Miniaturization of dielectric liquid microlens in package," *Biomicrofluidics*, vol. 4, p. 43006, 2010.

[55] A. Mermillod-Blondin, E. McLeod, , and C. B. Arnold, "High-speed varifocal imaging with a tunable acoustic gradient index of refraction lens," *Optics Letters*, vol. 33, no. 18, 2008.

[56] D. Koyama, R. Isago, , and K. Nakamura, "Compact, high-speed variable-focus liquid lens using acoustic radiation force," *Opt. Express*, vol. 18, p. 25158, 2010.

[57] P. Liebetraut, S. Petsch, J. Liebeskind, and H. Zappe, "Elastomeric lenses with tunable astigmatism," *Light: Science & Applications*, vol. 2, no. 1, 2013.

[58] S. Bonora, Y. Jian, P. Zhang, A. Zam, E. N. Pugh, Jr., R. J. Zawadzki, and M. V. Sarunic, "Wavefront correction and high-resolution in vivo oct imaging with an objective integrated multiactuator adaptive lens," *Opt. Express*, vol. 23, no. 17, pp. 21931–21941, 2015.

[59] J.-M. Choi, H.-M. Son, , and Y.-J. Lee, "Biomimetic variable-focus lens system controlled by winding-type sma actuator," *Opt. Expr.*, vol. 17, no. 10, pp. 8152–8164, 2009.

[60] N. Hasan, H. Kim, , and C. H. Mastrangelo, "Large aperture tunable-focus liquid lens using shape memory alloy spring," *Opt. Expr.*, vol. 24, no. 12, pp. 13334–13342, 2016.

[61] S. Xu, H. Ren, Y. J. Lin, M. G. J. Moharam, S. T. Wu, and N. Tabiryan, "Adaptive liquid lens actuated by photo-polymer," *Opt. Express*, vol. 17, pp. 17590–17595, 2009.

[62] F. Falk, "Model free-energy, mechanics and thermodynamics of shape memory alloys," *ACTA Metallurgica*, vol. 28, no. 12, pp. 1773–1780, 1980.

[63] F. Falk and P. Konopka, "Three-dimensional landau theory describing the martensitic transformation of shape memory alloys," *Journal de Physique*, vol. 2, pp. 61–77, 1990.

[64] R. B. Gorbet, *Control of hysteretic systems with Preisach representation.* PhD thesis, University of Waterloo (Ontario, Canada), 1997.

[65] Y. H. Teh, *Fast, accurate force and position control of shape memory alloy actuators.* PhD thesis, The Australian National University, Department of Information Engineering, ANU College of Engineering and Computer Science, 2008.

[66] K. K. Ahn and N. B. Kha, "Modeling and control of shape memory alloy actuators using preisach model, genetic algorithm and fuzzy logic," *Mechatronics*, vol. 18, pp. 141–152, 2008.

[67] I. Y. and P. T.J., "A constitutive model for hysteretic phase transition behavior," *Int. J. Eng. Sci.*, vol. 32, pp. 681–704, 1994.

[68] K. Tanaka, "A thermomechanical sketch of shape memory effect: one-dimensional tensile behavior," *Materials Science Research International*, vol. 18, p. 251, 1985.

[69] C. Liang and C. Rogers, "One-dimensional thermomechanical constitutive relations for shape memory materials," *Journal of Intelligent Material Systems and Structures*, vol. 1, no. 2, pp. 207–234, 1990.

[70] L. Brinson, "One-dimensional constitutive behavior of shape memory alloys: thermomechanical derivation with non-constant material functions and redefined martensite internal variable," *Intelligent Material Systems and Structures*, vol. 4, no. 2, pp. 229–242, 1993.

[71] A. Bekker and L. Brinson, "Phase diagram based description of the hysteresis behavior of shape memory alloys," *Acta mater.*, vol. 46, no. 10, pp. 3649–3665, 1998.

[72] PhD thesis.

[73] J.-J. Zhang, Y.-H. Yin, and J.-Y. Zhu, "Electrical resistivity-based study of self-sensing properties for shape memory alloy-actuated artificial muscle," *Sensors*, vol. 13, pp. 12958–12974, 2013.

[74] M. Pozzi and G. Airoldi, "The electrical transport properties of shape memory alloys," *Materials Science and Engineering*, vol. A273-275, pp. 300–304, 1999.

[75] J.L.Pons, D.Reynaerts, J. Peirs, R. Ceres, and H. .VanBrusse, "Comparison of different control approaches to drive sma actuators," *Proceedings of 8th International Conference on Advanced Robotics; Monterey, CA, USA*, pp. 819–824, 1997.

[76] T.-M. Wang, Z.-Y. Shi, D. Li, C. Ma, and Z.-H. Zhang, "An accurately controlled antagonistic shape memory alloy actuator with self-sensing," *Sensors*, vol. 12, pp. 7682–7700, 2012.

[77] K. Ikuta, "Micro/miniature shape memory alloy actuator," *IEEE-ICRA*, 1990.

[78] K. Ikuta, M. Tsukamoto, and S. Hirose, "Shape memory alloy servo actuator system with electric resistance feedback and application for active endoscope," *Proceedings of IEEE International Conference on Robotics and Automation; Philadelphia, PA, USA.*, pp. 427–430, 1988.

[79] S. Zhenyun, W. Tianmiao, L. Da, M. Chen, and Y. Xiangnan, "A fuzzy pid-controlled sma actuator for a two-dof joint," *Chinese Journal of Aeronautics*, vol. 27, no. 2, pp. 453–460, 2014.

[80] N. Ma, G. Song, and H.-J. Lee, "Position control of shape memory alloy actuators with internal electrical resistance feedback using neural networks," *Smart Materials and Structures*, vol. 13, pp. 777–783, 2004.

[81] "NI USB-6008 device specifications." http://www.ni.com/pdf/manuals/375295a.pdf. Accessed: 2017-02-10.

[82] "Dow corning® q3-6575 dielectric gel." http://www.polymer-g.com/prdFiles/q3-6575.PDF. Acessed: 2017-08-20.